In this thesis, a homogenized constitutive contact model representing the thermomechanical contact interaction of a tire's tread rubber cap with the road surface has been developed with a focus on tire rolling resistance computations in frameworks using *Arbitrary Lagrangian Eulerian kinematics*. This constitutive model describes the statistically averaged thermo-viscoelastic response of a single tread block in unilateral frictionless contact with a rough road surface and the subsequent internal dissipation in an energy consistent way.

The homogenization of this contact interaction is based on the identification of an equivalent uniaxial compression test of the tread's bulk material, which allows for a one-dimensional representation of the constitutive material law. In the course of the thesis, the homogenization approach is applied to simple contact scenarios in order to investigate its accuracy. In a next step, the stochastic average thermo-viscoelastic contact behavior of tread blocks on measured smooth and rough asphalt surfaces are identified with *Monte Carlo simulations*.

Based on these results, the rolling resistance of simple rubber wheels and air inflated tires is computed in coupled thermo-viscoelastic, tractive rolling contact simulations, where the homogenized unilateral tread-road contact response is represented by the developed constitutive contact law. Herein, the temperature and frequency dependency of rubber friction is taken into account via a phenomenological friction model. With this framework the stationary thermomechanical response of novel tire designs can be calculated at a higher level of detail compared to previous approaches, which is a crucial aspect in the development process of low rolling resistance tires.

ISBN 978-3-935732-44-4

ibnm

A Constitutive Contact Model for Homogenized Tread-Road Interaction in Rolling Resistance Computations

R. Beyer

R. Beyer

A Constitutive Contact Model for Homogenized Tread-Road Interaction in Rolling Resistance Computations

F17/2 F17/2

Institut für Baumechanik und Numerische Mechanik
Gottfried Wilhelm Leibniz Universität Hannover

ibnm

Hauptreferent:
Prof. Dr.-Ing. Udo Nackenhorst

Korreferent:
Prof. Dr.-Ing. habil. Michael Kaliske

Doktorand:
Robert Beyer, M.Sc.

A Constitutive Contact Model for Homogenized Tread-Road Interaction in Rolling Resistance Computations

Von der Fakultät für
Bauingenieurwesen und Geodäsie der
Gottfried Willhelm Leibniz
Universität Hannover

zur Erlangung des Grades eines

Doktor-Ingenieurs

genehmigte Dissertation von

Robert Beyer, M.Sc.

Hannover 2016

Tag der Einreichung:
25.05.2016
Tag der mündl. Prüfung:
08.09.2016

**Institut für Baumechanik und
Numerische Mechanik**

Herausgeber:
Prof. Dr.-Ing. Udo Nackenhorst

Verwaltung:
Institut für Baumechanik
und Numerische Mechanik
Gottfried Willhelm Leibniz
Universität Hannover
Appelstr. 9A
30167 Hannover
Tel.: +49 (0)511 / 762-3219
Fax: +49 (0)511 / 762-19053

ISBN 978-3-935732-44-4

Abstract

In this thesis, a homogenized constitutive contact model representing the thermomechanical contact interaction of tire tread blocks with the road surface was developed with a focus on tire rolling resistance computations in frameworks using *Arbitrary Lagrangian Eulerian kinematics*. This one-dimensional constitutive contact model describes the statistically averaged thermo-viscoelastic response of a single three-dimensional tread block in unilateral frictionless contact with a rough road surface and the subsequent internal dissipation in an energy-consistent way.

The homogenization of this contact interaction is based on the identification of an equivalent uniaxial compression test, which allows for a one-dimensional representation of the constitutive material model that describes the tread rubber. In the course of the thesis, the accuracy of the homogenization approach is investigated for the contact interaction with a spherical asperity first. In a next step, the stochastic average thermo-viscoelastic contact behavior of tread blocks on measured smooth and rough asphalt surfaces are identified with *Monte Carlo simulations* and transferred into constitutive contact models.

Based on these results, the rolling resistance of solid rubber wheels and air-inflated radial tires is computed in coupled thermo-viscoelastic tractive rolling contact simulations, where the homogenized unilateral tread-road contact response is represented by the developed constitutive contact model. Herein, the temperature and frequency dependence of rubber friction is taken into account via a phenomenological friction model. With this framework the stationary thermomechanical response of novel tire designs can be calculated at a higher level of detail compared to previous approaches, which is a crucial aspect in the development process of low rolling resistance tires.

Keywords Rough surface contact; Contact homogenization; Thermomechanical coupling; Arbitrary Lagrangian Eulerian kinematics (ALE-kinematics); Rolling contact; Rolling resistance; Finite element method (FEM); Time discontinuous Galerkin method (TDG-method)

Zusammenfassung

In der vorliegenden Arbeit wurde ein homogenisiertes konstitutives Kontaktmodell zur Beschreibung der thermomechanischen Kontaktinteraktion von Reifenprofilblöcken mit der Fahrbahnoberfläche entwickelt, wobei der Fokus auf Rollwiderstandsberechnungen im Rahmen einer *gemischten Euler-Lagrange Kinematik* lag. Dieses eindimensionale konstitutive Kontaktmodell beschreibt das statistisch gemittelte, thermo-viskoelastische Verhalten eines einzelnen dreidimensionalen Profilblocks im unilateralen, reibungsfreien Kontakt mit einer rauhen Fahrbahnoberfläche, sowie die resultierende interne Dissipation in energiekonsistenter Form.

Die Homogenisierung der Kontaktinteraktion basiert auf der Identifizierung eines äquivalenten unilateralen Druckversuchs, was eine eindimensionale Darstellung des konstitutiven Materialmodells erlaubt welches das Profilgummi beschreibt. Die Genauigkeit des Homogenisierungsansatzes wird zunächst am Beispielt der Kontaktinteraktion mit einer Kugel untersucht. Im Anschluss daran wird unter Anwendung von *Monte Carlo Simulationen* das statistisch gemittelte thermo-viskoelastische Kontaktverhalten von Profilblöcken auf gemessenen glatten und rauen Fahrbahnoberflächen bestimmt und in konstitutive Kontaktmodelle überführt.

Aufbauend auf diesen Ergebnissen wird der Rollwiderstand von Vollgummirädern und luftgefüllten Reifen mit gekoppelten thermo-viskoelastischen traktiven Rollkontaktberechnungen ermittelt, wobei der homogenisierte unilaterale Profil-Fahrbahnkontakt mittels des entwickelten konstitutiven Kontaktgesetzes dargestellt wird. Hierbei wird die Temperatur- und Frequenzabhängigkeit der Gummi-Reibung durch ein phänomenologisches Reibgesetz berücksichtigt. Mit Hilfe dieser Modellierung kann das stationäre thermomechanische Verhalten neuer Reifendesigns mit einem größeren Detaillierungsgrad berechnet werden als dies bisher möglich war, was bei der Entwicklung von Reifen mit geringem Rollwiderstand eine wichtige Rolle spielt.

Stichworte Kontakt mit rauer Oberfläche; Kontakthomogenisierung; thermomechanische Kopplung, gemischte Euler-Lagrange Kinematik (ALE-Kinematik); Rollkontakt; Rollwiderstand; Finite Elemente Methode (FEM); Zeit-diskontinuierliche Galerkin Methode (TDG-Methode)

Contents

1 Introduction

Motivation

In modern economy an increasing percentage of the transport of goods relies on trucks. For this reason, it is of high economical relevance to maximize the energy efficiency of these means of transport and to minimize their consumption of resources. Recent studies of [Cullen et al., 2011; Holmberg et al., 2012] on the energy consumption of cars and trucks give an overview of the percentile energy loss for different truck parts and their energy saving potentials. Among other factors of influence, e.g. aerodynamics, weight reduction, and combustion efficiency, large energy saving potentials were found in the optimization of tires. For this reason, current research initiatives aim for the development of sustainable tire designs with improved energy efficiency, e.g. the *Lorry project* (www.lorryproject.eu; funded by the European Union from 2011 to 2016). The goal of this interdisciplinary project is a reduction of resource consumption by developing new tire rubber compounds and optimized tread patterns. These novel compounds shall contain a higher percentage of natural rubber and also possess increased durability. The expected gain of these improvements is a reduction of the tire's rolling resistance by at least 20%. According to the studies [Holmberg et al., 2012; van Haaster et al., 2015] a reduction of rolling resistance by 10% results in approximately $2 - 2.5\%$ less fuel consumption.

The achievement of these goals requires detailed knowledge of the processes causing rolling resistance and of the quantification of their contributions, see ISO 18164:2005 and ISO 28580:2009 for standard procedures of measurement. The main cause of rolling resistance is the viscoelastic material behavior of the different rubber compounds in the material layers that make up the tire carcass. In addition to a fibre-reinforcement for higher tensile strength of the rubber layers, a modern radial tire also possesses a steel belt, which increases the bending stiffness below the tread cap and gives the tire its characteristic flat shape. During rolling motion the tire is flexed by the contact with the road, which also bends the steel belt. Due to the large difference in stiffness between belt and rubber, the connected rubber layer is subjected to large strains at high shear rates, which result in a large amount of viscous dissipation. The dissipated mechanical energy is transferred into heat and thereby significantly increases the tire's temperature. This change of temperature severely affects the material properties of rubber compounds, especially damage and aging effects are more pronounced at high temperatures. For this

reason, detailed tire calculations require a thermomechanically coupled framework so that these material phenomena can be take into account.

A further important contribution to rolling resistance is the thermomechanical contact interaction of the tread cap with the road. Both the tread pattern and the road surface roughness significantly influence rolling resistance. [van Haaster et al., 2015] measured a difference of 8-10% in rolling resistance between coarse and smooth asphalt textures, which is in accordance with the extensive literature review recently presented in [Willis et al., 2014]. In the above context, the term 'coarse' refers to the optically visible mesoscale asperity size (mm) rather than to the macroscopic waviness of the road (cm; m) or to the microscopic surface topology of each asperity (μm). Consequently, potential starting points for the optimization of the tire-road interface towards reduced rolling resistance can be found in the tire (e.g. adaptations of the tread rubber compound and the tread pattern) as well as on the road surface (surface characteristics in road building projects). However, the potential reduction of rolling resistance by smoothing the road surface is obviously limited by the necessity to ensure the transmission of traction and braking in the tread-road interface, as particularly a good wet grip behavior is a crucial safety factor. Note that suboptimal transmission of tractions (slip) is also a source of rolling resistance.

The optimal tire design depends on the particular conditions in the desired application. For instance, trucks transporting goods on motorways bridge large distances at nearly constant speeds and on similar road profiles to which the tire's steady state behavior can be optimized. In this context, numerical simulations that take into account the different dissipative effects (rolling resistance contributions) can yield detailed insight into the tire's thermomechanical behavior, which is difficult to directly access by experiments. These simulations enable numerical testing and rapid optimization of new tire designs for specific rolling conditions. Accordingly, numerical simulations in conjunction with optimized prototype testing can significantly reduce costs of tire development. And yet, experimental testing is of course still inevitable for the validation of mathematical modeling.

A review on rolling resistance calculations including the effects of tread-road interaction

Different theoretical approaches to calculate rolling resistance can be found in literature. The most common technique is the finite element method (FEM), which has been successfully applied for the past three decades and is available in different commercial as well as open source software distributions. Apart from standard FEM-approaches there are different mathematical frameworks such as the waveguide-FEM (see e.g. [Hoever, 2012]) or semi-analytical models (see e.g. [Louhghalam et al., 2015]). Both approaches

allow for an estimation of rolling resistance and noise radiation that can be applied e.g. for the optimization of road surface textures. However, these models do not provide as detailed insight into the complex thermomechanical behavior of the tire's bulk material as can be obtained with the FEM, which is of crucial importance for the tire manufacturer in order to calculate phenomena such as grip, wear, damage, and failure. For further details on the development of tire simulation techniques the reader is referred to the review by [Ghoreishy, 2008].

Effective kinematic description

The first numerical framework enabling a detailed and efficient finite element (FE) solution of stationary rolling contact problems was introduced in [Oden and Lin, 1986]. In this contribution, rolling motion and relative deformation were decoupled using a a relative kinematic description, which forms the theoretical basis for most present FE-frameworks for rolling resistance calculations. Due to this separation, the material rotates within the reference configuration so that material particles are no longer fixed to the FE-mesh. Due to this fact, standard algorithms for the treatment of frictional contact and inelastic material behavior cannot be directly applied. However, first approaches to overcome these issues were already developed in this first contribution. A successive paper of the same research group [Oden et al., 1988] extended the formulation to the three-dimensional case. In addition, rough surface contact interaction was accounted for by an experimentally evaluated nonlinear contact compliance. The further elaboration by [Faria et al., 1992] also considered anisotropic fiber-reinforced rubber materials, which enabled the simulation of air-inflated tires. This framework provided a first attempt to compute tractive (accelerated, braking, and cornering) steady state rolling contact scenarios considering dominant sources of rolling resistance.

The parallels of a relative kinematic description to *Arbitrary Lagrangian Eulerian kinematics* (ALE-kinematics), which is applied e.g. in fluid structure interaction problems, were first recognized in [Nackenhorst, 1993]. The further elaboration of this framework resulted in a sound mathematical basis of ALE-kinematics for the rolling contact problem, see [Nackenhorst, 2000, 2004]. In the absence of friction, this formulation achieved a symmetric stiffness matrix even for C^0-continuous linear shape functions.

Tractive rolling contact

In [Oden and Lin, 1986] the authors also suggested a first approach to solve the tractive rolling contact problem, based on a penalization of slip velocities so that contact tractions can be calculated analogous to viscous damping. It can be regarded as a weak point of this approach that small penalty parameters result in a drift of material points in the contact

and therefore the stick condition cannot be fulfilled precisely. However, in the context of rubber friction, the friction coefficient tends to zero on nominally flat rough surfaces for small sliding speeds (see [Moore, 1972]). Due to this fact, the penalization of sliding velocities only serves for the calculation of the sliding direction (predictor step), the actual contact traction is calculated by the friction law, which results in a good approximation for practical tire simulations.

The first mathematically precise calculation of the stick-slip transition in frictional contact interaction was presented in [Nackenhorst, 2004]. This formulation can be verified by analytical reference solutions assuming Hertzian contact, see e.g. [Johnson, 1985]. A weak point of this approach was that only linear convergence rates of the solution were achieved. Both deficiencies have been overcome by the solution presented by [Ziefle, 2007; Ziefle and Nackenhorst, 2008], who defined the slip as an additional degree of freedom. This modification allows the stick condition to be directly enforced by standard algorithms for frictional contact, and yields quadratic convergence of the solution. The application of this framework also allows a direct application of arbitrary friction models formulated in *Lagrangian kinematics*, as will be demonstrated in the course of this thesis.

Inelastic material behavior in rolling tires

The efficient treatment of inelastic material behavior, especially of viscoelastic effects, in ALE-kinematic frameworks is still an open topic of research. In this context, the evolution equation for internal material history variables possesses both local and convective parts. [Oden and Lin, 1986] suggested an integration of the material history along spatially fixed streamlines in the reference configuration, which however suffered from accuracy issues and required several revolutions in order to obtain convergence. A first fully coupled treatment of this problem was presented by [Faria et al., 1992], who introduced a Fourier series expansion of the evolution equation along these stream lines. This expansion allowed for a direct calculation of the viscoelastic steady state response at the cost of introducing the Fourier coefficients as additional degrees of freedom, which results in a large non-symmetric system of equations, see [Nasdala et al., 1998; Nasdala, 2000] for further details and applications. Note that this method suffered considerably from its mesh dependence, requiring a post-error analysis as measure of ensuring mesh adaptivity.

Following established methods in ALE-kinematic frameworks (see [Donea et al., 2004]), [Ziefle, 2007; Ziefle and Nackenhorst, 2008] introduced a staggered algorithm to separate the treatment of the material history evolution into a local part and an advective transport of the internal variable. In order to solve this transport problem with minimal numerical diffusion and without limitations on the integration step size by stability criteria, the *time discontinuous Galerkin method* (TDG-method) was applied in this study. However,

a disadvantage of this staggered treatment was that even though the TDG-method is unconditionally stable, the size of the integration steps (angular increments) is limited by the governing problem. In order to gather all local sources of inelastic effects above the contact zone and their relaxation in the non-contact areas, the element sizes as well as the angular increments must be chosen sufficiently small, which causes the solution to be numerically expensive. A comparison of the TDG-method with a simplified unsplit streamline update procedure published in [Wollny and Kaliske, 2013] showed a good agreement of the computational results at reduced computational effort. This result is in accordance with the theoretical observations of [Govindjee and Mihalic, 1998], who stated that the influence of advection on the material history evolution is negligible if the cycle duration is large compared to the relaxation time. The unsplit streamline update procedure presented in [Wollny and Kaliske, 2013] was later used in [Behnke and Kaliske, 2015] to perform thermomechanical rolling resistance calculations. The obtained numerical results were validated with experimental measurements also presented in that contribution and a good agreement of both was found.

Recently, [Govindjee et al., 2014b] published a fully coupled framework that overcomes the mathematical issues of prior coupled approaches. The key idea lies in transferring the material history evolution into a spatial minimization problem, which has been presented first in [Le Tallec et al., 1994]. But instead of solving this problem using an upwind scheme, [Govindjee et al., 2014b] reformulated the material history evolution in terms of linearized dynamics. By means of this framework, the viscoelastic steady state response is obtained directly from a spatial minimization problem. In the present form, this treatment requires the introduction of tensor valued over-stresses as additional state variables, which results in a large non-symmetric stiffness matrix.

Thermomechanical coupling

In the past decades, different approaches to include thermal effects into the calculation of stationary rolling tires have been published, see e.g. the literature review by [Ghoreishy, 2008]. The theoretical basis for the thermomechanically coupled rolling resistance calculations in the present work was presented in [Suwannachit, 2013; Suwannachit and Nackenhorst, 2013]. This framework allows for the application of arbitrary constitutive material models to describe temperature dependent, viscoelastic rubber compounds. In addition, it enables the calculation of the temperature rise by viscous dissipation yielding the thermomechanical steady state response of frictionless rolling tires on a flat rigid surface. In this framework, the thermomechanical coupling was treated by the isentropic operator split scheme by [Armero and Simo, 1992], which allows for an unconditionally stable separation of the mechanical and the thermal subproblem.

Tread-road interaction in ALE-kinematics

A yet unsolved limitation in ALE-kinematic frameworks is the requirement of a rotation-symmetric mesh. Accordingly, studies are presently limited to the analysis of tires with circumferential grooves. A recent approach by [Govindjee et al., 2014a] describing the time periodic states of treaded rolling bodies has not yet been applied to more complex tread structures of tires. To date, the structural behavior of real tread patterns on flat surfaces can only be considered by using anisotropic homogenized constitutive material models, as presented in [Kaliske and Timmel, 2005]. Note that this response depends on service temperature, load and speed (frequency) of the tire, and of course on the random asperity distribution of the contacting rough surface for a single tread design made of a specific rubber compound. Therefore, the identification of the average tread-road interaction as a basis for formulating a constitutive contact model requires either extensive experimental testing (see e.g. [Huemer et al., 2001b] for experimental rubber friction evaluation) or a mathematical solution of the rough surface contact problem. In this context, the thermomechanical behavior of the deformable asphalt surface also influences on the obtained results. However, a rough rigid surface is assumed in this study.

Experimental rough surface contact evaluation

[Oden et al., 1988] suggested the first engineering approach to include a constitutive contact model describing the tread-road interaction, which was derived from experimental testing. A negative aspect of such models is that their material parameters often have no direct physical meaning, and therefore need to be identified by solving an inverse problem. For this reason and in order to reduce experimental costs, analytical or numerical models are to be preferred to experimental testing.

Analytical methods for rough surface contact

An analytical solution for rough surface contact problems was first presented in [Greenwood and Williamson, 1966]. The history of the further development of this class of models is described in detail in [Liu et al., 1999; Zmitrowicz, 2009; Chen, 2013b,a], and a comparative study of different methods can be found in [Zavarise et al., 2004]. To date, the most elaborated analytical solution, which describes rough surface contact as a diffusive process over the spectral surface representation, has been presented in [Persson, 2001]. In case of the presented examples, this approach is highly accurate up to nearly full contact, and has since been applied for thermomechanical contact and inelastic material behavior, see [Persson, 2006b]. However, analytical models are based on the assumption of contacting elastic half-spaces which restricts the solution to small deformations and simple material

models. Consequently, analytical models cannot describe the structural response of tread blocks contacting the rough road surface and their rolling resistance contribution, which is dominated by large deformations and complex material behavior.

Rubber friction is a microscale phenomenon (μm) in the contact interface between tread rubber and the penetrating mesoscale asperity (mm). Therefore, rubber friction can be approximated by analytical methods in case that only the microscale roughness is taken into account, see [Persson, 2006b; Lorenz et al., 2011; Popov et al., 2014].

Multi-scale homogenization techniques

The restrictions on kinematics and material behavior can be overcome in detailed finite element (FE) models, see e.g. [Bandeira et al., 2004] for an example of a unilateral constitutive contact model development based on the evaluation of rough surface contact scenarios. In these calculations, the contacting bodies are discretized with FE-meshes, which allows for an evaluation of stress in the bulk material as well as the structural response of the contact interaction. This insight comes at high numerical costs if small length scale roughness must be captured by fine mesh resolutions. In order to minimize these numerical costs, multi-scale methods can be introduced. Based on the assumption of separable scales, small scale roughness can be observed in detailed sub-models, which are subjected to admissible boundary conditions fulfilling the *Hill-criterion*. This method allows for either a consistent homogenization of the average microscale material behavior, or a direct coupling of micro- and macroscale problem in a single simulation using the so-called FE^2-method, see [Miehe, 2003; Geers et al., 2010] for further details.

Due to the contact with the rough surface, admissible boundary conditions allowing for the volumetric first-order homogenization described above cannot be defined. For this reason, the rough surface contact response is homogenized on an interface in order to obtain a consistent micro-to-macro transition. Based on these assumptions, [Wriggers and Nettingsmeier, 2007; Reinelt and Wriggers, 2010] evaluated the multi-scale homogenized friction response of a rubber block on a rough surface by upscaling the average tractions on relatively fine levels for a prescribed contact pressure. As a result of this study, material parameters for a pressure, temperature, and velocity (frequency) dependent friction model were identified. In [De Lorenzis and Wriggers, 2013] this work has been extended by application of isogeometric shape functions and the Mortar method, which enhanced the stability of the contact simulation. Note that the fractal character of road surfaces does not allow for separation of scales in general.

Following the classical homogenization theory, a representative contact element (RCE) was formulated in [Temizer and Wriggers, 2008], enabling a direct coupling by means of FE^2. In these studies, the averaged friction response accounting for the effect of moving

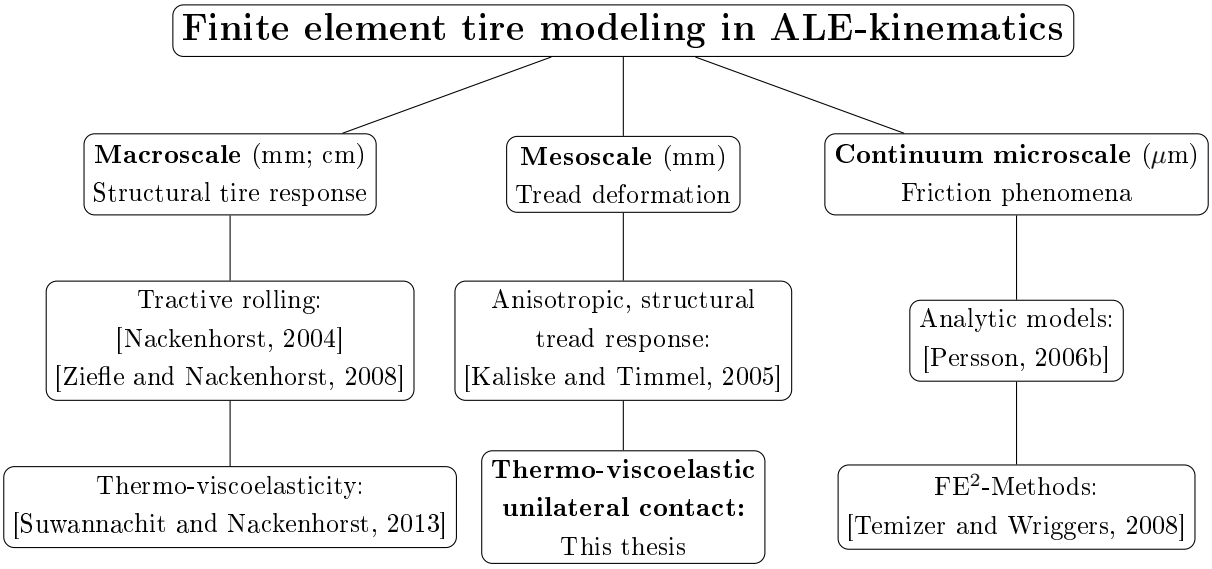

Figure 1.1: Relation of this thesis to the state of the art.

cylindrical third bodies in a two-dimensional contact interface was calculated. This approach was further elaborated introducing a thermodynamic consistent homogenization of viscoelastic effects to calculate the dissipation in the contact interface, see [Temizer and Wriggers, 2010a]. In order to estimate the average heat flux in rough surface contact interactions, [Temizer and Wriggers, 2010b] developed a thermomechanical extension of this contact homogenization framework.

The stochastic average tread-road contact interaction, which is required for the calculation of the stationary response, cannot be described by RCEs due to the fact that the autocorrelation length of rough road surfaces exceeds the size of tread blocks. Therefore, a direct coupling by means of FE^2 is not applicable to rolling resistance calculations.

Summarizing the outcomes of this literature review, a homogenized constitutive contact model accounting for the mesoscale stochastic average thermo-viscoelastic response of single tread blocks on rough road surfaces has not yet been developed. An energy-consistent representation of this contact behavior is required in order to quantify the influence of surface roughness on macroscale rolling resistance and is therefore highly relevant for the optimization of tread patterns. This thesis is meant to bridge this gap by providing a homogenized constitutive contact model, which enables to account for mesoscale tread-road interaction in macroscale rolling resistance calculations, see Figure 1.1.

Scope and structure of the thesis

The main objective of this thesis is the development of a one-dimensional constitutive contact model to represent the average thermomechanical contact interaction of a three-dimensional tread block on random rough road surfaces. This new approach is based on the tread's bulk material model and allows for precise calculations of average contact pressure and internal dissipation of tread blocks as a function of penetration depth, time (resulting in a prescribed penetration velocity or frequency), service temperature and a set of internal variables, which preserves the external energy in the load cycle (consistence of energy). The necessary solution steps for this homogenization problem are described in detail in this thesis. Thereby, the viscoelastic contact behavior of single tread blocks on optically measured road surfaces is characterized by numerical solution of the underlying stochastic contact problem. This result is obtained with a *Monte Carlo simulation*, in which the surface position is the random variable. The capability of representing viscoelastic rough surface contact interaction of tread blocks in macroscale models is validated by numerical studies of full scale models. Finally, rolling resistance calculations of rubber wheels and air-inflated radial tires accounting for thermomechanical tread-road interaction are performed by use of the developed constitutive contact model. The results of this study allow for a quantification of the influence of surface roughness on rolling resistance for the measured road profiles.

The basic continuum mechanics framework necessary for the definition of the described problem is summarized in **chapter 2**. Special focus is thereby put on the formulation of ALE-kinematics including the effect of thermal expansion.

The relevant material phenomena occurring in rubber materials as well as the chosen constitutive material model to depict these phenomena are briefly described in **chapter 3**. In addition, the behavior of the material model is illustrated in several numerical tests in order to allow for a better understanding of the subsequent results.

In **chapter 4** the theoretical background for the enforcement of contact constraints and the calculation of thermomechanical contact interaction is outlined. Here, the main issues are consistency of energy in the contact interface, and phenomenological friction models for rubber friction.

With these methods at hand, the homogenization of the random rough surface contact problem is addressed in **chapter 5**: First, the basic concepts for energy-consistent homogenization are briefly summarized, followed by the description of the constitutive contact model. Then, the mathematical problem for random rough surface contact is stated. By solving this problem, the average contact behavior of tread blocks on road

surfaces is obtained. In a next step, typical quantities for the characterization of rough surfaces are calculated for two measured asphalt surfaces. These surfaces serve as examples for rough and smooth road surfaces throughout this thesis. It is also demonstrated that moderate bandpass filtering can significantly reduce the numerical effort whilst retaining the mesoscopic contact behavior. In the last section of this chapter numerical examples are presented to illustrate the capability of the one-dimensional homogenized constitutive contact model to represent complex three-dimensional unilateral contact scenarios in an energy-consistent way. In addition, the results of the random rough surface contact problem are presented for two different tread geometries, and the parameters for the constitutive contact model are evaluated.

The obtained constitutive contact models describing the homogenized tread-road interaction, are then applied in thermomechanical rolling resistance calculations in **chapter 6**. Initially, a brief introduction on the numerical framework and its calculation algorithm is given, which was developed mainly based on the works of [Nackenhorst, 2000; Ziefle, 2007] and [Suwannachit, 2013]. In applying this framework, the influence of surface roughness on rolling resistance is investigated numerically for solid rubber wheels as well as for air-inflated radial tire models.

Finally, the results of this thesis are summarized and concluded in **chapter 7**. Furthermore, an outlook on further research is given.

2 Continuum thermomechanics

The calculation of rolling resistance requires a mathematical description of the involved coupled mechanical and thermal processes, which can be realized within the framework of continuum thermomechanics. This concept interprets arbitrarily shaped bodies as sets of continuously distributed media, rather than as discrete objects or sets of single atoms. Based on this assumption, engineering problems can be solved efficiently as it allows for a homogenized description of complex material phenomena.

The theoretical basis of this thesis largely originates from the detailed descriptions in the works of [Holzapfel, 2000; Nackenhorst, 2000; Liu, 2002; Haupt, 2002; Willner, 2003; Lubliner, 2006]. This chapter provides a short summary of continuum thermomechanics including the necessary aspects to formulate the mathematical problem and also serves to introduce the chosen notation. The key points of this chapter are the change of thermodynamic state, *Arbitrary Lagrangian Eulerian kinematics* in the realm of finite deformations, basic stress definitions, and the statement of the fundamental balance laws, which need to be fulfilled at all times in the following simulations.

2.1 Kinematics

Kinematics describes the motion of material particles in space and time. This descriptions is the basic requirement for a mathematical modeling of real world engineering problems. In the context of tire mechanics, the kinematic description must be suitable to cope with the occurring finite deformations and the large relative motions as well as the thermal expansion of the material. These complex phenomena can be described efficiently using *Arbitrary Lagrangian Eulerian kinematics* (ALE-kinematics), in which the body's motion is separated into a purely rotational contribution and a superimposed relative deformation. The ALE-kinematic description applied in this thesis is based on the ideas presented in the work of [Nackenhorst, 2004], which have since been used in [Ziefle, 2007; Suwannachit, 2013]. In the following sections, the mathematical description of the placement and the deformation of the material body is introduced, followed by definitions of strains and time derivatives of kinematic quantities.

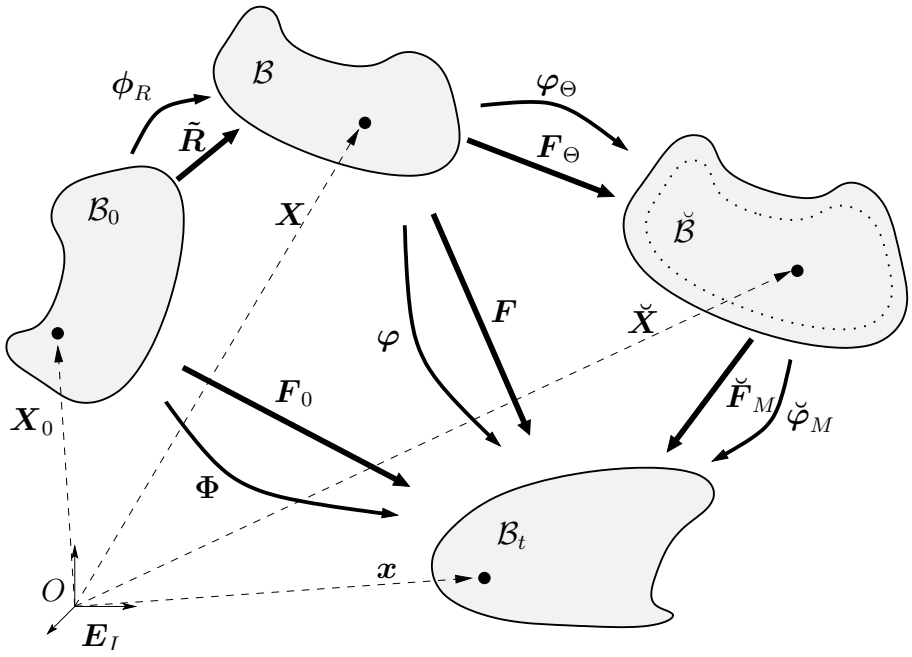

Figure 2.1: Material configuration $\mathcal{B}_0$, reference configuration $\mathcal{B}$, thermally expanded configuration $\breve{\mathcal{B}}$ and spatial configuration $\mathcal{B}_t$ of the material body.

2.1.1 Material body, configurations and motion

In continuum thermomechanics, the material body $\mathcal{B}$ is defined as a set of continuously distributed material points. For reasons of simplicity, the body is placed in the *Euclidean space* $\mathbb{E}^3$ in the present study, rather than using an arbitrary space definition. Any placement of the body $\mathcal{B}(t)$ at a fixed time t is called a configuration, in which each material point has a specific thermodynamic state.

The body's initial placement at time $t = t_0$ is assumed to be spatially fixed and referred to as the initial or material configuration $\mathcal{B}_0$ in the following. In this configuration the position of each material point is defined by a position vector $\boldsymbol{X}_0 = X_0^I \boldsymbol{E}_I (I = 1, 2, 3)$, where X_0^I are called material coordinates and the orthonormal base vectors $\boldsymbol{E}_I$ form a *Cartesian basis*. The related initial thermodynamic state of all material points is assumed to be stress-free and to have an initial temperature Θ_0.

The motion of the body is then regarded as a continuous process or series of configurations, which is described by a mapping $\boldsymbol{\Phi} : [t_0, t] \times \mathcal{B}_0 \to \mathbb{E}^3$. The actual placement at $t > t_0$ is called current or spatial configuration $\mathcal{B}_t$. Here, the material point has the position $\boldsymbol{x} = x^I \boldsymbol{E}_I (I = 1, 2, 3)$, with spatial coordinates x^I. Furthermore, the thermodynamic state of the material point in this instant is characterized by a spatial velocity $\boldsymbol{v}(\boldsymbol{x}) = \dot{\boldsymbol{\Phi}}(\boldsymbol{X}_0, t)$ and a temperature Θ.

The basic idea behind the description of large motions in ALE-kinematics lies in the

	Configuration			
	Material	Reference	Thermally expanded	Spatial
Symbol	$\mathcal{B}_0$	$\mathcal{B}$	$\breve{\mathcal{B}}$	$\mathcal{B}_t$
Variables	A_0	A	$\breve{A}$	a
Vectors	$\boldsymbol{N}_0$	$\boldsymbol{N}$	$\breve{\boldsymbol{N}}$	$\boldsymbol{n}$
Operators	GRAD	Grad	Grad_Θ	grad

Table 2.1: Notation convention [Suwannachit, 2013], modified.

introduction of an intermediate reference configuration, in which the convective material transport is traced in *Eulerian kinematics*. A *Lagrangian observer* that is fixed to this configuration then only describes the relative motion of the body. In the special case of a rolling motion the reference configuration is defined by a rigid body rotation $\mathcal{B} = \boldsymbol{\phi}_R(\mathcal{B}_0, t)$ of the initial configuration, which does not induce any stresses. The position $\boldsymbol{X} = X^I \boldsymbol{E}_I (I = 1, 2, 3)$ of the material point in this configuration is then defined by referential coordinates X^I.

In the context of thermomechanical simulations, the change of temperature $\Delta\Theta = \Theta - \Theta_0$ is accompanied by thermal expansion. In order to separate this effect from the mechanical deformation, [Lu and Pister, 1975] introduced an additional intermediate configuration $\breve{\mathcal{B}} = \boldsymbol{\varphi}_\Theta(\mathcal{B}(t), \Theta)$ using a multiplicative split of the deformation gradient. Here, the thermal expansion is assumed to be an isotropic volumetric extension, which is also to be stress-free if it is not restricted by boundary conditions. Note that the mapping $\boldsymbol{\varphi}_\Theta(\boldsymbol{X}, \Theta)$ is solely induced by the change of temperature. The remainder $\breve{\boldsymbol{\varphi}}_M\left(\breve{\boldsymbol{X}}, t\right)$ is referred to as effective mechanical motion. This formulation was applied in the models of [Heimes, 2005; Höfer, 2009], from which the present notation has been adapted.

The definition of these configurations enables a separation of the mapping

$$\boldsymbol{\Phi} = \boldsymbol{\varphi} \circ \boldsymbol{\phi}_R = \breve{\boldsymbol{\varphi}}_M \circ \boldsymbol{\varphi}_\Theta \circ \boldsymbol{\phi}_R, \tag{2.1}$$

which projects points from the material into the current configuration. In this equation the mapping $\boldsymbol{\varphi} : \mathcal{B} \times [t_0, t] \to \mathbb{E}^3$ describes the superimposed relative motion to the rotating reference configuration $\mathcal{B} = \boldsymbol{\phi}_R(\mathcal{B}_0, t)$ in ALE-kinematics. The relative deformations can be separated into a mapping $\breve{\boldsymbol{\varphi}}_M : \breve{\mathcal{B}} \times [t_0, t] \to \mathbb{E}^3$, which describes the purely mechanical deformation and a thermal expansion $\boldsymbol{\varphi}_\Theta : \mathcal{B} \times [\Theta_0, \Theta] \to \mathbb{E}^3$.

The relation of the different configurations and mappings is illustrated in Figure 2.1, and the notation of the most important quantities and operators is summarized in Table 2.1.

2.1.2 Displacement

The material displacement field

$$\boldsymbol{u}_0(\boldsymbol{X}_0, t) = \boldsymbol{x}(\boldsymbol{X}_0, t) - \boldsymbol{X}_0 \tag{2.2}$$

is a vector field, which relates the position of a material point in the initial configuration to its location in the current configuration. This displacement needs to be distinguished from the reference displacement field

$$\boldsymbol{u}(\boldsymbol{X}, t) = \boldsymbol{x}(\boldsymbol{X}, t) - \boldsymbol{X}(\boldsymbol{X}_0, t), \tag{2.3}$$

which is a mapping based on positions in the reference configuration. Note that if the motion has no convective contribution, both fields coincide.

2.1.3 Deformation gradient

The change in shape of a material body, i.e. the deformation of material lines and curves, is often quantified by the deformation gradient in continuum thermomechanics. This second-order, two-field tensor is generally introduced as a mapping of an incremental line element $\mathrm{d}\boldsymbol{X}_0$ in the material configuration onto the same line element $\mathrm{d}\boldsymbol{x}$ in the current configuration

$$\mathrm{d}\boldsymbol{x}(\boldsymbol{X}_0, t) = \boldsymbol{F}_0(\boldsymbol{X}_0, t)\mathrm{d}\boldsymbol{X}_0. \tag{2.4}$$

In the general concept of ALE-kinematics, the deformation gradient

$$\boldsymbol{F}_0(\boldsymbol{X}_0, t) = \boldsymbol{F}(\boldsymbol{X}, t) \cdot \tilde{\boldsymbol{R}}(\boldsymbol{X}_0, t) \tag{2.5}$$

is split multiplicatively into a convective material motion $\tilde{\boldsymbol{R}}$ and a motion $\boldsymbol{F}$ relative to the reference configuration. In the special case of rolling motions, $\tilde{\boldsymbol{R}}$ has been introduced in [Nackenhorst, 2000] as a purely rigid body rotation with an angular velocity $\omega(t)$ around a fixed axis. In this thesis, the rotation axis coincides with the third base vector $\boldsymbol{E}_3$ and therefore, the rotation tensor takes the form

$$\tilde{\boldsymbol{R}}_3(\omega_3(t), t) = \begin{pmatrix} \cos(\omega_3(t)t) & -\sin(\omega_3(t)t) & 0 \\ \sin(\omega_3(t)t) & \cos(\omega_3(t)t) & 0 \\ 0 & 0 & 1 \end{pmatrix}. \tag{2.6}$$

The *Lagrangian observer*, which can be regarded as fixed to the axis of rotation in this framework, perceives the relative velocity of the ground and the deformation of the reference configuration $\boldsymbol{F}$. Due to the fact that only the relative part describes a deformation of the material and all quantities are defined with respect to the reference configuration in the following, the term deformation gradient will from here on refer to the relative part.

The deformation gradient $\boldsymbol{F}$ is calculated as the partial derivative of the relative motion $\boldsymbol{\varphi}$ with respect to the coordinates of the reference configuration $\boldsymbol{X}$ as

$$\boldsymbol{F} = \frac{\partial \boldsymbol{\varphi}(\boldsymbol{X}, t)}{\partial \boldsymbol{X}} = \frac{\partial x_i}{\partial X_j} = \mathrm{Grad}\boldsymbol{x}. \tag{2.7}$$

With the definition of the material displacement field (2.3), the deformation gradient can also be expressed via

$$\boldsymbol{F} = \mathrm{Grad}(\boldsymbol{X} + \boldsymbol{u}) = \mathbf{1} + \boldsymbol{H} \text{ with } \boldsymbol{H} = \mathrm{Grad}\boldsymbol{u}, \tag{2.8}$$

where the tensor $\boldsymbol{H}$ denotes the displacement gradient.

The introduction of a thermally expanded configuration is realized by a further multiplicative decomposition of the deformation gradient

$$\boldsymbol{F} = \breve{\boldsymbol{F}}_M \cdot \boldsymbol{F}_\Theta = \frac{\partial \boldsymbol{x}}{\partial \breve{\boldsymbol{X}}} \cdot \frac{\partial \breve{\boldsymbol{X}}}{\partial \boldsymbol{X}}, \tag{2.9}$$

which allows for a distinction of the thermal expansion $\boldsymbol{F}_\Theta$ and the purely mechanical deformation $\boldsymbol{F}_M$. A thorough discussion on the advantages and disadvantages of possible sequences to introduce an intermediate thermal configuration, namely $\boldsymbol{F} = \breve{\boldsymbol{F}}_M \cdot \boldsymbol{F}_\Theta = \boldsymbol{F}_\Theta \cdot \breve{\boldsymbol{F}}_M$, has been published in [Hartmann, 2012]. In the context of ALE-kinematics the chosen sequence (2.9) appears to be most convenient.

Following [Höfer, 2009], the assumed isotropic thermal expansion is modeled by a scalar function $\varphi_\Theta(\Theta)$. This formulation was presented first in [Lu and Pister, 1975], in which the thermal deformation gradient was defined as

$$\boldsymbol{F}_\Theta = \varphi_\Theta^{\frac{1}{3}}(\Theta)\mathbf{1}. \tag{2.10}$$

The *Jacobian determinant* $J = \det(F)$ maps an infinitely small volume element in the reference configuration onto the current configuration

$$\mathrm{d}v = J\,\mathrm{d}V, \tag{2.11}$$

and can therefore be used as a measure for volume change. The introduction of intermediate configurations also enables a decomposition of the *Jacobian determinant*

$$J_0 = J = \varphi_\Theta\, J_M, \tag{2.12}$$

where the first equality results from the assumption of a rigid body motion. In the reference configuration the *Jacobian determinant* can be separated into a thermal part φ_Θ and an effective mechanical part J_M.

2.1.4 Strain measures

The objective calculation of stresses in terms of constitutive material models requires frame invariant strain measures. The deformation gradient (2.7) as a two-field tensor is generally non-symmetric and does not fulfill this requirement. Therefore, the *right Cauchy-Green tensor* is introduced in the rotating reference configuration as

$$\boldsymbol{C} = \boldsymbol{F}^{\mathrm{T}} \cdot \boldsymbol{F}, \text{ with } \det(\boldsymbol{C}) = J^2, \tag{2.13}$$

which results in a symmetric, objective deformation measure in this configuration. Furthermore, it contains information about the stretch

$$\lambda = \sqrt{\boldsymbol{e} \cdot \boldsymbol{C} \cdot \boldsymbol{e}}, \text{ where } \boldsymbol{e} = \frac{\mathrm{d}\boldsymbol{X}}{|\mathrm{d}\boldsymbol{X}|} \tag{2.14}$$

is the normalized direction of the material line element $\mathrm{d}\boldsymbol{X}$. For the formulation of frame invariant constitutive material models, the invariants of the *right Cauchy-Green tensor*

$$I_C = \mathrm{tr}(\boldsymbol{C}) = \lambda_1^2 + \lambda_2^2 + \lambda_3^2 \tag{2.15}$$

$$II_C = \frac{1}{2}\left(\mathrm{tr}(\boldsymbol{C})^2 - \mathrm{tr}\left(\boldsymbol{C}^2\right)\right) = \mathrm{tr}(C)^{-1}\det(\boldsymbol{C}) = \lambda_1^2\lambda_2^2 + \lambda_2^2\lambda_3^2 + \lambda_1^2\lambda_3^2 \tag{2.16}$$

$$III_C = \det(\boldsymbol{C}) = \lambda_1^2\lambda_2^2\lambda_3^2 \tag{2.17}$$

are of particular importance. Both the tensor notation and the form using principal stretches λ_i (square root of the *eigenvalues* of $\boldsymbol{C}$) are valid in arbitrary coordinate systems.

In order to enable the application of constitutive material models formulated in the regime of finite deformations at isothermal conditions, the purely mechanical deformation is extracted with respect to the thermally expanded intermediate configuration. Here, the effective, mechanical *right Cauchy-Green tensor* takes the form

$$\breve{\boldsymbol{C}}_M = \varphi_\Theta^{-\frac{2}{3}} \boldsymbol{C}. \tag{2.18}$$

A further important quantity in material modeling is the *Green-Lagrange strain*

$$\boldsymbol{E} = \frac{1}{2}\left(\boldsymbol{F}^{\mathrm{T}} \cdot \boldsymbol{F} - \boldsymbol{1}\right) = \frac{1}{2}(\boldsymbol{C} - \boldsymbol{1}) = \frac{1}{2}\left(\boldsymbol{H} + \boldsymbol{H}^{\mathrm{T}} + \boldsymbol{H}^{\mathrm{T}} \cdot \boldsymbol{H}\right), \tag{2.19}$$

which is defined in the rotating reference configuration as a nonlinear equivalent to the engineering strain. It follows from (2.9) that the *Green-Lagrange strain* can be separated into a thermal $\boldsymbol{E}_\Theta$ and a mechanical contribution $\boldsymbol{E}_M$, which yields

$$\boldsymbol{E}_\Theta = \frac{1}{2}\left(\boldsymbol{F}_\Theta^{\mathrm{T}} \cdot \boldsymbol{F}_\Theta - \boldsymbol{1}\right) \tag{2.20}$$

$$\boldsymbol{E}_M = \frac{1}{2}\left(\boldsymbol{F}^{\mathrm{T}} \cdot \boldsymbol{F} - \boldsymbol{F}_\Theta^{\mathrm{T}} \cdot \boldsymbol{F}_\Theta\right). \tag{2.21}$$

Its connection to the initial configuration is given by

$$\boldsymbol{E} = \tilde{\boldsymbol{R}}^{-\mathrm{T}} \cdot \boldsymbol{E}_0 \cdot \tilde{\boldsymbol{R}}^{-1} = \tilde{\boldsymbol{R}} \cdot \boldsymbol{E}_0 \cdot \tilde{\boldsymbol{R}}^{\mathrm{T}}, \tag{2.22}$$

where the second term is valid due to the orthogonality of the rotation tensor $\boldsymbol{R}^{\mathrm{T}} = \boldsymbol{R}^{-1}$.

2.1.5 Material time derivatives

In isothermal ALE-kinematics, the material time derivative of an arbitrary spatial quantity $f(\boldsymbol{x},t) = f(\boldsymbol{\varphi}(\boldsymbol{X},t),t)$ takes the form

$$\left.\frac{\mathrm{d}f(\boldsymbol{x},t)}{\mathrm{d}t}\right|_{\boldsymbol{X}_0} = \left.\frac{\partial f}{\partial t}\right|_{\boldsymbol{X}} + \left.\frac{\partial f}{\partial \boldsymbol{X}}\right|_{t} \cdot \left.\frac{\mathrm{d}\boldsymbol{X}}{\mathrm{d}t}\right|_{\boldsymbol{X}_0} = \left.\frac{\partial f}{\partial t}\right|_{\boldsymbol{X}} + \mathrm{Grad} f \cdot \boldsymbol{w} \tag{2.23}$$

Here, the first term can be interpreted as the local evolution or relative change of f, and the second term as its convective transport in the reference configuration.

In this thesis, this general form of the time derivative is restricted to the case of stationary rolling motions, for which a rigid body rotation $\boldsymbol{\omega}(t) = \boldsymbol{\omega}$ at constant angular velocity is assumed. Due to this assumption, a material point in the reference configuration moves with the guiding velocity

$$\boldsymbol{w} = \left.\frac{\mathrm{d}\boldsymbol{X}}{\mathrm{d}t}\right|_{\boldsymbol{X}_0} = \boldsymbol{X} \times \boldsymbol{\omega} = \boldsymbol{X} \cdot \begin{bmatrix} 0 & -\omega_3 & 0 \\ \omega_3 & 0 & 0 \\ 0 & 0 & 0 \end{bmatrix}, \tag{2.24}$$

see [Nackenhorst, 2000] for further details. Note that the local evolution or relative change of the quantity f vanishes for any process

$$\lim_{t\to\infty} \left.\frac{\partial f}{\partial t}\right|_{\boldsymbol{X}} \stackrel{!}{=} 0 \tag{2.25}$$

when approaching the stationary state.

The application of (2.23) on the spatial displacement yields the velocity field

$$\boldsymbol{v}(\boldsymbol{x},t) = \left.\frac{\mathrm{d}\boldsymbol{u}_0(\boldsymbol{x},t)}{\mathrm{d}t}\right|_{\boldsymbol{X}_0} = \left.\frac{\partial \boldsymbol{\varphi}}{\partial t}\right|_{\boldsymbol{X}} + \mathrm{Grad}\boldsymbol{\varphi} \cdot \boldsymbol{w} = \hat{\boldsymbol{v}} + \boldsymbol{c}, \tag{2.26}$$

in which a relative $\hat{\boldsymbol{v}}$ and a convective velocity $\boldsymbol{c}$ can be distinguished. For stationary motions, the relative velocity $\hat{\boldsymbol{v}}$ vanishes according to (2.25). This effect can also be observed in experiments in which tires seem to have a constant shape whilst rolling on the test drum. Following this assumption, the material time derivative (2.23) of the velocity field $\boldsymbol{v}(\boldsymbol{x},t)$ defines the acceleration field of a body in stationary rolling motion via

$$\boldsymbol{a}(\boldsymbol{x},t) = \left.\frac{\mathrm{d}\boldsymbol{v}(\boldsymbol{x},t)}{\mathrm{d}t}\right|_{\boldsymbol{X}_0} = \mathrm{Grad}\left(\mathrm{Grad}\boldsymbol{\varphi} \cdot \boldsymbol{w}\right) \cdot \boldsymbol{w}, \tag{2.27}$$

see [Nackenhorst, 2000] for details.

The introduced thermally expanded configuration allows for the direct application of standard material models, which are formulated in the isothermal regime. The effective

mechanical motion $\breve{\boldsymbol{F}}_M$ observed in this configuration is the same as for isothermal processes. For this purpose, the material time derivative (2.23) needs to be separated into its thermal and its mechanical contributions, which results in

$$\begin{aligned}\left.\frac{\mathrm{d}g(\boldsymbol{x},t)}{\mathrm{d}t}\right|_{\boldsymbol{X}_0} &= \left.\frac{\partial g}{\partial t}\right|_{\breve{\boldsymbol{X}}} + \frac{\partial g}{\partial \breve{\boldsymbol{X}}} \cdot \left.\frac{\mathrm{d}\breve{\boldsymbol{X}}}{\mathrm{d}t}\right|_{\boldsymbol{X}_0} \\ &= \left.\frac{\partial g}{\partial t}\right|_{\breve{\boldsymbol{X}}} + \frac{\partial g}{\partial \breve{\boldsymbol{X}}} \cdot \left(\boldsymbol{F}_\Theta \cdot \boldsymbol{w} + \frac{\partial \boldsymbol{\varphi}_\Theta}{\partial \Theta} \cdot \left(\left.\frac{\partial \Theta}{\partial t}\right|_{\boldsymbol{X}} + \mathrm{Grad}\Theta \cdot \boldsymbol{w}\right)\right) \quad (2.28)\end{aligned}$$

$$\text{with} \quad \left.\frac{\mathrm{d}\breve{\boldsymbol{X}}}{\mathrm{d}t}\right|_{\boldsymbol{X}_0} = \left.\frac{\mathrm{d}\boldsymbol{\varphi}_\Theta(\boldsymbol{X},\Theta)}{\mathrm{d}t}\right|_{\boldsymbol{X}_0} = \frac{\partial \boldsymbol{\varphi}_\Theta}{\partial \boldsymbol{X}} \cdot \left.\frac{\mathrm{d}\boldsymbol{X}}{\mathrm{d}t}\right|_{\boldsymbol{X}_0} + \frac{\partial \boldsymbol{\varphi}_\Theta}{\partial \Theta} \cdot \left.\frac{\mathrm{d}\Theta}{\mathrm{d}t}\right|_{\boldsymbol{X}_0} \quad (2.29)$$

for an arbitrary spatial quantity $g(\boldsymbol{x},t) = g\left(\boldsymbol{\varphi}_M\left(\breve{\boldsymbol{X}},t\right),t\right)$. Here, (2.29) follows from the assumption of isotropic thermal expansion. The contributions can be understood as the pure convective speed in the expanded configuration $\boldsymbol{F}_\Theta \cdot \boldsymbol{w}$ and the expansion velocity $\frac{\partial \boldsymbol{\varphi}_\Theta}{\partial \Theta}\dot{\Theta}$. The two different contributions are not distinguished in the material time derivative (2.23) with respect to the rotating reference configuration. For stationary motions, the relative changes $\left.\frac{\partial g}{\partial t}\right|_{\breve{\boldsymbol{X}}}$ and $\left.\frac{\partial \Theta}{\partial t}\right|_{\boldsymbol{X}}$ vanish according to (2.25).

2.1.6 Deformation rates

The description of the evolution of deformation processes, which is related to mechanical power, can be realized by introducing rates of strain tensors. In this thesis, the required quantities to formulate balance equations in the rotating reference configuration are the referential velocity gradient $\boldsymbol{L}$ describing the rate of change of the deformation gradient, and the rate of *Green-Lagrange strain* $\dot{\boldsymbol{E}}$. Here, the referential velocity gradient in stationary rolling motion is defined as

$$\boldsymbol{L} = \frac{\partial \boldsymbol{v}}{\partial \boldsymbol{X}} = \mathrm{Grad}\boldsymbol{v} = \dot{\boldsymbol{F}} + \boldsymbol{F} \cdot \boldsymbol{\Omega} \quad (2.30)$$

in which $\boldsymbol{\Omega} = \dot{\tilde{\boldsymbol{R}}} \cdot \tilde{\boldsymbol{R}}^{\mathrm{T}}$ is a skew symmetric tensor containing the angular velocity, see [Nackenhorst, 2000]. The rate of *Green-Lagrange strain* with respect to the stationary rotating reference configuration is introduced by

$$\begin{aligned}\dot{\boldsymbol{E}} &= \frac{1}{2}\left(\dot{\boldsymbol{F}}^{\mathrm{T}} \cdot \boldsymbol{F} + \boldsymbol{F}^{\mathrm{T}} \cdot \dot{\boldsymbol{F}} + \boldsymbol{F}^{\mathrm{T}} \cdot \boldsymbol{F} \cdot \boldsymbol{\Omega} - \boldsymbol{\Omega} \cdot \boldsymbol{F}^{\mathrm{T}} \cdot \boldsymbol{F}\right) \\ &= \frac{1}{2}\left(\dot{\boldsymbol{C}} + \boldsymbol{C} \cdot \boldsymbol{\Omega} - \boldsymbol{\Omega} \cdot \boldsymbol{C}\right). \quad (2.31)\end{aligned}$$

Analogous to the strain measures, the referential velocity gradient can also be decomposed into a mechanical part $\breve{\boldsymbol{L}}_M = \boldsymbol{L} \cdot \breve{\boldsymbol{L}}_\Theta{}^{-1}$ and a thermal part

$$\breve{\boldsymbol{L}}_\Theta = \dot{\boldsymbol{F}}_\Theta \cdot \boldsymbol{F}_\Theta^{-1} = \frac{\varphi'_\Theta}{3\varphi_\Theta}\dot{\Theta}\boldsymbol{1} \quad \text{with} \quad \varphi'_\Theta = \frac{\mathrm{d}\varphi_\Theta}{\mathrm{d}\Theta}. \quad (2.32)$$

This formulation of the thermal velocity gradient is based on the assumption of isotropic thermal expansion, see [Höfer, 2009]. By means of this definition, the rate of the mechanical part of the *right Cauchy-Green tensor* can be calculated via

$$\breve{\dot{\boldsymbol{C}}}_M = -\frac{2\varphi'_\Theta}{3\varphi_\Theta}\breve{\boldsymbol{C}}_M + \varphi_\Theta^{-\frac{2}{3}}\dot{\boldsymbol{C}}. \tag{2.33}$$

By using (2.18), the rate of the *Green-Lagrange strain* $\dot{\boldsymbol{E}}$ can then be separated into its mechanical and thermal contributions

$$\begin{aligned}\dot{\boldsymbol{E}} = \frac{1}{2}\dot{\boldsymbol{C}} &= \frac{1}{2}\left(\dot{\boldsymbol{F}}_\Theta^{\mathrm{T}}\cdot\breve{\boldsymbol{C}}_M\cdot\boldsymbol{F}_\Theta + \boldsymbol{F}_\Theta^{\mathrm{T}}\cdot\breve{\boldsymbol{C}}_M\cdot\dot{\boldsymbol{F}}_\Theta + \boldsymbol{F}_\Theta^{\mathrm{T}}\cdot\breve{\dot{\boldsymbol{C}}}_M\cdot\boldsymbol{F}_\Theta\right)\\ &= \frac{1}{2}\boldsymbol{F}_\Theta^{\mathrm{T}}\cdot\left(\breve{\boldsymbol{L}}_\Theta^{\mathrm{T}}\cdot\breve{\boldsymbol{C}}_M + \breve{\boldsymbol{C}}_M\cdot\breve{\boldsymbol{L}}_\Theta + \breve{\dot{\boldsymbol{C}}}_M\right)\cdot\boldsymbol{F}_\Theta.\end{aligned} \tag{2.34}$$

2.2 Stress definitions

The traction vector $\boldsymbol{t}$ is defined as incremental force $\mathrm{d}\boldsymbol{f}$ per incremental area $\mathrm{d}a$ in the current configuration and is related to the *Cauchy stress tensor* $\boldsymbol{\sigma}$ by the *Cauchy theorem*

$$\boldsymbol{t} = \frac{\mathrm{d}\boldsymbol{f}}{\mathrm{d}a} = \boldsymbol{\sigma}\cdot\boldsymbol{n}. \tag{2.35}$$

Using *Nanson's formula* $J\boldsymbol{F}^{-\mathrm{T}}\cdot\boldsymbol{N}\,\mathrm{d}A = \boldsymbol{n}\,\mathrm{d}a$ the nominal traction vector $\boldsymbol{T}$ can be defined as the incremental force $\mathrm{d}\boldsymbol{f}$ per incremental area $\mathrm{d}A$ in the reference configuration, which is related to the *first Piola-Kirchhoff stress tensor* $\boldsymbol{P}$ via

$$\boldsymbol{T} = \frac{\mathrm{d}\boldsymbol{f}}{\mathrm{d}A} = \boldsymbol{P}\cdot\boldsymbol{N}. \tag{2.36}$$

In order to obtain a symmetric representation, the *second Piola-Kirchhoff stress tensor* is introduced as

$$\boldsymbol{S} = \boldsymbol{F}^{-1}\cdot\boldsymbol{P}, \tag{2.37}$$

which is entirely defined in the reference configuration, but has no direct physical meaning.

2.3 Balance principles

In continuum mechanics, balance principles ensure physical consistency and therefore must be fulfilled at all times. In this section, a short overview of related balance principles is given, with special emphasis on thermomechanical problems. For a more detailed discussion the reader is referred to [Holzapfel, 2000; Willner, 2003].

2.3.1 Balance of mass

The balance of mass describes the change of mass in a body. As no wear or other abrasive effects are taken into account in this work, the mass m is assumed to be constant over time, which results in

$$m = \int_{\mathcal{B}_0} \varrho_0 \, \mathrm{d}V = \int_{\mathcal{B}} \varrho \, \mathrm{d}V = \int_{\breve{\mathcal{B}}} \breve{\varrho} \, \mathrm{d}\breve{V} = \int_{\mathcal{B}_t} \varrho_t \, \mathrm{d}v \stackrel{!}{=} \text{const.}, \tag{2.38}$$

where $\varrho_0, \varrho, \breve{\varrho}$ and ϱ_t are the mass densities within the different configurations. Due to the assumptions on stationary rolling motions introduced in subsection 2.1.1, the mass densities are related via

$$\varrho_0(\boldsymbol{X}_0) = \varrho(\boldsymbol{X}, t) = \varphi_\Theta(\Theta)\breve{\varrho}\left(\breve{\boldsymbol{X}}, t\right) = \varphi_\Theta(\Theta) J_M(\boldsymbol{x}, t)\varrho_t(\boldsymbol{x}, t), \tag{2.39}$$

where the initial density ϱ_0 is only affected by thermal expansion and volume changes resulting from mechanical deformations.

2.3.2 Balance of linear and angular momentum

The balance of linear and angular momentum relates the changes of momentum of a system to the acting forces and torques. In the stationary rotating reference configuration the local form of the balance of linear momentum is defined as

$$\varrho\dot{\boldsymbol{v}} = \mathrm{Div}\boldsymbol{P} + \varrho\boldsymbol{b}. \tag{2.40}$$

As shown e.g. in [Holzapfel, 2000], the balance of angular momentum implies the symmetry of the *Cauchy stress tensor* as well as for the *second Piola-Kirchhoff stress tensor*

$$\boldsymbol{\sigma} = \boldsymbol{\sigma}^{\mathrm{T}} \quad \text{and} \quad \boldsymbol{S} = \boldsymbol{S}^{\mathrm{T}}. \tag{2.41}$$

2.3.3 Balance of energy

For the description of thermomechanical systems, the balance of energy, also known as the *first law of thermodynamics*, relates the change of internal energy $\dot{e}$ to the sum of acting mechanical and thermal power. Its local form in the rotating reference configuration reads

$$\varrho\dot{e} \;\; = \;\; \boldsymbol{S} : \dot{\boldsymbol{E}} - \mathrm{Div}\boldsymbol{Q} + \varrho r, \tag{2.42}$$

where $\boldsymbol{S} : \dot{\boldsymbol{E}}$ is the mechanical stress power, $\boldsymbol{Q}$ denotes the heat flux, and r symbolizes internal heat sources. This equality needs to be fulfilled in all configurations and can be transferred by making use of the work conjugated pairs

$$\boldsymbol{S} : \dot{\boldsymbol{E}} = \boldsymbol{P} : \dot{\boldsymbol{F}} = J\boldsymbol{\sigma} : \boldsymbol{d}. \tag{2.43}$$

The general validity of these transformations is proven in [Holzapfel, 2000]. In this statement $\boldsymbol{d} = \frac{1}{2}\left(\mathrm{grad}\boldsymbol{v} + \mathrm{grad}^{\mathrm{T}}\boldsymbol{v}\right)$ is called the symmetric rate of deformation tensor.

With (2.34), the stress power $\mathcal{P} = \boldsymbol{S} : \dot{\boldsymbol{E}}$ in the reference configuration is separated into a purely mechanical part $\mathcal{P}_M$ and a thermal contribution $\mathcal{P}_\Theta$ that stems from the isotropic thermal expansion, which yields

$$\mathcal{P} = \breve{\boldsymbol{S}}_M : \dot{\breve{\boldsymbol{E}}}_M + \breve{\boldsymbol{S}}_M : \breve{\boldsymbol{C}}_M \cdot \breve{\boldsymbol{L}}_\Theta = \breve{\boldsymbol{S}}_M : \dot{\breve{\boldsymbol{E}}}_M + \frac{\varphi'_\Theta}{3\varphi_\Theta}\dot{\Theta}\breve{\boldsymbol{S}}_M : \breve{\boldsymbol{C}}_M = \mathcal{P}_M + \mathcal{P}_\Theta, \quad (2.44)$$

where the transformations $\breve{\boldsymbol{S}}_M = \varphi_\Theta^{\frac{2}{3}}\boldsymbol{S}$ and (2.18) were applied. By means of this equivalence, the local form of balance of energy (2.42) can be reformulated as

$$\varrho\dot{e} = \breve{\boldsymbol{S}}_M : \dot{\breve{\boldsymbol{E}}}_M + \frac{\varphi'_\Theta}{3\varphi_\Theta}\dot{\Theta}\breve{\boldsymbol{S}}_M : \breve{\boldsymbol{C}}_M - \mathrm{Div}\boldsymbol{Q} + \varrho r. \quad (2.45)$$

Note that the thermal stress power is zero in case of unrestricted thermal expansion.

2.3.4 Entropy inequality

The entropy inequality ensures that the solution of the balance of energy is physically consistent and results in a maximum of entropy s in the system. The local form of the entropy inequality with respect to the rotating reference configuration takes the form

$$\varrho\Theta\dot{s} + \mathrm{Div}\boldsymbol{Q} - \frac{1}{\Theta}\boldsymbol{Q} \cdot \mathrm{Grad}\Theta - \varrho r \geq 0. \quad (2.46)$$

This inequality can be related to the balance of energy (2.42) by using the mass-specific *Helmholtz free energy*

$$\psi = e - \Theta s, \quad \text{where} \quad \dot{\psi} = \dot{e} - \dot{\Theta}s - \Theta\dot{s} \quad (2.47)$$

is the time derivative, which is obtained by *Legendre transformation*. With this definition, the entropy inequality in the reference configuration reads

$$\boldsymbol{S} : \dot{\boldsymbol{E}} - \varrho\left(\dot{\psi} + \dot{\Theta}s\right) - \frac{1}{\Theta}\boldsymbol{Q} \cdot \mathrm{Grad}\Theta \;\geq\; 0. \quad (2.48)$$

With the separation of the stress power (2.44) into a mechanical and a thermal contribution, the balance of energy (2.48) can be reformulated into a heat conduction equation

$$\begin{aligned} \varrho\Theta\dot{s} &= \mathcal{D}_{int} - \mathrm{Div}\boldsymbol{Q} + \varrho r, \\ \text{with } \mathcal{D}_{int} &= \breve{\boldsymbol{S}}_M : \dot{\breve{\boldsymbol{E}}}_M + \frac{\varphi'_\Theta}{3\varphi_\Theta}\dot{\Theta}\breve{\boldsymbol{S}}_M : \breve{\boldsymbol{C}}_M - \varrho\left(\dot{\psi} + \dot{\Theta}s\right) - \frac{1}{\Theta}\boldsymbol{Q} \cdot \mathrm{Grad}\Theta \geq 0. \end{aligned} \quad (2.49)$$

This inequality needs to be fulfilled by any objective constitutive material model. Its fulfillment for the material model used in this thesis is shown in the next chapter.

3 Constitutive modeling of rubber materials

The precise calculation of rolling resistance requires a suitable material model that depicts the dominant nonlinear characteristics of tire rubber at steady state conditions. The continuum modeling of these phenomena is a wide and highly active field of research due to the economical importance of rubber materials. A broad overview on modeling approaches is given in the literature reviews by [Mackerle, 1998, 2004; Puglisi and Saccomandi, 2016].

In this thesis, the behavior of tire rubber compounds is described by an extension of the thermo-viscoelastic material model presented in [Suwannachit, 2013] (see chapter 6) and [Suwannachit and Nackenhorst, 2013], which is mainly based on the work of [Holzapfel and Simo, 1996a]. That model has been an extended by a strict separation of mechanical and thermal deformation presented in [Lu and Pister, 1975], which was applied in [Heimes, 2005; Höfer, 2009]. The present material model accounts for the characteristic nonlinear stress-strain relation, hyper-elasticity at large deformations, quasi incompressibility and viscous dissipation under cyclic loading. Furthermore, the temperature dependence of the elastic and the viscoelastic material properties are depicted, as well as the so-called *Gough-Joule effect*. All these phenomena occur at typical tire service temperatures $\Theta \in [-30, 60]$°C, whilst local temperatures may reach up to 120°C in hot spots inside the tire. Below the minimum service temperature, the material stiffness increases, whereas the elasticity decreases. Finally, at the so-called glass transition temperature the material changes from its rubbery to a glassy state and becomes brittle. Above the maximum service temperature aging mechanisms are accelerated, which soften the rubber irreversibly. Phenomena outside the service temperature regime are not in the scope of this work. Damage mechanisms like strain induced softening (*Mullins effect*) as well as wear and residual stretches (viscoplasticity) are also neglected due to the following assumptions. Damage effects occur within the first few revolutions of a virgin tire and do not to advance significantly thereafter. Wear effects evolve on larger time scales and are therefore of minor influence for the current steady state material behavior.

After some general remarks on constitutive material modeling and objectivity of material models, the model for the thermoelastic material behavior is introduced. Then, the applied concept for linear thermo-viscoelasticity at finite strains is summarized, followed by the algorithmic treatment of the coupled thermomechanical problem. The chapter ends with a numerical study illustrating the most important effects of the modeled thermo-viscoelastic material behavior.

3.1 General aspects of constitutive material modeling

Following [Holzapfel, 2000], the *Helmholtz free energy* for thermo-viscoelastic rubber materials is introduced as

$$\psi = \psi \left\{ \boldsymbol{E}, \Theta, \boldsymbol{\alpha}_{\mathrm{v}}^{(i)} \right\}. \tag{3.1}$$

In this thermoelastic expansion of the *generalized Maxwell model* the stored energy nonlinearly depends on the following state variables: the *Green-Lagrange strain* $\boldsymbol{E}$, the temperature Θ, and a set of strain-valued internal variables $\boldsymbol{\alpha}_{\mathrm{v}}^{(i)}$, which depict the elastic deformation of each *Maxwell-element*. Inserting the total time derivative of (3.1)

$$\dot{\psi} = \frac{\partial \psi}{\partial \boldsymbol{E}} : \dot{\boldsymbol{E}} + \frac{\partial \psi}{\partial \Theta} \dot{\Theta} + \sum_i \frac{\partial \psi}{\partial \boldsymbol{\alpha}_{\mathrm{v}}^{(i)}} : \dot{\boldsymbol{\alpha}}_{\mathrm{v}}^{(i)}, \tag{3.2}$$

into the Clausius-Duhem inequaltiy (2.48) and reorganizing the terms yields

$$\left(\boldsymbol{S} - \varrho \frac{\partial \psi}{\partial \boldsymbol{E}} \right) : \dot{\boldsymbol{E}} + \left(\frac{\partial \psi}{\partial \Theta} - s \right) \varrho \dot{\Theta} - \varrho \sum_i \frac{\partial \psi}{\partial \boldsymbol{\alpha}_{\mathrm{v}}^{(i)}} : \dot{\boldsymbol{\alpha}}_{\mathrm{v}}^{(i)} - \frac{1}{\Theta} \boldsymbol{Q} \cdot \mathrm{Grad}\Theta \geq 0. \tag{3.3}$$

In order to ensure the fulfillment of this relation for arbitrary values of $\dot{\boldsymbol{F}}$ and $\dot{\Theta}$, each term in brackets needs to be set to zero separately. Thus, the *second Piola-Kirchhoff stress tensor* is calculated by

$$\boldsymbol{S} = \varrho \frac{\partial \psi}{\partial \boldsymbol{E}} = \frac{\partial \Psi}{\partial \boldsymbol{E}} = 2 \frac{\partial \Psi}{\partial \boldsymbol{C}}, \tag{3.4}$$

where $\Psi = \varrho \psi$ is the strain energy function describing the stored energy per unit mass element. In conjuction with the separation of thermal and mechanical stress power (2.44), the entropy is computed from

$$\varrho s = \frac{\varphi'_{\Theta}}{3 \varphi_{\Theta}} \check{\boldsymbol{S}}_M : \check{\boldsymbol{C}}_M - \frac{\partial \Psi}{\partial \Theta}. \tag{3.5}$$

The viscoelastic material response is represented by a conjugate thermodynamic stress tensor

$$\boldsymbol{A}_{\mathrm{v}}^{(i)} = -\varrho \frac{\partial \psi}{\partial \boldsymbol{\alpha}_{\mathrm{v}}^{(i)}}. \tag{3.6}$$

The fulfillment of the remainder requires a consistent material model describing the heat flux. This is achieved by applying the *Fourier heat conduction law*

$$\boldsymbol{Q} = -k_{\Theta}(\Theta) \boldsymbol{C}^{-1} \cdot \mathrm{Grad}\Theta, \tag{3.7}$$

for heat conduction coefficients $\kappa_{\Theta}(\Theta) \geq 0$. In the present study, the heat conduction coefficient is modeled temperature dependent with the softening parameter ω_k via

$$k_{\Theta}(\Theta) = k_{\Theta 0}(1 - \omega_k(\Theta - \Theta_0)). \tag{3.8}$$

The remainder results in the definition of internal dissipation

$$\mathcal{D}_{\text{int}} = \sum_i \boldsymbol{A}_{\text{v}}^{(i)} : \dot{\boldsymbol{\alpha}}_{\text{v}}^{(i)} \geq 0. \tag{3.9}$$

Inserting the above findings into the heat conduction equation (2.49) and recalling the separation of stress power (2.44) results in the final form of the heat conduction equation

$$\varrho\Theta\dot{s} = -\frac{1}{3}\frac{\varphi_\Theta'}{\varphi_\Theta}\breve{\boldsymbol{S}}_M : \breve{\boldsymbol{C}}_M + \mathcal{D}_{\text{int}} - \frac{1}{\Theta}\boldsymbol{Q}\cdot\text{Grad}\Theta - \text{Div}\boldsymbol{Q} + \varrho r. \tag{3.10}$$

Note that the first term vanishes if the stress power is not separated into its mechanical and thermal parts by (2.44).

In addition to the general statements above, it is useful to introduce some specific preliminaries in the context of rubber modeling: The shear stiffness of rubber materials in general is much smaller than their volumetric stiffness, which is often described as quasi-incompressible material behavior. In order to depict this material behavior, a volumetric-isochoric split of kinematic quantities

$$\boldsymbol{F} = J^{\frac{1}{3}}\bar{\boldsymbol{F}} \text{ and } \boldsymbol{C} = J^{\frac{2}{3}}\bar{\boldsymbol{C}}, \text{ with } J = \det\boldsymbol{F} \tag{3.11}$$

is defined, which allows for a separated treatment of the volumetric response and the much softer isochoric parts. The thermal expansion of the material is depicted by the exponential scalar function suggested in [Lu and Pister, 1975]

$$\varphi_\Theta(\Theta) = \exp\left(\int_{\Theta_0}^{\Theta} 3\alpha_\Theta(\Theta)\,\mathrm{d}\Theta\right) = \exp\left(3\alpha_{\Theta 0}(\Theta-\Theta_0)\right). \tag{3.12}$$

Following [Heimes, 2005; Höfer, 2009], this function is used to compute the thermal deformation gradient $\boldsymbol{F}(\Theta)$ (2.10) and defines the thermomechanical separation of the deformation gradient (2.9). With these definitions, standard material models formulated in the isothermal regime can be evaluated in terms of the effective mechanical quantities

$$J_M = \frac{J(\boldsymbol{F},\Theta)}{\varphi_\Theta(\Theta)},\ \breve{\boldsymbol{C}}_M = \varphi_\Theta(\Theta)^{-\frac{2}{3}}\boldsymbol{C} \text{ and } \breve{\boldsymbol{S}}_M = \varphi_\Theta^{\frac{2}{3}}\boldsymbol{S}. \tag{3.13}$$

Note that the application of (3.11) yields $\breve{\bar{\boldsymbol{C}}}_M = J_M^{-\frac{2}{3}}\breve{\boldsymbol{C}}_M = \bar{\boldsymbol{C}}$. Consequently, the invariants of the isochoric response are equal in both configurations and can be calculated with definition (2.17), where $III_{\bar{C}_M} = III_{\bar{C}} = 1$.

Finally, the general additive structure of the strain energy function for the thermo-viscoelastic constitutive material model is stated as

$$\Psi\left(\breve{\boldsymbol{C}}_M,\Theta,\boldsymbol{\alpha}_{\text{v}}^{(i)}\right) = \Psi^\infty\left(\breve{\boldsymbol{C}}_M,\Theta\right) + \sum_{i=1}^{N}\Upsilon_i\left(\bar{\boldsymbol{C}},\Theta,\bar{\boldsymbol{\alpha}}_{\text{v}}^{(i)}\right). \tag{3.14}$$

The first term Ψ^∞ describes the time-invariant, thermoelastic equilibrium response of the material for $t\to\infty$. Each summand of the second term represents an isochoric, thermo-viscoelastic *Maxwell-element* with an additional strain-valued internal variable $\bar{\boldsymbol{\alpha}}_{\text{v}}^{(i)}$.

3.2 Thermoelastic constitutive material model for tire rubber

3.2.1 Strain energy function

This section describes the thermoelastic material model that represents the equilibrium stress response of tire rubber assuming entropy-elasticity. This model accounts for hyper-elastic material behavior, thermal stiffening, and the Gough Joule effect. The strain energy function for this thermoelastic constitutive material model

$$\Psi^{\infty}\left(\breve{\boldsymbol{C}}_M, \Theta\right) = U^{\infty}\left(J_M, \Theta\right) + W^{\infty}\left(\bar{\boldsymbol{C}}, \Theta\right) + T^{\infty}(\Theta), \tag{3.15}$$

consists of a volumetric penalty function enforcing incompressibility U^{∞}, the isochoric material response W^{∞} and the stored thermal energy T^{∞}.

The volumetric penalty function enforcing incompressibility presented in [Hartmann and Neff, 2003] is applied in order to restrict the effective volumetric deformation

$$U^{\infty}\left(J_M\right) = \frac{\kappa_0}{50}\left(J_M^5 + J_M^{-5} - 2\right), \tag{3.16}$$

where κ_0 is the compression modulus at reference temperature. This penalty function fulfills the physical plausibility conditions

$$U^{\infty}(1) = 0, U^{\infty\prime}(1) = 0, U^{\infty\prime\prime}(J) \geq 0, \lim_{J\to 0} U^{\infty}(J) = \infty, \lim_{J\to\infty} U^{\infty}(J) = \infty$$

and is convex in J. In this contribution, a superior behavior of this model compared to e.g. widely used models such as $U(J) = \frac{\kappa}{1}\left(J^1 - 1\right)$ was discussed.

Alternatively, the material model can be formulated in the reference configuration, as presented in [Suwannachit, 2013]. Here, the volumetric penalty function

$$U(J, \Theta) = \frac{\kappa_0 \Theta}{50\Theta_0}\left(J^5 + J^{-5} - 2\right) - \frac{\varrho e_0}{\Theta_0}(\Theta - \Theta_0), \text{ with } ,\frac{\varrho e_0}{\Theta_0} = 3\alpha_{\Theta 0}\kappa_0\gamma_{\Theta}^{-1}\left(J^{\gamma_\Theta} - 1\right) \tag{3.17}$$

is enhanced by a second term that represents the thermal expansion by a reduction of the volumetric stress response at elevated temperatures. Here, $\alpha_{\Theta 0}$ is the thermal expansion coefficient and γ_Θ is a thermomechanical coupling parameter. This phenomenological term was first introduced in [Chadwick, 1974], and has also been applied in the works of [Holzapfel and Simo, 1996a,b]. Its formulation is based on the idea of an additional potential to cope with the change of entropy induced by thermal expansion. However, this formulation does not ensure a stress-free thermal expansion.

The isochoric thermoelastic material response $W^{\infty}\left(\bar{\boldsymbol{C}}, \Theta\right) = \frac{\Theta}{\Theta_0} W^{\infty}\left(\bar{\boldsymbol{C}}, \Theta_0\right)$ is modeled in terms of well established isothermal formulations. In order to account for the temperature dependence of the elastic properties, their material parameters are linearly scaled

by the temperature. By means of this, the thermomechanical *Neo-Hooke model* takes the form

$$W^{\infty}\left(\bar{\boldsymbol{C}},\Theta\right)=\frac{\Theta}{\Theta_0}\frac{\mu_0}{2}(I_{\bar{C}}-3), \tag{3.18}$$

where μ_0 is the shear modulus at reference temperature. The thermomechanical *Mooney-Rivlin model* reads

$$W^{\infty}(\bar{\boldsymbol{C}},\Theta)=\frac{\Theta}{\Theta_0}\left[c_{10}(I_{\bar{C}}-3)+c_{01}(II_{\bar{C}}-3)\right], \tag{3.19}$$

with its material constants c_{10} and c_{01} at reference temperature.

Analogously, a linear temperature dependence for more sophisticated material models can be introduced, such as the *extended tube model* presented in [Kaliske and Heinrich, 1999]

$$W^{\infty}\left(\bar{\boldsymbol{C}},\Theta\right) \;=\; \frac{\Theta}{\Theta_0}\left(W^{\mathrm{topo}}\left(\bar{\boldsymbol{C}},\Theta_0\right)+W^{\mathrm{chem}}\left(\bar{\boldsymbol{C}},\Theta_0\right)\right). \tag{3.20}$$

This model consists of a topological W^{topo} and a chemical part W^{chem}, which are defined as

$$W^{\mathrm{topo}}\left(\bar{\boldsymbol{C}},\Theta_0\right) \;=\; \frac{2G_e}{\beta^2}\sum_{i=1}^{3}\left(\bar{\lambda}_i^{-\beta}-1\right) \tag{3.21}$$

$$W^{\mathrm{chem}}\left(\bar{\boldsymbol{C}},\Theta_0\right) \;=\; \frac{G_c}{2}\left\{\frac{(1-\delta^2)(I_{\bar{C}}-3)}{1-\delta^2(I_{\bar{C}}-3)}+\log\left[1-\delta^2(I_{\bar{C}}-3)\right]\right\}. \tag{3.22}$$

Here, the shear moduli G_c and G_e result from chemical bonds and topological restraints by finite chain length of rubber molecules. The parameter δ accounts for the restricted stretch of the polymer network chains, and tunes the upturn behavior of the elastic response that occurs when then chains are fully stretched. The fitting parameter $\beta\in[0,1]$ depends on the network structure and is ≈ 1 for well-connected, long polymer chains, see [Kaliske and Heinrich, 1999] for details. Following [Ziefle, 2007], its value is assumed to be 1 in the course of this thesis. The effect of this term above the maximum stretch can be characterized as a penalty function, which has a severe impact on the volumetric expansion being restricted in the same way. The interaction of both terms is observed in section 3.5.

The formulation of the thermal potential presented by [Heimes, 2005] was designed inversely, assuming a linear temperature dependence of the isobaric heat capacity

$$c_p=c_{p0}\left(1-k_{cp}\Theta_0\right)\left(\Theta-\Theta_0\right)=-\frac{1}{\varrho_0}\frac{\partial^2 T}{\partial\Theta\partial\Theta}. \tag{3.23}$$

The integration of this relation results in the thermal part of the potential

$$T^{\infty}(\Theta)=\varrho_0 c_{p0}\left[(1-k_{cp}\Theta_0)(\Theta-\Theta_0-\Theta\log\left(\frac{\Theta}{\Theta_0}\right)-\frac{1}{2}k_{cp}(\Theta-\Theta_0)^2\right]. \tag{3.24}$$

[Höfer, 2009] presented an experimental validation of this potential function.

3.2.2 Calculation of Stress

The general form of the calculation of the *second Piola Kirchhoff stress tensor* for isotropic materials, formulated in terms of invariants, is given in [Holzapfel, 2000] p. 216

$$\boldsymbol{S} = 2\frac{\partial \Psi(\boldsymbol{C})}{\partial \boldsymbol{C}} = 2\left[\left(\frac{\partial \Psi}{\partial I} + I\frac{\partial \Psi}{\partial II}\right)\boldsymbol{I} - \frac{\partial \Psi}{\partial II}\boldsymbol{C} + III\frac{\partial \Psi}{\partial III}\boldsymbol{C}^{-1}\right], \tag{3.25}$$

where $\boldsymbol{I}$ is the second order unit tensor. Due to the additive definition of the strain energy density (3.15), the stress response can be calculated component-wise by

$$\boldsymbol{S} = 2\frac{\partial \Psi\left(\breve{\boldsymbol{C}}_M, \Theta, \alpha_i\right)}{\partial \boldsymbol{C}} = 2\frac{\partial U^{\infty}(J_M, \Theta)}{\partial \boldsymbol{C}} + 2\frac{\partial W^{\infty}\left(\bar{\boldsymbol{C}}, \Theta\right)}{\partial \boldsymbol{C}}. \tag{3.26}$$

Using the chain rule, the volumetric contribution of (3.16) yields

$$\frac{\partial U^{\infty}(J_M)}{\partial \boldsymbol{C}} = \frac{\kappa_0}{20}\left(J_M^5 - J_M^{-5}\right)\boldsymbol{C}^{-1}. \tag{3.27}$$

Note that the implementation of this model only requires an exchange of the total volumetric deformation J by the effective mechanical measure J_M. If the model presented in [Suwannachit, 2013] (3.17) is applied, the volumetric response yields

$$\frac{\partial U^{\infty}(J, \Theta)}{\partial \boldsymbol{C}} = \left(\frac{\kappa_0 \Theta}{20\Theta_0}\left(J^5 - J^{-5}\right) - 3\alpha_{\Theta 0}\kappa_0 J^{\gamma\Theta}(\Theta - \Theta_0)\right)\boldsymbol{C}^{-1}. \tag{3.28}$$

The isochoric part of the *second Piola-Kirchhoff stress tensor* in case of the *Neo-Hooke model* (3.18) is calculated by

$$\frac{\partial W^{\infty}(\bar{\boldsymbol{C}}, \Theta)}{\partial \boldsymbol{C}} = \frac{\Theta}{\Theta_0}\frac{\mu}{2}J^{-\frac{2}{3}}\left(\boldsymbol{I} - \frac{1}{3}I_C\boldsymbol{C}^{-1}\right), \tag{3.29}$$

and the stress response of the *Mooney-Rivlin model* (3.19) is computed via

$$\frac{\partial W^{\infty}(\bar{\boldsymbol{C}}, \Theta)}{\partial \boldsymbol{C}} = \frac{\Theta}{\Theta_0}J^{-\frac{2}{3}}\left((c_{10} + c_{01}I_C)\boldsymbol{I} - c_{01}\bar{\boldsymbol{C}} - \left(\frac{c_{10}}{3}I_C + \frac{2c_{01}}{3}II_C\right)\boldsymbol{C}^{-1}\right). \tag{3.30}$$

Finally, the derivation of the *extended tube model* (3.20) yields

$$\begin{aligned}\frac{\partial W^{\infty}\left(\bar{\boldsymbol{C}}, \Theta\right)}{\partial \boldsymbol{C}} &= G_c J^{-\frac{2}{3}}\left(\frac{1-\delta^2}{\left(1-\delta^2\left(I_{\bar{C}}-3\right)\right)^2} - \frac{\delta^2}{1-\delta^2\left(I_{\bar{C}}-3\right)}\right)\left(\boldsymbol{I} - \frac{1}{3}I_C\boldsymbol{C}^{-1}\right) \\ &+ G_e\sum_{i=1}^{3}\left(\frac{J}{\lambda_i^2}\left(\frac{1}{3}\left(\lambda_1^{-1} + \lambda_2^{-1} + \lambda_3^{-1}\right) - \lambda_i^{-1}\right)\right)\boldsymbol{E}_i^{\bar{C}} \otimes \boldsymbol{E}_i^{\bar{C}}.\end{aligned} \tag{3.31}$$

Here, $\boldsymbol{E}_i^{\bar{C}}$ denotes the eigenvectors of $\bar{\boldsymbol{C}}$ and the assumption $\beta = 1$ has already been inserted in order to shorten the notation. See Appendix A for further details on these derivations.

3.2.3 Calculation of entropy

Following [Höfer, 2009], the calculation of entropy (3.5) is performed by

$$\varrho_0 s = \frac{3\alpha_{\Theta 0}\kappa_0}{10}(J_M^5 - J_M^{-5}) - \frac{\partial U^\infty(J,\Theta)}{\partial\Theta} - \frac{\partial W^\infty\left(\bar{\boldsymbol{C}},\Theta\right)}{\partial\Theta} - \frac{\partial T^\infty(\Theta)}{\partial\Theta}, \tag{3.32}$$

where the first term represents the mechanical energy stored in the thermal expansion $\frac{\varphi'_\Theta}{3\varphi_\Theta}\breve{\boldsymbol{S}}_M : \breve{\boldsymbol{C}}_M$. The derivative of the volumetric penalty function in terms of purely mechanical deformation (3.16) with respect to temperature yields $\frac{\partial U^\infty(J_M)}{\partial\Theta} = 0$. For the unseparated formulation (3.17), the first term vanishes due to $\varphi_\Theta = 0$, and the derivative with respect to temperature yields

$$\frac{\partial U^\infty(J,\Theta)}{\partial\Theta} = \frac{\kappa_0}{50\Theta_0}\left(J^5 + J^{-5} - 2\right) - \frac{3\alpha_{\Theta 0}\kappa_0\gamma^{-1}}{\Theta_0}\left(J^\gamma - 1\right). \tag{3.33}$$

Due to the linear scaling with temperature, the derivative of the deviatoric part simply is $\frac{\partial W^\infty(\bar{\boldsymbol{C}},\Theta)}{\partial\Theta} = \frac{1}{\Theta_0}W^\infty\left(\bar{\boldsymbol{C}},\Theta_0\right)$. And finally, the derivative of thermal potential with respect to temperature yields

$$\frac{\partial T^\infty(\Theta)}{\Theta} = \varrho_0 c_{p0}\left[(1 - k_{cp}\Theta_0)\left(-\log\left(\frac{\Theta}{\Theta_0}\right)\right) - k_{cp}\left(\Theta - \Theta_0\right)\right]. \tag{3.34}$$

3.3 Linear thermo-viscoelasticity at finite strains

Following [Suwannachit, 2013], the time-dependent thermo-viscoelastic material response is modeled by a *generalized Maxwell-model* in the regime of finite deformations. For a generalized overview, we assume a multiplicative split of the initial deformation gradient (2.4)

$$\boldsymbol{F}_0 = \bar{\boldsymbol{F}} \cdot \boldsymbol{F}_{\mathrm{ref}}, \tag{3.35}$$

into a relative isochoric motion $\bar{\boldsymbol{F}}$ that describes the deformation of the *Maxwell-elements* and an arbitrary dilational reference motion $\boldsymbol{F}_{\mathrm{ref}}$. For each *Maxwell-element*, an intermediate configuration is introduced by multiplicative separation of the isochoric deformation gradient

$$\bar{\boldsymbol{F}} = \bar{\boldsymbol{F}}_{\mathrm{el}}^{(i)} \cdot \bar{\boldsymbol{F}}_{\mathrm{v}}^{(i)} \tag{3.36}$$

into an elastic $\bar{\boldsymbol{F}}_{\mathrm{el}}^{(i)}$ and a viscoelastic part $\bar{\boldsymbol{F}}_{\mathrm{v}}^{(i)}$. This separation yields an additive decomposition of deviatoric *Green-Lagrange strain* and its rate

$$\begin{aligned}
\bar{\boldsymbol{E}} &= \frac{1}{2}\left(\left(\bar{\boldsymbol{F}}_{\mathrm{v}}^{(i)}\right)^{\mathrm{T}} \cdot \bar{\boldsymbol{F}}_{\mathrm{v}}^{(i)} - \boldsymbol{1}\right) + \frac{1}{2}\left(\bar{\boldsymbol{F}}^{\mathrm{T}} \cdot \bar{\boldsymbol{F}} - \left(\bar{\boldsymbol{F}}_{\mathrm{v}}^{(i)}\right)^{\mathrm{T}} \cdot \bar{\boldsymbol{F}}_{\mathrm{v}}^{(i)}\right) \\
&= \bar{\boldsymbol{\alpha}}_{\mathrm{v}}^{(i)} + \bar{\boldsymbol{H}}_{\mathrm{el}}^{(i)} \qquad (3.37) \\
\dot{\bar{\boldsymbol{E}}} &= \dot{\bar{\boldsymbol{\alpha}}}_{\mathrm{v}}^{(i)} + \dot{\bar{\boldsymbol{H}}}_{\mathrm{el}}^{(i)}, \qquad (3.38)
\end{aligned}$$

where $\bar{\boldsymbol{\alpha}}_{\mathrm{v}}^{(i)}$ is an internal variable and $\bar{\boldsymbol{H}}_{\mathrm{el}}^{(i)}$ is an elastic algorithmic strain variable, see [Suwannachit, 2013]. With these kinematic definitions, the energy stored in the spring element of the i-th *Maxwell-element* is modeled by

$$\Upsilon^{(i)}\left(\bar{\boldsymbol{C}}, \Theta, \bar{\boldsymbol{\alpha}}_{\mathrm{v}}^{(i)}\right) = \mu_{\mathrm{v}}^{(i)}(\Theta)\left(\bar{\boldsymbol{E}} - \bar{\boldsymbol{\alpha}}_{\mathrm{v}}^{(i)}\right) : \left(\bar{\boldsymbol{E}} - \bar{\boldsymbol{\alpha}}_{\mathrm{v}}^{(i)}\right), \tag{3.39}$$

where $\mu_{\mathrm{v}}^{(i)}(\Theta)$ is the temperature dependent shear modulus. With this potential, the thermodynamic stress conjugate to the internal variable (3.6) yields

$$-\frac{\partial \Upsilon^{(i)}\left(\bar{\boldsymbol{C}}, \Theta, \bar{\boldsymbol{\alpha}}_{\mathrm{v}}^{(i)}\right)}{\partial \bar{\boldsymbol{\alpha}}_{\mathrm{v}}^{(i)}} = \bar{\boldsymbol{A}}_{\mathrm{v}}^{(i)} = \eta_{\mathrm{v}}^{(i)}(\Theta)\dot{\bar{\boldsymbol{\alpha}}}_{\mathrm{v}}^{(i)}. \tag{3.40}$$

Following [Johlitz et al., 2010], the shear modulus and the viscosity $\eta_{\mathrm{v}}^{(i)}(\Theta)$ at the current temperature are calculated by

$$\begin{aligned} \mu_{\mathrm{v}}^{(i)}(\Theta) = a_{\mathrm{v}}^{T}(\Theta)\mu_{\mathrm{v}}^{(i)}(\Theta_0) \text{ and } \eta_{\mathrm{v}}^{(i)}(\Theta) = a_{\mathrm{v}}^{T}(\Theta)\eta_{\mathrm{v}}^{(i)}(\Theta_0), \\ \text{with } a_{\mathrm{v}}^{T}(\Theta) = \exp\left[\xi_{\mathrm{v}}^{(i)}\left(1 - \frac{\Theta}{\Theta_0}\right)\right], \end{aligned} \tag{3.41}$$

where $\xi_{\mathrm{v}}^{(i)}$ is a relaxation parameter, which causes a decrease of dissipation at elevated temperatures for $\xi_{\mathrm{v}}^{(i)} > 0$ assuming less friction loss by the relative motion of polymer chains. Due the same scaling of both material parameters, the relaxation time

$$\tau_{\mathrm{v}}^{(i)} = \frac{\eta_{\mathrm{v}}^{(i)}(\Theta_0)}{2\mu_{\mathrm{v}}^{(i)}(\Theta_0)} \tag{3.42}$$

is temperature invariant.

In order to evaluate the stress response of the *Maxwell-element*, the internal variable $\bar{\boldsymbol{\alpha}}_{\mathrm{v}}^{(i)}$ that describes the relaxation needs to be calculated. In analogy to the equilibrium of the stress within the spring and the dashpot in the uniaxial case it can be postulated that

$$\bar{\boldsymbol{A}}_{\mathrm{v}}^{(i)} = \eta_{\mathrm{v}}^{(i)}(\Theta)\dot{\bar{\boldsymbol{\alpha}}}_{\mathrm{v}}^{(i)} = 2\mu_{\mathrm{v}}^{(i)}(\Theta)(\bar{\boldsymbol{E}} - \bar{\boldsymbol{\alpha}}_{\mathrm{v}}^{(i)}) = 2\mu_{\mathrm{v}}^{(i)}(\Theta)\bar{\boldsymbol{H}}_{\mathrm{el}}^{(i)}, \tag{3.43}$$

which can be used to formulate an evolution equation

$$\dot{\bar{\boldsymbol{\alpha}}}_{\mathrm{v}}^{(i)} = \frac{1}{\tau_{\mathrm{v}}^{(i)}}\bar{\boldsymbol{H}}_{\mathrm{el}}^{(i)} = \frac{1}{\tau_{\mathrm{v}}^{(i)}}(\bar{\boldsymbol{E}} - \bar{\boldsymbol{\alpha}}_{\mathrm{v}}^{(i)}). \tag{3.44}$$

Due to the temperature invariance of the relaxation time, this evolution equation can be solved analytically by convolution

$$\bar{\boldsymbol{H}}_{\mathrm{el}}^{(i)}(t) = \int_{t_0}^{t} \exp\left(-\frac{t-s}{\tau_{\mathrm{v}}^{(i)}}\right)\dot{\bar{\boldsymbol{E}}}(s)\mathrm{d}s \text{ assuming } \bar{\boldsymbol{H}}_{\mathrm{el}}^{(i)}(0) = 0, \tag{3.45}$$

which significantly reduces the computational effort. This integral can be transferred into an update formula

$$\bar{\boldsymbol{H}}_{\mathrm{el}}^{(i)}(t_{n+1}) = \exp\left(-\frac{\Delta t}{\tau_{\mathrm{v}}^{(i)}}\right)\bar{\boldsymbol{H}}_{\mathrm{el}}^{(i)}(t_n) + \exp\left(-\frac{\Delta t}{2\tau^{(i)}}\right)\Delta\bar{\boldsymbol{E}}, \tag{3.46}$$

in time-discrete solution schemes with a time step size Δt.

Finally, the deviatoric overstress response of the rate dependent *Maxwell-elements* in terms of the *second Piola-Kirchhoff stress tensor* yields

$$\bar{\boldsymbol{S}}_{\mathrm{v}}^{(i)}(t_{n+1}) = \frac{\partial\Upsilon\left(\bar{\boldsymbol{C}},\Theta,\bar{\boldsymbol{\alpha}}_{\mathrm{v}}^{(i)}\right)}{\partial\boldsymbol{C}} = 2\mu_{\mathrm{v}}^{(i)}(\Theta)J^{-\frac{2}{3}}\mathrm{DEV}\bar{\boldsymbol{H}}_{\mathrm{el}}^{(i)}(t_{n+1}) = J^{-\frac{2}{3}}\mathrm{DEV}\bar{\boldsymbol{A}}_{\mathrm{v}}^{(i)}(t_{n+1}), \tag{3.47}$$

and the dissipation in each element is calculated by

$$\mathcal{D}_{\mathrm{int}}^{(i)}(t_{n+1}) = 2\mu_{\mathrm{v}}^{(i)}(\Theta)\bar{\boldsymbol{H}}_{\mathrm{el}}^{(i)}(t_{n+1}) : \dot{\bar{\boldsymbol{\alpha}}}_{\mathrm{v}}^{(i)}(t_{n+1}) = \frac{1}{\eta_{\mathrm{v}}^{(i)}(\Theta)}\bar{\boldsymbol{A}}_{\mathrm{v}}^{(i)}(t_{n+1}) : \bar{\boldsymbol{A}}_{\mathrm{v}}^{(i)}(t_{n+1}). \tag{3.48}$$

The thermal derivative of (3.39) results in the entropy in each *Maxwell-element*

$$\varrho_0 s_{\mathrm{v}}^{(i)}(t_{n+1}) = -\frac{\partial\Upsilon^{(i)}\left(\bar{\boldsymbol{C}},\Theta,\bar{\boldsymbol{\alpha}}_{\mathrm{v}}^{(i)}\right)}{\partial\Theta} = \frac{\xi_{\mathrm{v}}^{(i)}}{\Theta_0}\mu_{\mathrm{v}}^{(i)}(\Theta)\bar{\boldsymbol{H}}_{\mathrm{el}}^{(i)}(t_{n+1}) : \bar{\boldsymbol{H}}_{\mathrm{el}}^{(i)}(t_{n+1}), \tag{3.49}$$

which adds to the entropy of the thermoelastic model (3.32).

3.4 Algorithmic treatment of the coupled thermomechanical problem

The calculation of the thermo-viscoelastic response of tire rubber compounds by means of finite element methods requires the solution of both the balance of linear momentum (2.40) and the heat conduction equation (balance of energy) (3.10), which results in a coupled thermomechanical problem. The weak forms of the mathematical problem are stated as follows:

$$\mathcal{G}_{\boldsymbol{u}}(\boldsymbol{u},\delta\boldsymbol{u}) = \int_{\mathcal{B}}\left(-\varrho\dot{\boldsymbol{v}}\cdot\delta\boldsymbol{u} + \boldsymbol{S} : \delta\boldsymbol{E} + \varrho\boldsymbol{b}\cdot\delta\boldsymbol{u}\right)\mathrm{d}V + \int_{\partial_t\mathcal{B}}\boldsymbol{T}\cdot\delta\boldsymbol{u}\,\mathrm{d}A, \tag{3.50}$$

$$\mathcal{G}_{\Theta}(\Theta,\delta\Theta) = \int_{\mathcal{B}}\delta\Theta\left(\varrho_0\dot{s}\Theta - \mathcal{D}_{\mathrm{int}} - \varrho r\right) + \mathrm{Grad}\delta\Theta\cdot\boldsymbol{Q}\,\mathrm{d}V + \int_{\partial_q\mathcal{B}}Q_N\delta\Theta\,\mathrm{d}A. \tag{3.51}$$

The sought solution $\mathcal{G}_{\boldsymbol{u}}(\boldsymbol{u},\delta\boldsymbol{u}) = \mathcal{G}_{\Theta}(\Theta,\delta\Theta) \stackrel{!}{=} 0$ fulfills

$$\boldsymbol{u}(\boldsymbol{X},t) = \bar{\boldsymbol{u}}(\boldsymbol{X},t)\,\forall\boldsymbol{X}\in\partial_{\boldsymbol{u}}\mathcal{B} \quad\wedge\quad \boldsymbol{P}(\boldsymbol{X},t)\cdot\boldsymbol{N}(\boldsymbol{X}) = \boldsymbol{T}(\boldsymbol{X},t)\,\forall\boldsymbol{X}\in\partial_{\boldsymbol{t}}\mathcal{B} \tag{3.52}$$

$$\Theta(\boldsymbol{X},t) = \bar{\Theta}(\boldsymbol{X},t)\,\forall\boldsymbol{X}\in\partial_{\Theta}\mathcal{B} \quad\wedge\quad \boldsymbol{Q}(\boldsymbol{X},t)\cdot\boldsymbol{N}(\boldsymbol{X}) = Q_N(\boldsymbol{X},t)\,\forall\boldsymbol{X}\in\partial_q\mathcal{B}, \tag{3.53}$$

where $\bar{\boldsymbol{u}}, \bar{\Theta}$ are the *Dirichlet boundary conditions* and $\boldsymbol{T}, Q_N$ are the *von Neumann boundary conditions*. These are applied along the mechanical $\partial\mathcal{B} = \partial_{\boldsymbol{u}}\mathcal{B} \cup \partial_{\boldsymbol{t}}\mathcal{B} \wedge \partial_{\boldsymbol{u}}\mathcal{B} \cap \partial_{\boldsymbol{t}}\mathcal{B} = \emptyset$ and the thermal $\partial\mathcal{B} = \partial_{\Theta}\mathcal{B} \cup \partial_{q}\mathcal{B} \wedge \partial_{\Theta}\mathcal{B} \cap \partial_{q}\mathcal{B} = \emptyset$ boundary separation. In this statement, the following relations have been applied: $\boldsymbol{P}(\boldsymbol{X}, t) = \boldsymbol{F}(\boldsymbol{X}, t) \cdot \boldsymbol{S}(\boldsymbol{X}, t)$ and $\boldsymbol{N}(X) = \text{const.}$ in the reference configuration. Furthermore, the solution requires the specification of an initial temperature field, which is assumed to be homogeneous in this thesis $\Theta(\boldsymbol{X}, t_0) = \Theta_0$. The test functions $\delta\boldsymbol{u}$ and $\delta\Theta$ are arbitrary, but need to fulfill

$$\delta\boldsymbol{u}(\boldsymbol{X}) = 0 \,\forall \boldsymbol{X} \in \partial_{\boldsymbol{u}}\mathcal{B} \text{ and } \delta\Theta(\boldsymbol{X}) = 0 \,\forall \boldsymbol{X} \in \partial_{\Theta}\mathcal{B}. \tag{3.54}$$

For the time-discrete solution of this coupled initial boundary value problem the isentropic operator spit scheme by [Armero and Simo, 1992] has been applied in [Suwannachit and Nackenhorst, 2013]. With this staggered strategy, the problem is solved for each time slab in two subsequent solution phases:

1. Mechanical phase: solve (3.50), for $\Delta s \overset{!}{=} 0$ to obtain $\boldsymbol{u}_{n+1}$
2. Thermal phase: solve (3.51), for $\Delta\boldsymbol{u} \overset{!}{=} 0$ to obtain Θ_{n+1} and s_{n+1}.

This results in an unconditionally stable time-integration algorithm, rather than using the isothermal operator split by [Argyris et al., 1981]. However, this advantage inherits the necessity to calculate an intermediate isentropic temperature $\tilde{\Theta}_{n+1}$ at each integration point. This can be realized in a local iteration scheme, solving

$$\tilde{\Theta}^{k+1}_{n+1} = \tilde{\Theta}^{k}_{n+1} + \Delta\tilde{\Theta} \;\text{ with }\; \Delta\tilde{\Theta} = -\frac{s\left(\boldsymbol{u}_{n+1}, \tilde{\Theta}^{k}_{n+1}\right) - s_n}{\frac{\partial}{\partial\Theta}\left[s\left(\boldsymbol{u}_{n+1}, \tilde{\Theta}^{k}_{n+1}\right)\right]} \text{ and } \tilde{\Theta}^{0}_{n+1} = \Theta_n, \tag{3.55}$$

until the convergence criterion $\Delta\tilde{\Theta} < tol$ is fulfilled. This iteration converges after only a few steps, but still increases numerical costs. Both staggered approaches yield smaller equation systems than monolithic schemes, which are symmetric in case of conservative problems. Monolithic schemes a priori require the solution of large and non-symmetric equation systems. Nonetheless, monolithic systems can be more efficient in case of strong thermomechanical coupling and large time steps, see [Zinatbakhsh et al., 2010].

Following Suwannachit [2013], the material time derivative of the internal entropy in (3.51) is redefined per unit volume and calculated by introducing an Euler backward time stepping scheme

$$\varrho_0 \dot{s} = \varrho_0 \frac{s\left(\boldsymbol{u}_{n+1}, \Theta_{n+1}\right) - s_n}{\Delta t}, \tag{3.56}$$

where s_n is known from the previous step.

Both the mechanical and the thermal phase require the solution of a nonlinear problem in each time step, which is realized with the *Newton-Raphson method*, see e.g. [Wriggers, 2008]. Here, the basic idea is to represent the solution of a functional $\mathcal{F}(\boldsymbol{s})$ at the state $\boldsymbol{s}_{n+1}$ by a Taylor series expansion

$$\mathcal{F}(\boldsymbol{s}_{n+1}) = \left.\frac{\mathrm{d}\mathcal{F}}{\mathrm{d}s}\right|_{\boldsymbol{s}=\boldsymbol{s}_n} \Delta\boldsymbol{s} + \mathcal{F}(\boldsymbol{s}_n), \tag{3.57}$$

where the gradient matrix $\frac{\mathrm{d}\mathcal{F}}{\mathrm{d}s}$ is often referred to as stiffness matrix in the context of engineering finite element methods. This problem can then be solved iteratively, starting at $\boldsymbol{s}_{n+1}^0 = \boldsymbol{s}_n^0$

$$\left.\frac{\mathrm{d}\mathcal{F}}{\mathrm{d}s}\right|_{\boldsymbol{s}=\boldsymbol{s}_n^k} \Delta\boldsymbol{s} = \mathcal{F}\left(\boldsymbol{s}_{n+1}^k\right) - \mathcal{F}(\boldsymbol{s}_n) \tag{3.58}$$

$$\text{and } \boldsymbol{s}_{n+1}^{k+1} = \boldsymbol{s}_{n+1}^k + \Delta\boldsymbol{s}, \tag{3.59}$$

until a desired convergence criterion is reached, such as for the norm of the incremental state change $\|\Delta\boldsymbol{s}\| \leq tol$ or the residual norm $\left\|\mathcal{F}\left(\boldsymbol{s}_{n+1}^k\right) - \mathcal{F}\left(\boldsymbol{s}_n\right)\right\| \leq tol$.

In order to solve the continuos problem for arbitrarily shaped bodies, an iso-parametric finite element discretization is applied, which represents both spatial points of the body as well as the solution fields by a finite number of so-called nodes. In between these points, the geometry and the solution are interpolated with nodal shape functions. Each of these shape functions is defined only on its nodal support. Here, the most common technique is to formulate these shape functions as *Lagrangian polynomials* in discrete simple-shaped integration domains (finite elements), such as triangles, quadriliterals, tetrahedrons, and hexahedrons. As a consequence of this formulation, shape functions are C^0-continuous across the boundaries of these elements.

Note that the total differential of the *second Piola-Kirchhoff stress tensor* takes the form

$$\mathrm{d}\boldsymbol{S} = 2\frac{\partial \boldsymbol{S}}{\partial \boldsymbol{C}} : \frac{1}{2}\mathrm{d}\boldsymbol{C} + \frac{\partial \boldsymbol{S}}{\partial \Theta} : \mathrm{d}\Theta, \tag{3.60}$$

due to temperature dependence of the material, which can be reformulated as

$$\mathrm{d}\boldsymbol{S} = 2\frac{\partial \boldsymbol{S}}{\partial \boldsymbol{C}} : \frac{1}{2}\mathrm{d}\boldsymbol{C} + \frac{\partial \boldsymbol{S}}{\partial \Theta} : \left(-2\frac{\partial s}{\partial \boldsymbol{C}} : \frac{1}{2}\mathrm{d}\boldsymbol{C}\right)\left(\frac{\partial s}{\partial \Theta}\right)^{-1}, \tag{3.61}$$

assuming constant entropy $\mathrm{d}s = 0$. This definition results in a consistent isentropic tangent operator $\mathrm{K}_{\boldsymbol{u}}\left(\boldsymbol{u}, \tilde{\Theta}_{n+1}^{k+1}\right)$, see [Suwannachit, 2013].

3.5 Numerical study of the material behavior

In this section, a short overview of the thermo-viscoelastic material behavior is given by numerical experiments confirming its capability to represent the desired material phenomena. For further details on the implementation of this constitutive material model and on the modeling of rubber materials in continuum thermomechanics, the reader is referred to the theses of [Heimes, 2005; Höfer, 2009; Suwannachit, 2013] and the textbook by [Holzapfel, 2000].

3.5.1 Thermoelastic response and Gough-Joule effect

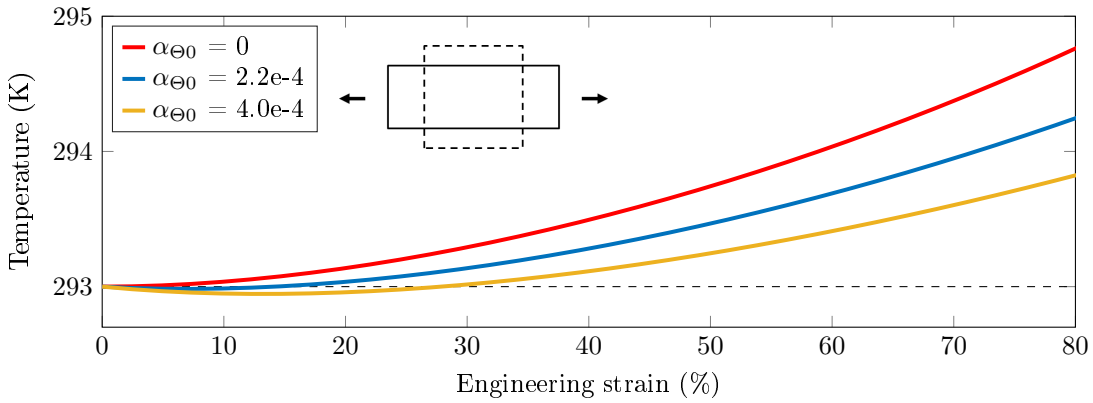

Figure 3.1: Temperature evolution of a thermoelastic rubber strip in a tension test at adiabatic conditions, representing the *Gough-Joule effect*.

In this study, the thermoelastic response of a rubber strip in a quasi-static, uniaxial tensile test at adiabatic conditions is calculated by using the presented finite element framework, in which the material behavior is depicted with the *extended tube model* (3.20). Note that an equivalent shear modulus can be calculated via $\mu = G_e + G_c$ in order to compare the material behavior with the *Neo-Hooke model*. The material parameters (see Table 3.1) used in this study are taken from [Suwannachit, 2013] and [Höfer, 2009]. The calculated system as well as the resulting temperature over stretch are illustrated in Figure 3.1.

The temperature evolution reveals that a slight initial temperature decrease is followed by a continuous temperature increase as the stretch evolves. This behavior matches the experimental observations presented in [Chadwick, 1974], and is closely related to the so-called thermoelastic inversion. As the rubber material is assumed to be entropy elastic and as the test conditions are adiabatic, the internal energy is not altered by deformation. For this reason, the decrease of mechanical entropy resulting from the applied stretch is

Elastic properties		**Viscoelastic properties**	
Chemical shear modulus	$G_c = 3.0\ \mathrm{N/(mm^2)}$	Shear modulus	$\mu_{\mathrm{v}}^1 = 1\ \mathrm{N/(mm^2)}$
Topological shear modulus	$G_e = 1.3\ \mathrm{N/(mm^2)}$	Viscosity	$\eta_{\mathrm{v}}^1 = 0.02\ \mathrm{Ns/(mm^2)}$
Stretch restriction	$\delta = 0.3$	Relaxation time	$\tau_{\mathrm{v}}^1 = 0.01\ \mathrm{s}$
Poisson's ratio	$\nu = 0.49$	Thermal softening	$\xi_{\mathrm{v}}^1 = 10$
Thermal behavior			
Reference temperature	$\Theta_0 = 293\ \mathrm{K}$	Heat capacity	$\varrho_0 c_{p0} = 1.7385\ \mathrm{N/(mm^2\,K)}$,
Thermal expansion	$\alpha_{\Theta 0} = 2.22 \cdot 10^{-4}\ 1/\mathrm{K}$		$k_{cp} = 0.0024\ \mathrm{J/(kg\,K^2)}$
Density	$\varrho_0 = 800\ \mathrm{kg/m^3}$	Thermal conductivity	$k_{\Theta 0} = 0.2595 \cdot 10^{-4}\ 1/\mathrm{K}$,
			$\omega_k = 0.004\ 1/\mathrm{K}$

Table 3.1: Material parameters for the thermo-viscoelastic *extended tube model*.

compensated by an increase in thermal entropy, which is observed as a temperature rise in the specimen. Consequently, this effect is more strongly pronounced with an increasing thermal expansion coefficient $\alpha_{\Theta 0}$, see Figure 3.1.

In this context, [Suwannachit, 2013] simulated the well known demonstration experiment for the *Gough-Joule effect* with this material model. In this experiment, a rubber strip is loaded with a weight and then heated in order to raise its internal energy. This causes the rubber strip to shorten, or in other words, the material stiffness to increase.

In Figure 3.2, this temperature dependence of the thermoelastic material behavior under uniaxial loading is illustrated at typical service temperatures for both the *Neo-Hooke model* (3.18) and the *extended tube model* (3.20). Within the so-called entropy-elastic temperature range, the stiffness of rubber materials increases linearly with increasing temperature. This behavior can be observed for both material models and agrees with the experimental results presented in [Höfer, 2009]. Note that the *Neo-Hooke model* does not reproduce the characteristic upturn of the stress response that results from the full extension of the polymer chains in the rubber material.

In contrast, the *extended tube model* clearly shows this behavior, which results from its topological part (3.21). This representation of the upturn can be understood as penalty restriction, which comes at the cost of a high volumetric expansion at large strains, see Figure 3.3. Here, a volumetric penalty function is not sufficient in order to represent the quasi incompressible material behavior in the domain above 100% strain. As most filled technical rubber materials fail before such high strains are reached, this theoretical limitation is not of practical importance for the further simulations in this thesis.

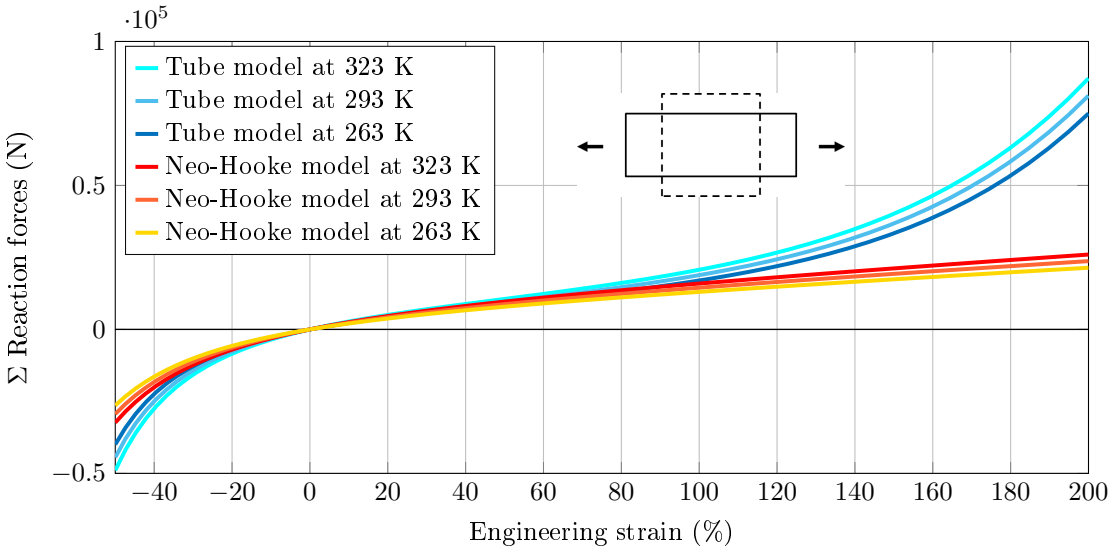

Figure 3.2: Temperature dependence of the elastic material behavior under uniaxial loading.

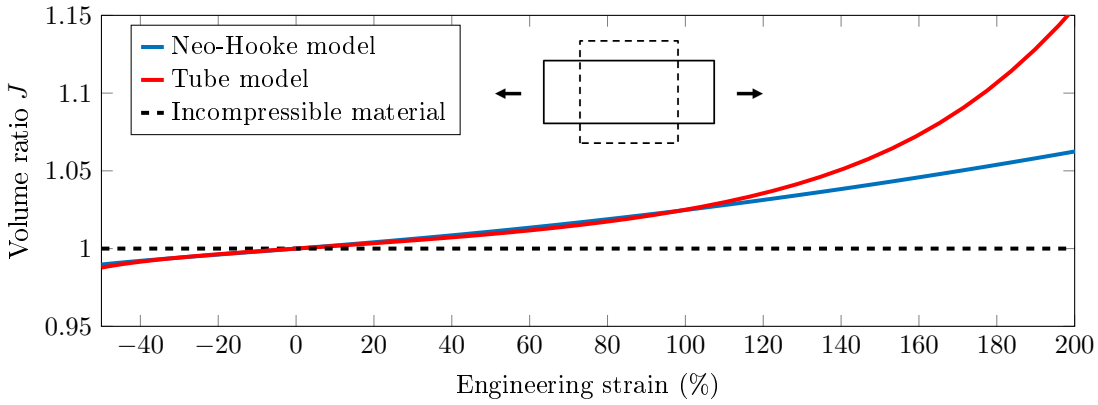

Figure 3.3: Evolution of the volume ratio J over stretch λ.

3.5.2 Thermo-viscoelastic behavior under cyclic loading

In order to demonstrate the stationary thermo-viscoelastic behavior of the material model, 5000 cycles of a shear test were calculated. In this test, a cubic specimen with an edge length of 50 mm is sheared by a sinusoidal excitation with an amplitude of 25 mm at a frequency of 100 Hz under adiabatic conditions. Due to the delayed relaxation of the material, the stress response in the first cycle is much larger along the loading path than along the unloading path, see Figure 3.4 (a). The area in-between the two curves serves as a measure for the dissipated mechanical energy in the load cycle, the so-called hysteresis. This dissipation acts as a heat source causing an increase in temperature, see Figure 3.4 (b) for the temperature evolution in the specimen. In the first cycles the temperature

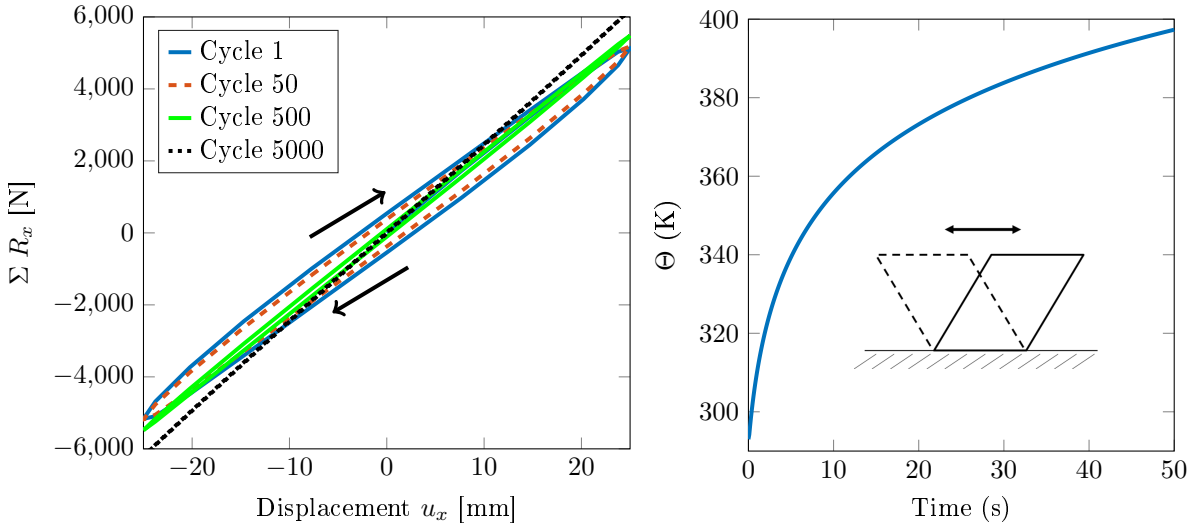

(a) Hysteresis

(b) Temperature evolution

Figure 3.4: Thermo-viscoelastic material response of a rubber strip in a cyclic deformation test at adiabatic conditions (a) stress response and (b) evolution of the average temperature in the specimen.

increases quickly, then the slope decreases until a steady state is reached. This steady state point is characterized by the equilibrium of the internal mechanical dissipation and the thermal dissipation over the boundaries.

The increase in service temperature goes along with a reduction of the viscoelastic material response, resulting in a smaller hysteresis in the load cycle, see Figure 3.4 (a). Due to this fact, hardly any hysteresis is observed for the 500th and for the last cycle, as the thermoelastic response becomes dominant above ≈ 360 K. The physical reason for this behavior lies in the source of the internal mechanical dissipation itself, which is the relative sliding of the polymer chains making up the polymer network of the rubber. At elevated temperatures, the molecules in these chains move faster due to higher entropy, which eases their relative sliding and consequently results in less mechanical dissipation. This behavior is modeled by the thermal softening parameter introduced in (3.41).

4 Thermomechanical contact

In tire mechanics the performance is strongly influenced by the contact interaction of the tire with the road surface. Due the severe temperature dependence of rubber compounds, tire-road interaction is a thermomechanical contact problem. The solution of coupled thermomechanical contact problems requires the enhancement of the mechanical optimization problem (3.50) with a geometrical non-penetration constraint of contacting surfaces. This restriction allows for the calculation of contact tractions, but changes the mathematical character of the problem into a variational inequality. Furthermore, the heat conduction in the resulting contact interface extends the thermal problem (3.51). A detailed overview on computational contact mechanics and the treatment of thermomechanical contact problems is given in the textbooks by [Laursen, 2003; Wriggers, 2006; Yastrebov, 2013].

In order to achieve the main goal of this thesis in developing a constitutive contact model representing mesoscale tread-road interaction, this contact behavior needs to be characterized first. The solution of this rough surface contact problem requires a robust contact constraint enforcement strategy. On the macroscale the contact constraints allow for the computation of the tire's tractive rolling contact behavior (pressure distribution in the footprint and lateral contact tractions) and the calculation of rolling resistance.

In this chapter, the necessary theory for the formulation and solution of thermomechanical contact problems is summarized. This overview starts with kinematic quantities to detect contact and to describe the relative motion of material points in the contact interface in between two bodies. Then, the balance of energy and the *Clausius-Duhem inequality* are formulated for the contact interface. The chapter ends with the description of contact constraint enforcement strategies. Due the introduction of *Arbitrary Lagrangian Eulerian kinematics* to describe the tire's rolling motion, material particles are not fixed to the mesh and therefore contact constraint enforcement strategies for frictional contact that were developed in *Lagrangian kinematics* cannot be applied to compute the tire's tractive response. This problem has been solved by the approach presented by [Ziefle, 2007], which is applied in combination with the phenomenological friction law describing rubber friction by [Huemer et al., 2001a] in this thesis.

4.1 Contact kinematics

Contact kinematics describes the relative motion of surface points of three-dimensional bodies, which can come into contact. Following standard approaches, the contact pairing of two bodies is defined by a master-slave relation, in which kinematic quantities are evaluated on the master surface and the contact contribution to the thermomechanical contact problem is integrated over the slave's surface. In this thesis, the problem definition is restricted to the contact of a deformable slave body with a rigid master surface, which is described by an analytical continuously differentiable function $\boldsymbol{X}_M = \boldsymbol{X}_M(\boldsymbol{\xi})$ in the domain of convective surface coordinates $\boldsymbol{\xi}$. At a position (ξ_1, ξ_2) on the master surface, contact quantities are defined using a local coordinate system consisting of the tangent vectors $\boldsymbol{A}_1$ and $\boldsymbol{A}_2$ and the normal vector $\boldsymbol{N}$. The tangent vectors

$$\boldsymbol{A}_i = \frac{\partial \boldsymbol{X}_M(\xi_1, \xi_2)}{\partial \xi_i}, \text{ with } i = 1, 2 \tag{4.1}$$

are defined as the covariant derivatives of the contravariant position vector $\boldsymbol{X}_M$. By means of this, the unit surface normal is then defined as

$$\boldsymbol{N} = \frac{\boldsymbol{A}_i \times \boldsymbol{A}_j}{\|\boldsymbol{A}_i \times \boldsymbol{A}_j\|}. \tag{4.2}$$

With these definitions, the closest projection of the slave point onto the master surface can be calculated by solving the minimization problem posed by

$$d(\xi_1, \xi_2) \quad = \quad \arg\min \left\| \boldsymbol{x}_s - \bar{\boldsymbol{X}}_M \left(\bar{\boldsymbol{\xi}}(\boldsymbol{x}_s) \right) \right\|,$$

see [Wriggers, 2006] for details.

In order to distinguish between contact and separation, the normal penetration function is introduced

$$d_N = -\left(\boldsymbol{x}_s - \bar{\boldsymbol{X}}_M \right) \cdot \bar{\boldsymbol{N}} \begin{cases} < 0 & \text{no contact} \\ = 0 & \text{contact} \\ > 0 & \text{peneration} \end{cases}, \tag{4.3}$$

which results in a scalar measure of the distance to the closest point. The time derivative of the penetration yields

$$\dot{d}_N = -\left(\dot{\boldsymbol{x}}_s - \dot{\bar{\boldsymbol{X}}}_M \right) \cdot \bar{\boldsymbol{N}} - \left(\boldsymbol{x}_s - \bar{\boldsymbol{X}}_M \right) \cdot \dot{\bar{\boldsymbol{N}}}. \tag{4.4}$$

This penetration velocity is required for the description of viscoelastic contact problems. Note that $\dot{\bar{\boldsymbol{N}}}$ vanishes on flat surfaces.

The calculation of frictional contact reactions requires a measure of tangential relative motion, which is defined by the tangential gap

$$s_i = \left(\boldsymbol{x} - \bar{\boldsymbol{X}}_M \right) \cdot \bar{\boldsymbol{A}}_i \tag{4.5}$$

and its time derivative, the relative tangential velocity

$$\dot{\boldsymbol{s}} = \left(\boldsymbol{I} - \bar{\boldsymbol{N}}^{\mathrm{T}}\bar{\boldsymbol{N}}\right) \cdot \left(\dot{\boldsymbol{x}}_s - \dot{\bar{\boldsymbol{X}}}_M\right). \tag{4.6}$$

With these definitions, the stick condition is stated as

$$s_i = \left(\boldsymbol{x} - \bar{\boldsymbol{X}}_M\right) \cdot \bar{\boldsymbol{A}}_i = 0 \Leftrightarrow \dot{s}_i = 0. \tag{4.7}$$

4.2 Balance of energy in the contact interface

The calculation of thermomechanical contact interaction accounting for viscous dissipation of the tread rubber, frictional heating, and conductive heat transfer requires the solution of the balance of energy in the contact interface. A detailed discussion on this topic is presented in [Laursen, 2003; Willner, 2003; Wriggers, 2006].

In order to reformulate the balance of energy (2.42) in terms of the contact interface, the nominal surface traction is defined by projection of the *first Piola-Kirchhoff stress tensor* $\boldsymbol{P}$ along the surface normal $\boldsymbol{N}$, which yields

$$\boldsymbol{T} = -\boldsymbol{P} \cdot \boldsymbol{N} = P\boldsymbol{N} + \sum_i T^i \boldsymbol{A}_i. \tag{4.8}$$

This traction is separated into a nominal normal pressure P and nominal tangential tractions T^i in the direction of the tangent vectors $\boldsymbol{A}_i$. Furthermore, the outward nominal heat fluxes over the contact boundaries are defined as

$$-\boldsymbol{Q}^W \cdot \boldsymbol{N} = Q_c^W \quad \text{and} \quad \boldsymbol{Q}^R \cdot \boldsymbol{N} = Q_c^R \tag{4.9}$$

where Q_c^W is the heat flux from the tire into the contact interface using $\boldsymbol{n}_s = -\boldsymbol{N}$, and Q_c^R is the heat flux transferring energy from the road into the contact interface.

With these definitions the balance of energy in the contact interface reads

$$\dot{e}_c = P\dot{d}_N + \boldsymbol{T} \cdot \dot{\boldsymbol{s}} + Q_c^W + Q_c^R. \tag{4.10}$$

Furthermore, the thermodynamically consistent formulation of constitutive contact models requires the fulfillment of the entropy inequality in the interface, which is defined as

$$\dot{\eta}_c \Theta_c \geq \frac{Q_c^W}{\Theta^W}\Theta_c + \frac{Q_c^R}{\Theta^R}\Theta_c. \tag{4.11}$$

Furthermore, the total slip $\boldsymbol{s}$ and the sliding velocity $\dot{\boldsymbol{s}}$ are separated into

$$\boldsymbol{s} = \boldsymbol{s}^{\mathrm{el}} + \boldsymbol{s}^{\mathrm{pl}} \quad \text{and} \quad \dot{\boldsymbol{s}} = \dot{\boldsymbol{s}}^{\mathrm{el}} + \dot{\boldsymbol{s}}^{\mathrm{pl}}, \tag{4.12}$$

where the elastic components $\boldsymbol{s}^{\mathrm{el}}$ and $\dot{\boldsymbol{s}}^{\mathrm{el}}$ occur only in case of regularized treatment of the friction law (e.g. *Coulomb friction*), which allows for an elastic relative motion. Otherwise only the plastic components $\boldsymbol{s}^{\mathrm{pl}}$ and $\dot{\boldsymbol{s}}^{\mathrm{pl}}$ are present. This analogy to plasticity has been recognized first in [Michalowski and Mroz, 1978]

Analogous to the continuum formulation, the *Legendre transform* of the strain energy function Ψ_c is calculated by

$$\Psi_c\left(d_N, \alpha_{\mathrm{v}}^{(i)}, \boldsymbol{s}^{\mathrm{el}}, \eta_c\right) = e_c - \eta_c \Theta_c \tag{4.13}$$

$$\dot{\Psi}_c = \frac{\partial \Psi_c}{\partial d_N}\dot{d}_N + \sum_i \frac{\partial \Psi_c}{\partial \alpha_{\mathrm{v}}^{(i)}}\dot{\alpha}_{\mathrm{v}}^{(i)} + \frac{\partial \Psi_c}{\partial \boldsymbol{s}^e} \cdot \dot{\boldsymbol{s}}^{\mathrm{el}} + \frac{\partial \Psi_c}{\partial \Theta_c}\Theta_c = \dot{e}_c - \dot{\eta}_c \Theta_c - \eta_c \dot{\Theta}_c, \tag{4.14}$$

as well as its time derivative $\dot{\Psi}_c$. Inserting these definitions into (4.11) results in the *Clausius-Duhem inequality*

$$\begin{aligned} &\left(P - \frac{\partial \Psi_c}{\partial d_N}\right)\dot{d}_N + \left(\boldsymbol{T} - \frac{\partial \Psi_c}{\partial \boldsymbol{s}^e}\right) \cdot \dot{\boldsymbol{s}}^e - \left(\eta_c + \frac{\partial \Psi_c}{\partial \Theta_c}\right)\dot{\Theta}_c \\ &+ \sum_i \frac{\partial \Psi_c}{\partial \alpha_{\mathrm{v}}^{(i)}}\dot{\alpha}_{\mathrm{v}}^{(i)} + \boldsymbol{T} \cdot \dot{\boldsymbol{s}}^{\mathrm{pl}} + \frac{Q_c^W}{\Theta^W}(\Theta_W - \Theta_c) + \frac{Q_c^R}{\Theta^R}(\Theta_c - \Theta_R) \geq 0, \end{aligned} \tag{4.15}$$

which requires the constitutive contact model to fulfill

$$P = \frac{\partial \Psi_c}{\partial d_N},\ \boldsymbol{T} = \frac{\partial \Psi_c}{\partial \boldsymbol{s}^{\mathrm{el}}},\ \text{and}\ \eta_c = -\frac{\partial \Psi_c}{\partial \Theta_c}. \tag{4.16}$$

The remainder of the inequality results in the calculation of dissipation

$$\mathcal{D}_c^{\mathrm{mech}} = \frac{\partial \Psi_c}{\partial \alpha_{\mathrm{v}}^{(i)}}\dot{\alpha}_{\mathrm{v}}^{(i)} + \frac{\partial \Psi_c}{\partial \boldsymbol{s}^{\mathrm{el}}} \cdot \dot{\boldsymbol{s}}^{\mathrm{pl}} \geq 0 \tag{4.17}$$

$$\mathcal{D}_c^{\mathrm{therm}} = \frac{Q_c^W}{\Theta_W}(\Theta_W - \Theta_c) + \frac{Q_c^R}{\Theta_R}(\Theta_c - \Theta_R) \geq 0, \tag{4.18}$$

where both the mechanical $\mathcal{D}_c^{\mathrm{mech}}$ as well as the thermal dissipation $\mathcal{D}_c^{\mathrm{therm}}$ must be non-negative.

The formulation of the strain energy function for the calculation of contact tractions is presented in the next section. The nominal heat fluxes are modeled by

$$Q_c^W = k_{\mathrm{Wc}}(\Theta_W - \Theta_c) \text{ and } Q_c^R = k_{\mathrm{Rc}}(\Theta_c - \Theta_R), \tag{4.19}$$

with the heat conduction coefficients k_{Wc} and k_{Rc}. Neglecting the heat capacity of the trapped debris, the resulting heat flux in the contact interface yields

$$Q_c^{WR} = -\rho_{\mathcal{D}}\frac{\partial \Psi_c}{\partial \alpha_{\mathrm{v}}^{(i)}}\dot{\alpha}_{\mathrm{v}}^{(i)} - \rho_{\mathcal{D}}\frac{\partial \Psi_c}{\partial \boldsymbol{s}^{\mathrm{el}}} : \dot{\boldsymbol{s}}^{\mathrm{pl}} + h_{\mathrm{WR}}(\Theta_W - \Theta_R), \tag{4.20}$$

with the effective conductivity of the contact interface k_{WR} and the partition coefficient $\rho_{\mathcal{D}}$ that describes the amount of mechanical dissipation entering the wheel. Note that both coefficients can be functions of state variables such as pressure and temperature, see [Wriggers and Miehe, 1994; Hofstetter, 2004].

4.3 Contact constraint enforcement

Different standard techniques for the enforcement of contact constraints have been developed in the last decades, see [Laursen, 2003; Wriggers, 2006; Yastrebov, 2013]. Here, well established standard methods are *Penalty regularizations*, *Lagrangian multipliers*, and the *Augmented Lagrangian multiplier method*, all of which are also available in many commercial codes. The different techniques vary in computational costs, precision, effort of implementation, and stability. Their common feature is an enhancement of the weak form of the balance of linear momentum (3.50) $\mathcal{G}_{\text{mech}} = \mathcal{G}_{\boldsymbol{u}} + \mathcal{G}_c$ by the contact virtual work

$$\mathcal{G}_c(\boldsymbol{u}, \delta\boldsymbol{u}) = \int_{\partial_c\mathcal{B}} P\delta d_N + \boldsymbol{T}_T \cdot \delta\boldsymbol{s} \, \mathrm{d}A \tag{4.21}$$

changing the boundary separation, in which boundary conditions are applied, into

$$\partial\mathcal{B} = \partial_{\boldsymbol{u}}\mathcal{B} \cup \partial_{\boldsymbol{t}}\mathcal{B} \cup \partial_c\mathcal{B} \wedge \partial_{\boldsymbol{u}}\mathcal{B} \cap \partial_{\boldsymbol{t}}\mathcal{B} \cap \partial_c\mathcal{B} = \emptyset, \tag{4.22}$$

in which the contact area $\partial_c\mathcal{B}$ is unknown and needs to be determined by the algorithm.

4.3.1 Normal contact constraint

In this thesis an *Augmented Lagrangian multiplier method* is applied for the mesoscale rough surface contact problem as well as for macroscale rolling contact simulations on the flat surface. In these contact scenarios, the precise fulfillment of the non-penetration condition yield the *Karush-Kuhn-Tucker* complementary conditions

$$d_N \leq 0; P \geq 0 \text{ and } Pd_N = 0. \tag{4.23}$$

The contact pressure is hereby evaluated in terms of the *Uzawa algorithm* as

$$P = \max[\alpha_N + \varepsilon_N d_N, 0], \tag{4.24}$$

where ε_N is a penalty parameter. The *Augmented Lagrange multiplier* α_N is held fixed during the contact iterations and updated each time this solution reaches convergence, see [Laursen, 2003]. As a benefit of this update scheme, the size of the stiffness matrix is constant and it remains symmetric for unilateral contact. In general, the desired accuracy of the solution is reached after few augmentation steps using comparably small penalty parameters, which avoids ill-conditioning and allows for larger load step sizes than an equivalently accurate *Penalty method*. However, a weak point of the *Uzawa algorithm* is the C^0-continuity of its contact potential, which results in a non-smooth transition of the contact state (change of the active set). A more robust and efficient *Augmented*

Lagrangian multiplier contact constraint enforcement method based on a C^1-continuous contact potential has been presented in [Pietrzak and Curnier, 1999]. This advantage comes at the cost of introducing the contact pressure as an additional degree of freedom (*Lagrangian multiplier*), which results in a larger non-symmetric stiffness matrix.

In technical applications, the stiffness of the contact interface often cannot be assumed to be infinite. Especially the homogenized description of rough surface interaction is often realized using a nonlinear regularization, see [Willner, 2003].

4.3.2 Rubber friction

In order to calculate the correct pressure distribution in the tire's footprint, the friction response of tread rubber must be taken into account. In experimental studies such as that presented in [Hofstetter, 2004], the friction response of rubber materials on rough surfaces has been observed to be highly dependent of pressure, temperature and velocity. In this contact pairing the soft rubber material is penetrated by much stiffer surface asperities. The relative sliding motion of the rubber material on top of these asperities in conjunction with the thermo-viscoelastic material response presented in section 3.5 results in the so-called plowing component of the friction behavior. This effect is also present in the absence of adhesion on lubricated surfaces and causes the above mentioned dependence on service conditions. Furthermore, the large local strains at high strain rates that are caused by the plowing of surface asperities result in high local dissipation, which induce a severe temperature increase in the contact interface.

In order to capture these phenomena, a general form of a regularized friction law is applied

$$\boldsymbol{T}_T = \min\left[\alpha_T \|\boldsymbol{s}\|, \mu\left(p, \|\dot{\boldsymbol{s}}\|, \Theta\right)|p|\right] \frac{\boldsymbol{s}}{\|\boldsymbol{s}\|}, \tag{4.25}$$

which is suitable to account for the dominant effects in rubber friction. In this context, the common approach of Coulomb's friction law, which is based on a constant friction coefficient μ, cannot depict rubber friction phenomena for large variations of influence parameters.

In this thesis, the friction model presented in [Huemer et al., 2001a], and further elaborated in [Hofstetter et al., 2006] is applied. The friction coefficient is calculated via

$$\mu\left(P, \|\dot{\boldsymbol{s}}\|\right) = \left(\alpha|p|^{n-1} + \beta\right)\left(a + \frac{b}{\|\dot{\boldsymbol{s}}\|^e} + \frac{c}{\|\dot{\boldsymbol{s}}\|^{2e}}\right)^{-1}, \tag{4.26}$$

where the first term represents the pressure dependence, and the second term depicts the influence of the sliding velocity. The temperature dependence is achieved by the *Williams-Landel-Ferry equation* (WLF-equation), see [Williams et al., 1955]. This function relates

Table 4.1: Modified parameters for the friction law $\mu\left(P, \|\dot{\boldsymbol{s}}\|, \Theta\right)$, see Hofstetter [2004].

Pressure dependent part	$\alpha_h = 0.1399$	$\beta_h = 0.1841$	$n_h = 0.8680$	
Velocity dependent part	$a = 0.9203$	$b = -1.1188$	$c = 0.9677$	$e = 0.1672$
WLF-transform	$d_1 = 43.1$	$d_2 = 509.4$	T_{ref} =20 °C	T_g = -50 °C

relaxation times to service temperature, which can be used to calculate the equivalent sliding velocity (loading frequency) at reference temperature

$$\dot{\boldsymbol{s}}_{\text{ref}} = \frac{a_{\Theta,\text{cur}}}{a_{\Theta,\text{ref}}} \dot{\boldsymbol{s}}_{\text{cur}} \tag{4.27}$$

for the sliding velocity $\dot{\boldsymbol{s}}_{\text{cur}}$ at the current temperature, so that an increase in temperature is equivalent to an increase in sliding speed. Here, the projection coefficients $a_{\Theta,\text{cur}}, a_{\Theta,\text{ref}}$ are defined as

$$\log_{10} a_{\Theta,i} = \frac{d_1(\Theta_i - \Theta_g + 50°\text{C})}{d_2 + (\Theta_i - \Theta_g + 50°\text{C})},\ i = \{\text{cur, ref}\} \tag{4.28}$$

with the two additional material parameters d_1, d_2 and Θ_g being the glass transition temperature. The friction coefficient is then evaluated for the equivalent sliding velocity at reference temperature along the so-called master-curve, to which model parameters α, β, n as well as a, b, c, e are fit. See [Huemer et al., 2001a] for details on the mastering process for experimental data.

In Figure 4.1 (a) and (b) the resulting friction coefficient for the material parameters given in Table 4.1 is illustrated. It can be observed in both figures that the friction coefficient first tends towards a maximum value, and then decreases with sliding speed. This effect increases at small contact pressures, which results in a larger friction coefficient, see Figure 4.1 (a). As a result of the WLF-equation (4.28) that depicts the temperature dependence of rubber friction, the maximum of the master-curve is shifted towards smaller sliding speeds for increasing service temperatures, see Figure 4.1 (b).

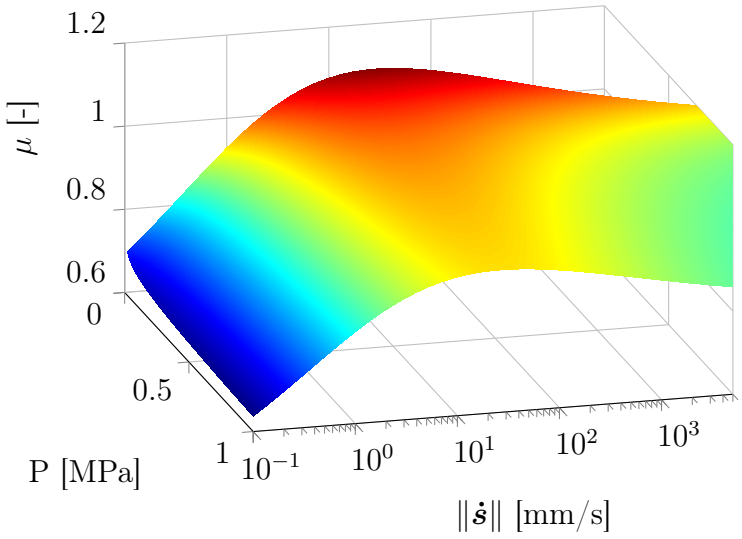

(a) Pressure dependence at reference temperature $\Theta = 20$ °C.

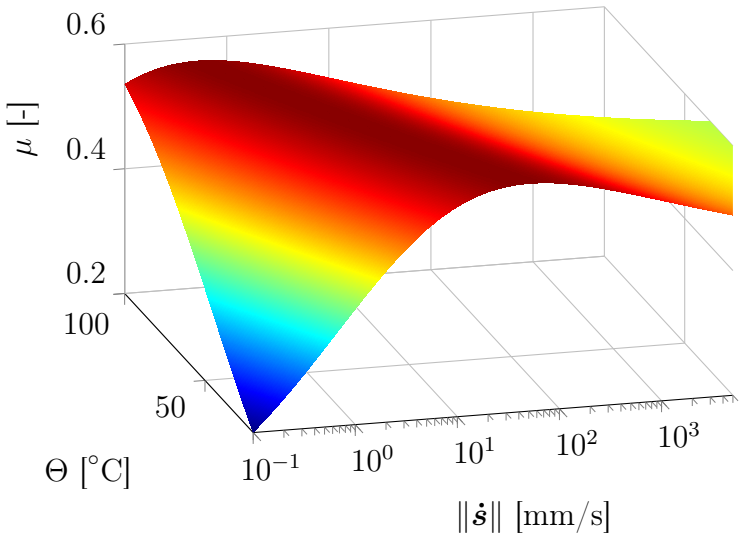

(b) Temperature dependence for $P = 1$ MPa.

Figure 4.1: Friction coefficient at varying pressures and temperatures over sliding speed.

5 Homogenization of unilateral rough surface contact

Accounting for tread-road interaction in rolling resistance calculations is an unsolved research problem of high economical relevance. As shown in the review on the state of the art in chapter 1, there is presently no convincing approach to incorporate the nonlinear large deformation contact interaction of tread rubber with the mesoscopic rough road surface.

In this chapter a novel approach is presented, which represents the stochastic average contact behavior of a single three-dimensional tread block with the random rough road surface in terms of a one-dimensional homogenized constitutive contact model. The aim for this formulation is to approximate the average nominal contact pressure and the volume average dissipation resulting from the thermo-viscoelastic response of the bulk material preserving the external energy in the load cycle (consistence of energy).

In order to achieve this goal, the basic concepts of homogenization techniques are reviewed first in this chapter, which points out their restriction to sub-scales. Thereafter, the special case of contact homogenization is studied, and the criteria for consistency of energy are stated. Based on these definitions, a novel rough surface contact homogenization strategy for the unilateral tread-road interaction based on a reformulation of the bulk material model is developed. The resulting constitutive contact model preserves the characteristics of the thermo-viscoelastic material response.

The identification of the average tread-road contact interaction behavior with random rough road surfaces requires the solution of a stochastic contact problem, namely a *random Signorini problem*. Its mathematical treatment is presented in the second section of this chapter. After the introduction of this general basis, the statistical characterization of rough surfaces is briefly reviewed. These characteristic quantities are then calculated and compared for a smooth and a rough measured road surface. Later on in this chapter, the average contact behavior on these surfaces is evaluated and approximated by constitutive contact models. This homogenized representation finally allows for an estimation of the influence of surface roughness on rolling resistance in section 6.2.

In the fourth part of this chapter, the numerical results for energy-consistent homogenization of a tread block in contact with a sphere are validated. In a next step, the evaluation of the average rough surface contact behavior of single tread blocks on the measured road surfaces by means of a *Monte Carlo simulation* is presented. The homogenization of this response results in a set of material parameters for the constitutive contact model, which are applied in the rolling resistance calculations in section 6.2.

5.1 Contact homogenization

5.1.1 General aspects of homogenization in continuum mechanics

Computational homogenization techniques aim for the macroscopic description of microscopically heterogeneous materials assuming C^1-continuous *Boltzmann kinematics*. Furthermore, these techniques are used to describe material phenomena occurring on smaller length scales, especially damage. Their goal is to identify the effective mechanical properties, see e.g. [Miehe, 2003] and [Temizer and Zohdi, 2007], as well as effective thermomechanical properties, see e.g. [Özdemir et al., 2008]. In general, these approaches are based on the assumption that the microscopic length scale $l << L$ is much smaller than the macroscopic one L and therefore allows for a separation of scales. Under this assumption, a representative volume element (RVE) $\mathcal{B}_m$ can be found, which describes the random heterogeneous microstructure in the vicinity of a material point on the macroscale. Consistent scale transition of quantities in the RVE is then ensured by the volume averaging operator

$$\langle \bullet \rangle = \frac{1}{V_m} \int_{\mathcal{B}_m} \bullet(\boldsymbol{X}) \, \mathrm{d}V_m. \tag{5.1}$$

In order to shorten the notation, the location of the quantity $\boldsymbol{X}$ is omitted in the following. Within the RVE, the microscopic displacement field

$$\boldsymbol{u}_m = \boldsymbol{u} + \boldsymbol{u}_f \tag{5.2}$$

is assumed to consist of small local fluctuations $\boldsymbol{u}_f$ of the macroscopic displacement $\boldsymbol{u}$, which vanish in the volume average $\langle \boldsymbol{u}_f \rangle = 0$. Furthermore, the displacement field is assumed to have no jumps ($[\![\boldsymbol{u}]\!] = 0$) on the boundary of the RVE $\partial\mathcal{B}_m$. This approach is called first order homogenization, in which only the first order term of the Taylor series expansion of the displacement field

$$\Delta\boldsymbol{x} = \frac{\partial \boldsymbol{x}}{\partial \boldsymbol{X}} \cdot \Delta\boldsymbol{X} + \mathcal{O}\left(\Delta\boldsymbol{X}^2\right), \tag{5.3}$$

is accounted for using average first order gradients $\boldsymbol{F} = \frac{\partial \boldsymbol{x}}{\partial \boldsymbol{X}}$. Consequently, the variations of the macroscopic fields need to be sufficiently small. Furthermore, the stress field is assumed to be divergence free, which means that no inertia and body forces are acting on the microscale.

The commonly used base quantity to describe the kinematics of the RVE is the average deformation gradient

$$\langle \boldsymbol{F} \rangle = \frac{1}{V_m} \int_{\mathcal{B}_m} \boldsymbol{F} \, \mathrm{d}V_m = \frac{1}{V_m} \int_{\partial\mathcal{B}_m} \boldsymbol{\varphi} \otimes \boldsymbol{N} \, \mathrm{d}A_m, \tag{5.4}$$

which is calculated by volume integration, and can also be expressed by a surface integral with the divergence theorem. This fact can be used to enforce an equivalent uniform displacement boundary condition. Based on this definition, dependent quantities are defined, e.g. the *right Cauchy Green tensor* $\tilde{\boldsymbol{C}} = \langle \boldsymbol{F} \rangle^{\mathrm{T}} \cdot \langle \boldsymbol{F} \rangle$ and the *Green-Lagrange strain* $\tilde{\boldsymbol{E}} = \frac{1}{2} \left(\langle \boldsymbol{F} \rangle^{\mathrm{T}} \cdot \langle \boldsymbol{F} \rangle - \boldsymbol{1} \right)$. The description of time dependent processes also requires volume averaging of the material velocity gradient

$$\left\langle \dot{\boldsymbol{F}} \right\rangle = \frac{1}{V_m} \int\limits_{\mathcal{B}_m} \dot{\boldsymbol{F}} \, \mathrm{d}V_m = \frac{1}{V_m} \int\limits_{\partial \mathcal{B}_m} \boldsymbol{v} \otimes \boldsymbol{N} \, \mathrm{d}A_m, \tag{5.5}$$

which is measurable as a surface velocity $\boldsymbol{v}$ of the RVE. The material velocity gradient is related to the spatial velocity gradient $\boldsymbol{l}$ via $\boldsymbol{l} = \mathrm{grad}\boldsymbol{v} = \dot{\boldsymbol{F}} \cdot \boldsymbol{F}^{-1}$.

The macroscopic stress field is then defined in terms of the energy conjugate average *first Piola-Kirchhoff stress tensor*

$$\langle \boldsymbol{P} \rangle = \frac{1}{V_m} \int\limits_{\mathcal{B}_m} \boldsymbol{P} \, \mathrm{d}V_m = \frac{1}{V_m} \int\limits_{\partial \mathcal{B}_m} \boldsymbol{T} \otimes \boldsymbol{X} \, \mathrm{d}A_m, \tag{5.6}$$

which can also be expressed as an integral over the tractions along the boundary of the RVE. This quantity can also be expressed as the volume average of the partial derivative of the elastic potential with respect to the deformation gradient

$$\langle \boldsymbol{P} \rangle = \frac{1}{V_m} \int\limits_{\mathcal{B}_m} \frac{\partial \Psi}{\partial \boldsymbol{F}} \, \mathrm{d}V_m. \tag{5.7}$$

The material response can be split into its different contributions from the constitutive material model by interchanging the integral and the summation

$$\langle \boldsymbol{P} \rangle = \langle \boldsymbol{P}_{\mathrm{vol}} \rangle + \langle \boldsymbol{P}_{\mathrm{dev}} \rangle + \sum_i \left\langle \boldsymbol{P}^i_{\mathrm{neq}} \right\rangle, \tag{5.8}$$

which later on allows for a separate identification of mapping functions and constitutive parameters. The dependent *second Piola-Kirchhoff stress tensor* $\tilde{\boldsymbol{S}}$ is then calculated via

$$\tilde{\boldsymbol{S}} = \langle \boldsymbol{F} \rangle^{-1} \cdot \langle \boldsymbol{P} \rangle = 2 \frac{\partial \bar{\Psi} \left(\tilde{\boldsymbol{C}}, \Theta, \tilde{\boldsymbol{\alpha}}^{(i)}_{\mathrm{v}} \right)}{\partial \tilde{\boldsymbol{C}}}. \tag{5.9}$$

If viscous material behavior is observed, the volume average internal dissipation (3.48) also needs to be transmitted to the macroscale as

$$\langle \mathcal{D}_{\mathrm{int}} \rangle = \frac{1}{V_m} \int\limits_{\mathcal{B}_m} \frac{1}{\eta_i} \bar{\boldsymbol{A}}^{(i)}_{\mathrm{v}} : \bar{\boldsymbol{A}}^{(i)}_{\mathrm{v}} \, \mathrm{d}V_m \text{ with } E_{\mathcal{D}_{\mathrm{int}}} = \int_0^T \langle \mathcal{D}_{\mathrm{int}} \rangle \, \mathrm{d}t, \tag{5.10}$$

which is the dissipated energy over a load cycle with a duration of T. For reasons of completeness, the calculation of the elastically stored energy in the macroscale system is given by

$$W = \frac{1}{V} \int_0^T \left\langle \boldsymbol{P} : \dot{\boldsymbol{F}} \right\rangle \, \mathrm{d}t. \tag{5.11}$$

With the above, the requirement of energetic consistency of homogenization is ensured by the equivalence of macroscopic and averaged microscopic stress power

$$\langle \boldsymbol{P} \rangle : \left\langle \dot{\boldsymbol{F}} \right\rangle = \left\langle \boldsymbol{P} : \dot{\boldsymbol{F}} \right\rangle = \frac{1}{V_m} \int\limits_{\mathcal{B}_m} \boldsymbol{P} : \dot{\boldsymbol{F}} \, \mathrm{d}V_m = \frac{1}{V_m} \int\limits_{\partial \mathcal{B}_m} \boldsymbol{t} \cdot \boldsymbol{v} \, \mathrm{d}A_m \tag{5.12}$$

also known as the *average work theorem* and, in terms of small deformations, as the *Hill criterion*. It states that fluctuations of the internal quantities do not affect the macroscopic power response. Based on that theorem, only three types of boundary conditions can fulfill this equality, namely:

- Uniform displacements,
- Uniform tractions,
- Periodic boundary conditions,

see e.g. [Miehe, 2003] for details on the proof. Consequently, this criterion cannot be fulfilled a priori for the mesoscale contact problem due to the boundary conditions imposed by the tire structure. Therefore, a stochastic homogenization is applied to represent the contact behavior of tread block on the rough road surface.

The limitation of scale separation $l << L$ and the necessity of vanishing oscillations of the displacement field along the boundary ($[\![\boldsymbol{u}]\!] = 0$) in first-order homogenization methods can be overcome by second-order homogenization techniques, see e.g. [Castañeda, 1996], [Lopez-Pamies and Ponte Castañeda, 2003] and more recently [Kouznetsova et al., 2004]. This is achieved by accounting for the quadratic term of the Taylor series expansion

$$\Delta \boldsymbol{x} = \boldsymbol{F} \cdot \Delta \boldsymbol{X} + 0.5 \Delta \boldsymbol{X} \cdot \mathbb{G} \cdot \Delta \boldsymbol{X} + \mathcal{O}\left(\Delta \boldsymbol{X}^3\right) \tag{5.13}$$

of the macroscopic fields, where the third order tensor $\mathbb{G}$ depicts the quadratic parts of the gradient. Obviously, the second order homogenization can only be realized with a C^1-continuous continuum description on the macroscale.

5.1.2 Homogenization of contact interface phenomena

The homogenization of surface phenomena in contact interfaces requires an adaption of the continuum framework for heterogeneous materials, as admissible boundary conditions

cannot be found. Therefore, it is assumed that the height h of the contact interface is negligible compared to the system dimension H, which is equivalent to a separation of scales $h << H$. Consequently, the homogenization is executed along an interface area $\partial_c \mathcal{B}_m$ rather then in a volume element. In the papers of [Temizer and Wriggers, 2008], [Temizer and Wriggers, 2010a] and [Temizer and Wriggers, 2010b], a first order homogenization framework for contact interfaces ensuring thermomechanical consistency was developed. This framework accounts for large deformations, viscoelastic effects and also for either the presence of third bodies or rough surfaces.

Analogous to the homogenization of the continuum, a surface average operator

$$\bar{\bullet} = \frac{1}{A} \int_{\partial_c \mathcal{B}_m} \bullet(\boldsymbol{x}) \, \mathrm{d}A. \tag{5.14}$$

is defined in the interface $\partial_c \mathcal{B}_m$. With this operator, the average gap vector $\bar{\boldsymbol{d}} = \overline{\boldsymbol{u}_m - \boldsymbol{u}_s}$ and the average tangential traction $\bar{\boldsymbol{t}}$ are defined as basic quantities for describing the behavior of the contact interface, which follows the concept of using the volume averages of the deformation gradient (5.4) and the *first Piola-Kirchhoff stress tensor* (5.6) to describe the microscale continuum. Both $\bar{\boldsymbol{d}}$ and $\bar{\boldsymbol{t}}$ were introduced for general contact problems in chapter 4. With these quantities an equivalent local average work rate criterion (5.12)

$$\overline{\boldsymbol{t} \cdot \boldsymbol{v}} = \bar{\boldsymbol{t}} \cdot \bar{\boldsymbol{v}} \tag{5.15}$$

can be derived for the contact interface, i.e. the balance of energy (4.10), where $\bar{\boldsymbol{v}}$ is the relative velocity of the surfaces. This relation can be separated by projection onto the respective base vectors in the macroscopic configuration into

$$\overline{\boldsymbol{t} \cdot \boldsymbol{v}} = \overline{p \, \dot{d}_N} + \overline{\boldsymbol{\tau} \cdot \dot{\boldsymbol{\xi}}_\alpha} = \bar{p} \, \dot{\bar{d}}_N + \sum_i \bar{\tau}^\alpha \, \dot{\bar{\xi}}_i, \tag{5.16}$$

where $\dot{\bar{d}}_N = \boldsymbol{v} \cdot \boldsymbol{n}$ is the normal penetration velocity and $\dot{\bar{\xi}}_i = \boldsymbol{v} \cdot \boldsymbol{a}_i$ is the parametric sliding velocity in the tangential direction i.

In [Temizer and Wriggers, 2008] the effective tangential traction $\bar{\boldsymbol{\tau}} = \bar{\mu} \bar{p} \frac{\bar{\boldsymbol{v}}}{\|\bar{\boldsymbol{v}}\|}$ of a viscoelastic rubber block sliding on a flat surface with microscopic rolling particles in the contact interface was studied. Due to the material properties of the rubber material the effective friction coefficient $\bar{\mu} = \bar{\mu}(\bar{p}, \|\bar{\boldsymbol{v}}\|)$ depends on contact pressure $\bar{p}$ and sliding speed $\|\bar{\boldsymbol{v}}\|$. In order to evaluate this effective friction coefficient, a microscale model resolving the interaction with single particles was simulated in that study. Here, the interface area (top surface) of this microscale model was subjected to the macroscopic average contact pressure $\bar{p}$ and dragged with a constant velocity $\bar{\boldsymbol{v}}$, whilst symmetric boundary conditions were applied along the lateral sides assuming periodicity. As the traction response of this

sliding motion is very oscillatory, the effective friction coefficient

$$\bar{\mu}(\bar{p}, \|\bar{\boldsymbol{v}}\|) = \frac{1}{t} \int_{t_0}^{t} \frac{\|\bar{\boldsymbol{\tau}}\|}{\bar{p}} \, \mathrm{d}t \tag{5.17}$$

was calculated by averaging over time. In [Reinelt and Wriggers, 2010] and later in [De Lorenzis and Wriggers, 2013] the average tangential contact response of a rubber block sliding on a rough surface was calculated likewise.

The description of tread-road interaction results in a contact homogenization problem with random heights of the master surface $\mathbf{x}_M$. Here, the distribution of asperity shapes results in a large autocorrelation length that determines the size of a representative contact element (RCE). As this size exceeds the size of a single tread block, the classical first order FE^2 method applied in [Temizer and Wriggers, 2010b] is not suitable, and thus stochastic homogenization becomes necessary in order to formulate a constitutive contact model representing the stationary response. The size and the distribution of asperities and their rough texture are characterized by a continuous spectrum of length scales. For this reason, standard homogenization approaches formulated under the assumption of separable scales are not applicable, and consequently no representative contact element can be defined. Therefore, the proposed method is based on stochastic homogenization of the contact interaction of the single tread block with the rough road surface.

5.1.3 Constitutive contact model

In this section, a novel approach is introduced for empirical development of one-dimensional thermomechanical constitutive contact models to represent the homogenized, unilateral, frictionless contact behavior of a three-dimensional tread block on rough road surfaces. The first step in this homogenization is to separate the mesoscale tread blocks from the macroscale tire model by definition of a transition area $\partial\Omega_M$ in between. This allows for a decoupled identification of the structural response of the tread-road interaction. Here, the motion and the temperature of the transition area are prescribed by the tire model, which is consistent with the contact constraint enforcement techniques presented in section 4.3. This definition results in the application of displacement and temperature boundary conditions to the mesoscale model pressing it onto the rough road surface.

The identified mesoscale contact behavior (average contact pressure and average heat flux) is then be represented by a constitutive contact model. As a novel approach, the constitutive contact model is derived directly from the tread's bulk material model assuming an equivalent uniaxial compression test, see Figure 5.1. This constitutive contact model is later used to solve the macroscale contact interaction problem (rolling resistance calculation of tires) accounting for homogenized mesoscale rough surface contact behavior.

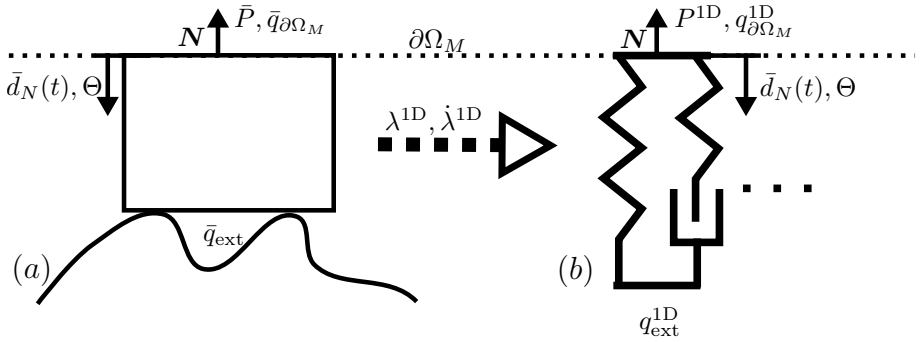

Figure 5.1: Homogenization of rough surface contact interaction in the mesoscale model (a) and the representation by a constitutive contact model assuming uniaxial compression (b) in the transition area.

Evaluation of the homogenized mesoscale contact behavior

The first step in the present study is an investigation of the contact compliance of the tread-road interface, the viscoelastic effects occurring in the load cycle, and the average heat flux. This heat flux results from the heat source by internal mechanical dissipation in the tread rubber, which is reduced by the heat conduction between tread block and road. For this reason, a uniform displacement of the transition area is applied to the upper surface of the tread block, which is analogous to enforcing a penetration of the plane defined by the highest asperity below the tread block.

The mechanical quantity of interest is the average nominal contact pressure

$$\bar{P}\left(\bar{d}_N(t), \Theta\right) = \frac{1}{A_0} \int_{\partial\Omega_M} P\left(\bar{d}_N(t), \Theta\right) \, \mathrm{d}A_M \tag{5.18}$$

in the transition area $\partial\Omega_M$ for the present boundary conditions, namely the current penetration $\bar{d}_N(t)$ which prescribes a penetration rate $\dot{\bar{d}}_N$, and the temperature Θ. The average nominal pressure

$$\bar{P} = \boldsymbol{N} \cdot \bar{\boldsymbol{T}} \tag{5.19}$$

is the normal component of the average nominal surface traction $\bar{\boldsymbol{T}}$ acting on the initial area A_0. Due to the chosen *Dirichlet boundary conditions*, the normal vectors

$$\boldsymbol{N}(\boldsymbol{x}) = \boldsymbol{n}(\boldsymbol{x}) \; \forall \boldsymbol{x} \in \partial\Omega_M, \tag{5.20}$$

of the initial and the current configuration coincide in the transition area. The thermal quantity of interest is the average heat flux

$$\bar{q}_{\partial\Omega_M}\left(\bar{d}_N(t), \Theta\right) = \rho_{\mathcal{D}} \left(\langle \mathcal{D}_{\text{int}} \rangle - \bar{q}_{\text{ext}} \right), \tag{5.21}$$

which is defined as a portion $\rho_{\mathcal{D}}$ of volume average dissipation in the mesoscale model $\langle \mathcal{D}_{\text{int}} \rangle$ reduced by the heat flux over external boundaries $\bar{q}_{\text{ext}}$, e.g. convection on free surfaces and conduction in the tread-road interface.

The evaluation of the average external mechanical power in the transition area must is adapted from the ideas presented in [Temizer and Wriggers, 2008]. In the present case of unilateral contact interaction, it can be calculated via

$$\mathcal{P}_M = \int_{\partial\Omega_M} P\dot{\bar{d}}_N \,\mathrm{d}A = \int_{\Omega_M} \boldsymbol{P} : \dot{\boldsymbol{F}} \,\mathrm{d}V \approx \sum_i R_i(\bar{d}_N)\dot{\bar{d}}_N, \tag{5.22}$$

which is equal to the internal power in the tread block and can be approximated by discrete nodal reaction forces $R_i(\bar{d}_N)$ and prescribed penetration velocity $\dot{\bar{d}}_N$. By time integration, the external mechanical work can be defined in the load cycle

$$\mathcal{W}_M = \int_{t_0}^{T} \mathcal{P}_M \,\mathrm{d}t \approx \sum_n \sum_i \Delta R_i \Delta \bar{d}_N \tag{5.23}$$

and its also discrete approximation. Note that time increments vanish due to $\dot{d}_N \Delta t = \Delta d_N$ in case of discrete load steps with constant velocity.

Derivation of the constitutive contact model

In this thesis, it is assumed that the mesoscale frictionless unilateral tread-road contact interaction is dominated by the contact pressure, and lateral tractions vanish in the stochastic average. With this assumption, the complex rough surface contact scenario can be represented by an equivalent uniaxial compression test. The aim is to formulate of a constitutive contact model, which accurately represents the identified average mesoscale contact interaction as a strain energy function Ψ_C depending on a set of control variables, such as introduced in section 3.1. The application of this constitutive contact model in the transition area then allows for macroscale calculations considering homogenized mesoscale effects. In the following, all equivalent macroscale quantities related to the constitutive contact model are marked by $\bullet^{\mathrm{1D}}$. In this sense, the equivalent macroscale nominal contact pressure

$$P^{\mathrm{1D}}\left(\bar{d}_N(t), \Theta, ...\right) \stackrel{!}{=} \boldsymbol{N}^{\mathrm{T}} \cdot \langle \boldsymbol{P} \rangle \cdot \boldsymbol{N} = \bar{P}\left(\bar{d}_N(t), \Theta\right) \tag{5.24}$$

must be equal to the normal projection of the volume average *first Piola-Kirchhoff stress tensor* $\langle \boldsymbol{P} \rangle$ of the mesoscale model and the mesoscale average nominal pressure $\bar{P}$. The same is required for the equivalent and the average heat flux

$$q^{\mathrm{1D}}_{\partial\Omega_M}\left(\bar{d}_N(t), \Theta, ...\right) \stackrel{!}{=} \bar{q}_{\partial\Omega_M}\left(\bar{d}_N(t), \Theta\right). \tag{5.25}$$

The central objective is to fulfill the equality of mechanical power $\mathcal{P}^{\mathrm{1D}}_M = \mathcal{P}_M$ in order to ensure that the same mechanical energy is stored in the interface. This requirement is expressed in terms of the *first law of thermodynamics*

$$\begin{aligned} \varrho_0 \dot{e} &= \left\langle \boldsymbol{P} : \dot{\boldsymbol{F}} \right\rangle - \mathrm{DIV}\langle \boldsymbol{Q} \rangle + \varrho_0 R \\ &= \frac{1}{h_0} \overline{\boldsymbol{T} \cdot \dot{\bar{\boldsymbol{d}}}} + \bar{q}, \end{aligned} \tag{5.26}$$

where the first equation represents the volume average at the mesoscale, and the second equation is formulated in the transition area $\partial\Omega_M$. Here, h_0 denotes the initial height of the mesoscale model. The reformulation of the balance of energy in terms of entropy

$$\varrho_0\Theta\dot{s} = -\mathrm{DIV}\boldsymbol{Q} + \langle\mathcal{D}_{\mathrm{int}}\rangle + \varrho_0 R, \text{ with } \mathcal{D}_{\mathrm{int}} = \boldsymbol{P} : \dot{\boldsymbol{F}} - \varrho_0\left(\dot{\Psi} + \dot{\Theta}s\right) \geq 0, \tag{5.27}$$

clarifies the necessity of equal internal dissipation $\mathcal{D}_{\mathrm{int}}^{\mathrm{1D}} = \langle\mathcal{D}_{\mathrm{int}}\rangle$, which only results from viscous effects in the bulk material in the context of the isothermal, frictionless rough surface contact problems and acts as a heat source in the tread material. In this context the time integral of the internal dissipation is the loss of mechanical energy, which is the source of rolling resistance. Furthermore, the rate of mechanical power,

$$\left\langle \dot{P}\dot{\bar{d}}_N \right\rangle = \dot{P}^{\mathrm{1D}}\dot{\bar{d}}_N, \tag{5.28}$$

needs to be equal to the mesoscale result in order to ensure a correct representation of viscoelastic effects.

A typical engineering approach to solve the problem stated above could be based on a polynomial fit of the experimental data for the elastic response and on an identification of complex moduli to represent viscoelastic effects. In case of the large deformation problem at hand this method however does not correspond with the definition of complex moduli in the realm of small deformations. It can be seen as another weak point of this approach that in analogy to experimental testing a set of combinations of control variables needs to be simulated for approximating the response over the parametric space. Finally, this data fitting results in an empiric function $P\left(\bar{d}_N, \dot{\bar{d}}_N, \Theta, ...\right)$ where several parameters may have no direct physical meaning. For this reason, parameter identification requires the solution of an optimization problem, which is however no principal disadvantage.

The basic idea for the derivation of a homogenized constitutive contact model to represent rough surface contact interaction is to apply a uniaxial incompressible reformulation Ψ_C of the strain energy function Ψ of the quasi-incompressible material model that was used in the mesoscale calculation. The strain energy function Ψ of most material models in continuum mechanics is a scalar function of the invariants of the *right Cauchy-Green tensor* $\boldsymbol{C}$, as these invariants allow for a frame-invariant, objective modeling. The actual dimensionality or generalization of this formulation first arises in the derivation of the stress response $S = \frac{\partial\Psi}{\partial\boldsymbol{C}}$. In case of the assumed uniaxial compression, the invariants of the *right Cauchy-Green tensor* and subsequently the material response (energy stored in the tread deformation) only depends on the applied scalar stretch. For this reason, the aim of this contact homogenization approach is to find an equivalent stretch-penetration relation $\lambda^{\mathrm{1D}}(\bar{d}_N)$. With this reformulation, the equivalent nominal contact pressure

$$P^{\mathrm{1D}}\left(\lambda^{\mathrm{1D}}, \Theta, \alpha_{\mathrm{v}}^{\mathrm{1D}(i)}\right) = \frac{\partial\Psi_C\left(\lambda^{\mathrm{1D}}, \Theta, \alpha_{\mathrm{v}}^{\mathrm{1D}(i)}\right)}{\partial\bar{d}_N} = \boldsymbol{N}\cdot\frac{\partial\Psi\left(\boldsymbol{F}^{\mathrm{1D}}, \Theta, \boldsymbol{\alpha}_{\mathrm{v}}^{\mathrm{1D}(i)}\right)}{\partial\boldsymbol{F}^{\mathrm{1D}}}\cdot\boldsymbol{N} \tag{5.29}$$

can calculated with a scalar equation, depending on the same control variables that were used in the numerical experiment. By means of this, the equivalent heat flux

$$q^{1\mathrm{D}}_{\partial\Omega_M}\left(\lambda^{1\mathrm{D}},\Theta,\alpha_{\mathrm{v}}^{1\mathrm{D}(i)}\right) \;=\; \rho^{1\mathrm{D}}_M\left(\mathcal{D}^{1\mathrm{D}}_{\mathrm{int}} - q^{1\mathrm{D}}_{\mathrm{ext}}\right) \tag{5.30}$$

is calculated as a portion $\rho^{1\mathrm{D}}_M$ of the equivalent macroscopic dissipation in the dash pots and the penetration-dependent heat conduction in the contact area $q^{1\mathrm{D}}_{\mathrm{ext}} = h^{1\mathrm{D}}\left(\bar{d}_N\right)\mathrm{Grad}\Theta\cdot\boldsymbol{N}$, see Figure 5.1 (b).

Equivalent stretch

The resulting homogenized deformation of the mesoscale model being penetrated by surface asperities is described by the equivalent deformation gradient $\boldsymbol{F}^{1\mathrm{D}}$. Due to the assumption of uniaxial compression, the equivalent deformation gradient only depends on the equivalent stretch $\lambda^{1\mathrm{D}}$, which is therefore the basic kinematic quantity here. The equivalent stretch can be extracted from the volume average deformation gradient $\langle\boldsymbol{F}\rangle$ via

$$\lambda^{1\mathrm{D}}\left(\bar{d}_N\right) = \sqrt{\min\text{ Eigenvalue}\left(\langle\boldsymbol{F}\rangle^{\mathrm{T}}\cdot\langle\boldsymbol{F}\rangle\right)}. \tag{5.31}$$

The evaluation of this definition at different prescribed penetration depths $\bar{d}_N$ results in an equivalent stretch-penetration relation that represents the homogenized compression of the mesoscale model. Consequently, this relation depends on the model geometry, the applied boundary conditions and the statistical characteristics of surface roughness. Note that the discrete evaluations of (5.31) obtained from numerical experiments need to be approximated by a continuous analytical function, e.g. a polynomial, in order to apply the constitutive contact model in macroscale computations. This approximation results in a minimization problem, which is discussed in section 5.4.

The upper bound for the equivalent stretch-penetration relation is defined by the contact interaction with a flat surface, on which all normal compression results in tangential stretch. This contact behavior can be described by $\lambda^{1\mathrm{D}}(\bar{d}_N) = 1 - \bar{d}_N/h_0$, where h_0 is the initial height of the mesoscale model. This fact implies that the deformation $u^{1\mathrm{D}} = \lambda^{1\mathrm{D}}h_0$ of the assumed equivalent compression test is smaller on a rough surface than the prescribed displacement of the mesoscale model $u^{1\mathrm{D}} \leq \bar{d}_N$.

With the definition of the equivalent stretch $\lambda^{1\mathrm{D}}$ in (5.31), dependent equivalent kinematic quantities can be derived assuming incompressibility $J^{1\mathrm{D}} = \det\boldsymbol{F}^{1\mathrm{D}} = 1$

$$\boldsymbol{F}^{1\mathrm{D}} = \begin{bmatrix} \sqrt{\frac{1}{\lambda^{1\mathrm{D}}}} & 0 & 0 \\ 0 & \sqrt{\frac{1}{\lambda^{1\mathrm{D}}}} & 0 \\ 0 & 0 & \lambda^{1\mathrm{D}} \end{bmatrix}, \quad \boldsymbol{C}^{1\mathrm{D}} = \left(\boldsymbol{F}^{1\mathrm{D}}\right)^{\mathrm{T}}\cdot\boldsymbol{F}^{1\mathrm{D}} \begin{bmatrix} \frac{1}{\lambda^{1\mathrm{D}}} & 0 & 0 \\ 0 & \frac{1}{\lambda^{1\mathrm{D}}} & 0 \\ 0 & 0 & \left(\lambda^{1\mathrm{D}}\right)^2 \end{bmatrix}. \tag{5.32}$$

Here, $\boldsymbol{F}^{1\mathrm{D}}$ denotes the equivalent deformation gradient, and $\boldsymbol{C}^{1\mathrm{D}}$ is the equivalent *right Cauchy-Green tensor*. By means of that, the equivalent *Green-Lagrange strain* is defined

as $\boldsymbol{E}^{1\mathrm{D}} = 0.5\left(\boldsymbol{C}^{1\mathrm{D}} - \mathbf{1}\right)$. Due to the assumption of uniaxial compression with unrestricted lateral deformation, all tensors have diagonal form. In this context, the invariants of the *right Cauchy-Green tensor* take the form

$$I_C = \mathrm{tr}(\boldsymbol{C}^{1\mathrm{D}}) = \frac{2}{\lambda^{1\mathrm{D}}} + \left(\lambda^{1\mathrm{D}}\right)^2 \tag{5.33}$$

$$\frac{\partial I_C}{\partial \lambda^{1\mathrm{D}}} = 2\lambda^{1\mathrm{D}} - \frac{2}{\left(\lambda^{1\mathrm{D}}\right)^2} \tag{5.34}$$

$$II_C = \frac{1}{2}\left(\mathrm{tr}\left(\boldsymbol{C}^{1\mathrm{D}}\right)^2 - \mathrm{tr}\left(\left(\boldsymbol{C}^{1\mathrm{D}}\right)^2\right)\right) = \frac{1}{(\lambda^{1\mathrm{D}})^2} + 2\lambda^{1\mathrm{D}} \tag{5.35}$$

$$\frac{\partial II_C}{\partial \lambda^{1\mathrm{D}}} = 2 - \frac{2}{(\lambda^{1\mathrm{D}})^3} \tag{5.36}$$

$$III_C = \det\left(\boldsymbol{C}^{1\mathrm{D}}\right) \stackrel{!}{=} 1. \tag{5.37}$$

The uniaxial form of these invariants is presented here in order to allow for a shorter notation of the evaluation of different material models later on. The derivation of the constitutive contact model with respect to the penetration (5.29) can then be separated into

$$\frac{\partial \Psi_C}{\partial \bar{d}_N} = \left(\frac{\partial \Psi_C}{\partial I_C}\frac{\partial I_C}{\partial \lambda^{1\mathrm{D}}} + \frac{\partial \Psi_C}{\partial II_C}\frac{\partial II_C}{\partial \lambda^{1\mathrm{D}}}\right)\frac{\partial \lambda^{1\mathrm{D}}}{\partial \bar{d}_N}. \tag{5.38}$$

For the computation of mechanical power and the integration of material history the equivalent material velocity gradient

$$\dot{\boldsymbol{F}}^{1\mathrm{D}} = \frac{\mathrm{d}\boldsymbol{F}^{1\mathrm{D}}}{\mathrm{d}t} \approx \frac{\Delta \boldsymbol{F}^{1\mathrm{D}}}{\Delta t} \tag{5.39}$$

and its time discrete approximation (second term) are defined. Its normal projection is the equivalent normal stretch rate of the assumed uniaxial compression test

$$\dot{\lambda}^{1\mathrm{D}} = \boldsymbol{N}^{\mathrm{T}} \cdot \dot{\boldsymbol{F}}^{1\mathrm{D}} \cdot \boldsymbol{N}. \tag{5.40}$$

Additionally, the rate of the equivalent *Green-Lagrange strain* is defined as

$$\dot{\boldsymbol{E}}^{1\mathrm{D}} = \frac{1}{2}\left(\left(\dot{\boldsymbol{F}}^{1\mathrm{D}}\right)^{\mathrm{T}} \cdot \boldsymbol{F}^{1\mathrm{D}} + \left(\boldsymbol{F}^{1\mathrm{D}}\right)^{\mathrm{T}} \cdot \dot{\boldsymbol{F}}^{1\mathrm{D}}\right), \tag{5.41}$$

which is required to calculate the evolution of the internal strain-like variables.

The postulated equality of external mechanical power in the mesoscale volume and on the macroscale interface

$$c_{\dot{\lambda}}\left(\bar{d}_N\right)\boldsymbol{P}^{1\mathrm{D}} : \dot{\boldsymbol{F}}^{1\mathrm{D}} = c_{\dot{\lambda}}\left(\bar{d}_N\right)P^{1\mathrm{D}}\dot{\lambda}^{1\mathrm{D}} \stackrel{!}{=} \left\langle \boldsymbol{P} : \dot{\boldsymbol{F}} \right\rangle \tag{5.42}$$

in conjunction with the exact representation of the nominal contact pressure $P^{1\mathrm{D}} \stackrel{!}{=} \bar{P}$ result in the practical necessity to introduce a penetration dependent energy scaling factor

$c_{\dot{\lambda}}\left(\bar{d}_N\right)$ in order to calibrate the stretch velocities

$$c_{\dot{\lambda}}\left(\bar{d}_N\right)\dot{\lambda}^{1\mathrm{D}} \stackrel{!}{=} \frac{\dot{\bar{d}}_N}{h_0}. \tag{5.43}$$

This results from the incapability of the applied boundary conditions to fulfill the average work criterion (5.12). In time discrete simulations this scaling can be evaluated by

$$c_{\dot{\lambda}}\left(\bar{d}_N\right) = \frac{\Delta\bar{d}_N}{\Delta\lambda^{1\mathrm{D}} h_0}. \tag{5.44}$$

Evaluation of contact pressure

According to (5.29), the contact pressure is calculated using an arbitrary incompressible material. For this case, the equivalent *first Piola-Kirchhoff stress tensor* is defined as

$$\boldsymbol{P}^{1\mathrm{D}} = -p_h^{1\mathrm{D}}\left(\boldsymbol{F}^{1\mathrm{D}}\right)^{-\mathrm{T}} + \frac{\partial\Psi\left(\boldsymbol{F}^{1\mathrm{D}}, \Theta, \boldsymbol{\alpha}_{\mathrm{v}}^{1\mathrm{D}(i)}\right)}{\partial\boldsymbol{F}^{1\mathrm{D}}}, \tag{5.45}$$

in which p_h is the hydrostatic pressure, see [Holzapfel, 2000]. In the context of continuum mechanics this internal pressure is either calculated by using a *Lagrangian multiplier*, or approximated with a penalty function, see section 3.2. In the uniaxial case, the absence of lateral tractions

$$\boldsymbol{A}_i^{\mathrm{T}} \cdot \boldsymbol{P}^{1\mathrm{D}} \cdot \boldsymbol{N} = 0, \tag{5.46}$$

can be exploited in order to evaluate the scalar internal hydrostatic pressure

$$p_h^{1\mathrm{D}} = \boldsymbol{A}_i^{\mathrm{T}} \cdot \frac{\partial\Psi}{\partial\boldsymbol{F}^{1\mathrm{D}}} \cdot \left(\boldsymbol{F}^{1\mathrm{D}}\right)^{\mathrm{T}} \cdot \boldsymbol{N}, \tag{5.47}$$

using an arbitrary tangent vector $\boldsymbol{A}_i$. As an example, the calculation of the nominal pressure in terms of the *Neo-Hooke model* (3.18) yields

$$P^{1\mathrm{D}} = \mu^{1\mathrm{D}}\left(\lambda^{1\mathrm{D}} - \frac{1}{\left(\lambda^{1\mathrm{D}}\right)^2}\right), \tag{5.48}$$

where the equivalent shear modulus $\mu^{1\mathrm{D}} = c_{\mathrm{el}}\mu$ is the shear modulus of the mesoscale model μ scaled by a constant factor c_{el}.

The incompressible *extended tube model* (3.20) is evaluated by

$$\begin{aligned} P^{1\mathrm{D}} &= G_c^{1\mathrm{D}}\left\{\frac{1-\delta^2}{(1-\delta^2(I_C-3))^2} - \frac{\delta^2}{1-\delta^2(I_C-3)}\right\}\left(\lambda^{1\mathrm{D}} - \frac{1}{(\lambda^{1\mathrm{D}})^2}\right) \\ &+ \frac{2G_e^{1\mathrm{D}}}{\beta(\lambda^{1\mathrm{D}})^{\beta+1}}\left(\left(\lambda^{1\mathrm{D}}\right)^{\frac{3\beta}{2}} - 1\right), \end{aligned} \tag{5.49}$$

where $G_c^{1\mathrm{D}} = c_{\mathrm{el}}G_c$ is the equivalent chemical shear modulus, $G_e^{1\mathrm{D}} = c_{\mathrm{el}}G_e$ is the equivalent topological shear modulus, and both are scaled by the same factor as identified for the Neo-Hooke model c_{el}.

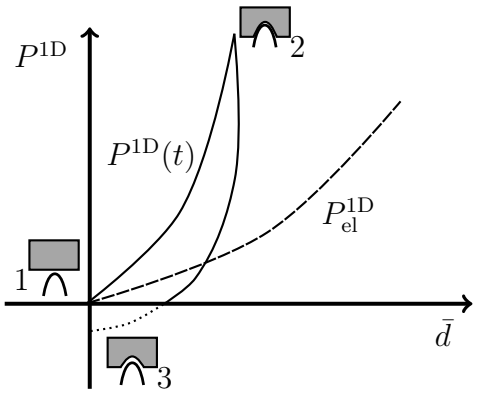

Figure 5.2: Schematic diagram: Elastic P^{1D}_{el} and viscoelastic $P^{1D}(t)$ response of the constitutive contact model. The gray tread blocks illustrate the basic contact states: 1-no contact; 2-penetration; 3-separation.

For the calculation of viscoelastic response the evolution of the internal variables need to be integrated in order to evaluate the resulting overstresses. Due to the additive composition of the mesoscale constitutive material model

$$\Psi_C = W_C + \sum_i \Upsilon_C^{(i)}, \tag{5.50}$$

from an elastic part W_C and a number of viscoelastic parts $\Upsilon_C^{(i)}$, the different contributions of pressure response can be evaluated separately

$$\begin{aligned} P^{1D}\left(\lambda^{1D}, \Theta, \boldsymbol{\alpha}_v^{1D(i)}\right) &= -\left(p_h^{el} + p_h^{v}\right)\lambda^{1D} + \boldsymbol{N}^T \cdot \frac{\partial \Psi\left(\boldsymbol{F}^{1D}, \Theta, \boldsymbol{\alpha}_v^{1D(i)}\right)}{\partial \boldsymbol{F}^{1D}} \cdot \boldsymbol{N} \geq 0 \\ &= \max\left[0, P_{el}^{1D}\left(\lambda^{1D}, \Theta\right) + P_v^{1D}\left(\lambda^{1D}, \Theta, \boldsymbol{\alpha}_v^{1D(i)}\right)\right]. \end{aligned} \tag{5.51}$$

A sketch of the resulting contact pressure-penetration curve of a displacement driven experiment is shown in Figure 5.2. Due to the viscoelastic behavior, the material does not fully relax in the unloading phase of the load cycle $P^{1D}(t)$. For this reason, the tread looses its contact to the road at a penetration $\bar{d}_N > 0$ (with $\lambda^{1D}\left(\bar{d}_N\right) < 1$) resulting in no contact pressure.

As the equivalent deformation is assumed to be a uniaxial compression, the internal algorithmic variable describing the elastic strain of the $i-$th *Maxwell-element*

$$\boldsymbol{H}_{el}^{1D(i)} = \begin{bmatrix} h_T^{1D(i)} & 0 & 0 \\ 0 & h_T^{1D(i)} & 0 \\ 0 & 0 & h_N^{1D(i)} \end{bmatrix} \text{ with } \boldsymbol{E}^{1D} = \boldsymbol{H}_{el}^{1D(i)} + \boldsymbol{\alpha}_v^{1D(i)}, \tag{5.52}$$

which was introduced in (3.47) has a diagonal form and depends on two scalar values

$$\begin{aligned} h_{T\,n+1}^{1\mathrm{D}(i)} &= \exp\left(-\frac{\Delta t}{\tau_i}\right) h_{T\,n}^{1\mathrm{D}(i)} + \exp\left(-\frac{\Delta t}{2\tau_i}\right)\left(0.5\Delta\frac{1}{\lambda^{1\mathrm{D}}}\right) \\ h_{N\,n+1}^{1\mathrm{D}(i)} &= \exp\left(-\frac{\Delta t}{\tau_i}\right) h_{N\,n}^{1\mathrm{D}(i)} + \exp\left(-\frac{\Delta t}{2\tau_i}\right)\left(0.5\Delta\left(\lambda^{1\mathrm{D}}\right)^2\right). \end{aligned} \tag{5.53}$$

In this definition, $h_N^{1\mathrm{D}(i)}$ describes the elastic strain in normal direction, and $h_T^{1\mathrm{D}(i)}$ the elastic strain in tangential direction of the $i-$th *Maxwell-element*. The possibility to integrate a set of evolution equations depicting the material history evolution in the homogenized contact layer directly on the macroscale is a major advantage in compared to FE^2-schemes. In FE^2-schemes the material history evolution is calculated within the coupled microscale models, requiring a much larger computational effort.

The viscoelastic contribution to the equivalent nominal pressure results in

$$P_{\mathrm{v}}^{1\mathrm{D}} = 2\sum_i \mu_{\mathrm{v}}^{1\mathrm{D}(i)}\left(\lambda^{1\mathrm{D}} h_{N\,n+1}^{1\mathrm{D}(i)} - h_{T\,n+1}^{1\mathrm{D}(i)}\frac{1}{\left(\lambda^{1\mathrm{D}}\right)^2}\right). \tag{5.54}$$

Due to the larger elastic strains in the *Maxwell-elements*, the equivalent shear modulus of the $i-$th *Maxwell-element* $\mu_{\mathrm{v}}^{1\mathrm{D}(i)} = c_{\mathrm{v}}\mu_{\mathrm{v}}^{(i)}$ is scaled by a factor c_{v}. In order to keep the relaxation time constant $\tau_{\mathrm{v}}^{(i)} = \frac{\eta_{\mathrm{v}}^{1\mathrm{D}(i)}}{2\mu_{\mathrm{v}}^{1\mathrm{D}(i)}}$, the viscosity $\eta_{\mathrm{v}}^{1\mathrm{D}(i)} = c_{\mathrm{v}}\eta_{\mathrm{v}}^{(i)}$ of the $i-$th *Maxwell-element* is also scaled.

Finally, the dissipation of mechnical energy in the dashpots is calculated, presented in short notation as

$$\mathcal{D}_{\mathrm{int}}^{1\mathrm{D}}\left(\lambda^{1\mathrm{D}}, \Theta, \boldsymbol{\alpha}_{\mathrm{v}}^{1\mathrm{D}(i)}\right) = 4c_{\dot{\lambda}}\left(\bar{d}_N\right)\sum_i \frac{\left(\mu_{\mathrm{v}}^{1\mathrm{D}(i)}\right)^2}{\eta_{\mathrm{v}}^{1\mathrm{D}(i)}}\boldsymbol{H}_{\mathrm{el}}^{1\mathrm{D}(i)} : \boldsymbol{H}_{\mathrm{el}}^{1\mathrm{D}(i)}, \tag{5.55}$$

which needs to be scaled by the energy scaling factor (5.43) in order to obtain consistency of energy at the interface.

Summary of the homogenization approach

1. Calculation of the thermo-viscoelastic mesoscale contact interaction
2. Evaluation of the equivalent stretch-penetration relation (5.31)
3. Identification of the material scaling parameters c_{el} and c_{visco}
4. Evaluation of contact pressure $P^{1\mathrm{D}}\left(\lambda^{1\mathrm{D}}, \Theta, \boldsymbol{\alpha}_{\mathrm{v}}^{1\mathrm{D}(i)}\right)$ (5.51) and dissipation $\mathcal{D}_{\mathrm{int}}^{1\mathrm{D}}\left(\lambda^{1\mathrm{D}}, \Theta, \boldsymbol{\alpha}_{\mathrm{v}}^{1\mathrm{D}(i)}\right)$ (5.55) in terms of the bulk material

Note that the application of this constitutive contact model requires a C^1-continuous analytic approximation of the stretch-penetration relation, which can be realized e.g. by polynomial least-squares fitting.

5.2 Random rough surface contact problem

The interaction of a single tread block with the rough road surface can be regarded as a random experiment. Each time the tread block impacts onto the road it touches a new patch with random asperity height and shape distribution, which results in a random displacement field and random reaction forces. Due to the thermo-viscoelastic properties of the tread rubber, the resulting reaction forces strongly depend on the penetration velocity. Its influence is equivalent to the loading frequency in uniaxial testing, see section 3.5. The material parameters are considered deterministic in this thesis and therefore each impact can be described as a deterministic process. For the description of the steady state rolling motion, oscillations caused by single impacts hardly affect the result and therefore, the focus is put on the time-averaged response in the present study. This assumption simplifies the problem to a random elliptic variational inequality, the *random Signorini problem* see [Ganguly and Wadhwa, 1997; Kornhuber et al., 2014].

In the classical *Signorini problem*, the balance of linear momentum (2.40) is solved under the non-penetration condition of a parameterized surface $x_m(\boldsymbol{\xi})$ as

$$\begin{aligned} \mathcal{G}_{\boldsymbol{u}}\left(\boldsymbol{u}, \delta\boldsymbol{u}\right) \stackrel{!}{=} 0 \quad &= \int_{\mathcal{B}} \mathbb{E}\left[\boldsymbol{S} : \delta\boldsymbol{E} + \varrho\boldsymbol{b} \cdot \delta\boldsymbol{u}\right] \, \mathrm{d}V - \int_{\partial_t\mathcal{B}} \mathbb{E}\left[\boldsymbol{T} \cdot \delta\boldsymbol{u}\right] \, \mathrm{d}A \\ &- \int_{\partial_c\mathcal{B}} \mathbb{E}\left[\boldsymbol{T}_c \cdot \delta(\bar{\boldsymbol{x}}_m(\boldsymbol{\xi}) - \boldsymbol{x}_s)\right] \, \mathrm{d}A. \end{aligned} \tag{5.56}$$

Herein, $\boldsymbol{T}$ are the applied external nominal surface tractions, $\boldsymbol{T}_c$ denotes the nominal contact tractions and the closest point projection fulfills $(\bar{\boldsymbol{x}}_m\left(\boldsymbol{\xi}\right) - \boldsymbol{x}_s) \cdot \bar{\boldsymbol{n}}\left(\boldsymbol{\xi}\right) = \|\bar{\boldsymbol{x}}_m\left(\boldsymbol{\xi}\right) - \boldsymbol{x}_s\|$.

In the present study, the rough road surface is modeled by a spectral representation of a measured road profile. The computation of this analytical surface description is specified in the next section. As the tread block is smaller than the characteristic length scale of the road surface, a random impact position is introduced in order to achieve the average contact behavior. The impact position $\boldsymbol{\xi} = \boldsymbol{\xi}_0 - \boldsymbol{\zeta}$ is modeled by a uniformly randomly distributed offset vector (random variable) $\boldsymbol{\zeta} \in \boldsymbol{Z}$, which is an element of the sample space $\boldsymbol{Z}$. With this definition the solution $\boldsymbol{u}(\boldsymbol{\xi})$ of the *Signorini problem* becomes random as well. The mathematical formalism of this problem can be found in [Ganguly and Wadhwa, 1997; Kornhuber et al., 2014].

The main interest of this computation lies in the average solution

$$\bar{\boldsymbol{u}}\left(\bar{d}_N(t), \Theta\right) = \int_{\boldsymbol{Z}} \left(\bar{d}_N(t), \Theta, \boldsymbol{\zeta}\right) \mathrm{d}\boldsymbol{\zeta} \tag{5.57}$$

across the sample space $\boldsymbol{Z}$ as a function of the current penetration $\bar{d}_N(t)$ which prescribes a penetration rate $\dot{\bar{d}}_N$, and the temperature Θ. Here, penetration means the prescribed

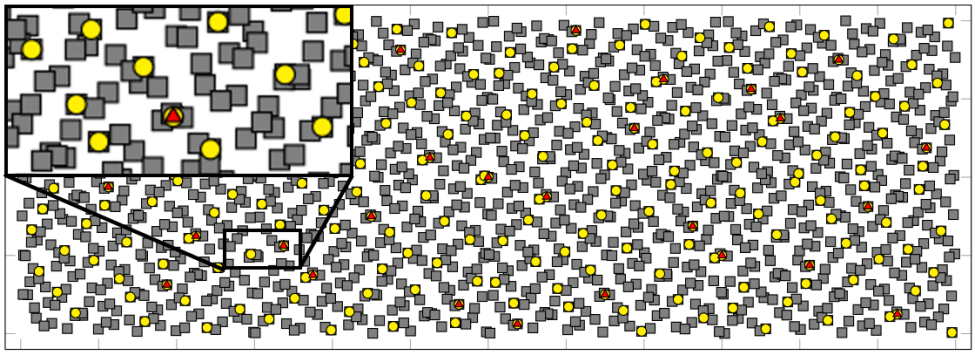

Figure 5.3: Evaluation of the Sobol sequence for the two-dimensional phase shift vector in the contact domain.

violation of the plane that is defined by the highest asperity below the tread block. The frequency dependence of the solution arises from the viscoelastic properties of the material. Based on this average deformation state, the average nominal contact pressure response can be defined as a reaction at the *Dirichlet boundary* $\partial_{\boldsymbol{u}}\mathcal{B}$

$$\bar{P}\left(\bar{d}_N(t),\Theta\right) = \frac{1}{A}\int\limits_{\partial_{\boldsymbol{u}}\mathcal{B}} P\left[\bar{\boldsymbol{u}}\left(\bar{d}_N(t),\Theta\right)\right]\,\mathrm{d}A, \tag{5.58}$$

Finally, the volume average internal dissipation is calculated via

$$\bar{\mathcal{D}}\left(\bar{d}_N(t),\Theta\right) = \frac{1}{V}\int\limits_{\mathcal{B}} \mathcal{D}\left[\bar{\boldsymbol{u}}\left(\bar{d}_N(t),\Theta\right)\right]\,\mathrm{d}V. \tag{5.59}$$

In this thesis, the *Quasi Monte Carlo method* is applied in order to evaluate the parametric integral (5.57). With this method, the samples of the uniformly distributed random offset vector are generated from a low discrepancy sequence, so that the parametric space is covered at improved computational effort. In the present study the *Sobol-sequence* is applied for sample generation. The generator algorithm of this sequence is available as open-source code as well as in commercial environments such as *Matlab*®. It hands back a series of uniformely distributed nested samples, e.g. the two-dimensional example sequence illustrated in Figure 5.3. Here, the first few samples (red triangles) are already distributed across the entire parametric domain, and following samples (yellow circles and gray squares) successively close the empty spaces in between the previous objects without overlapping. This characteristic is very sophisticated for numerical studies as it allows for a truncation of the simulation when the average value has reached convergence $\Delta\bar{\boldsymbol{u}} \leq \epsilon$. Also, it allows for the generation of additional samples if this threshold ϵ (accuracy of the mean value) has not yet been reached.

5.3 Statistical characterization of rough road surfaces

The solution of the random Signorini problem requires a description of the rough road surface. In order to allow for an exact evaluation of the contact kinematics and to calculate a consistent stiffness matrix, a C^2-continuous surface representation is required in case of unilateral contact. In this thesis, a C^∞-continuous spectral representation was chosen, which can be obtained by the *discrete Fourier transform* (DFT). The raw data is thereby transformed into a power spectrum representing the measured data by a set of cosine functions. This allows for an efficient statistical analysis as well as for filtering, storage, and evaluation of surface points by an inverse transformation. The procedure of its construction is briefly described in the following subsection. Alternatively, the measured data could have been discretized with spline functions, or the height profile of the surface could have been generated as realization of a random field description of the rough surface with prescribed stochastic properties. The definition of the most relevant quantities and the evaluation of the measured smooth and rough road profiles and their filtered representations are presented in the second part of this section.

5.3.1 Continuous representation

In the context of contact simulations, a continuous analytic description of measured surface data that enables a continuous evaluation of surfaces derivatives is desirable. This fact allows for a calculation of a continuous normal vector field, which is beneficial for the convergence of the contact constraint enforcement algorithm. In this study, an analytic representation is obtained by DFT, for which the discrete spectral power density is calculated via

$$Z\left(f_x^{(u)}, f_y^{(v)}\right) = \frac{1}{M\,N} \sum_{k=0}^{M-1} \sum_{l=0}^{N-1} z\left(x^{(k)}, y^{(l)}\right) e^{-i2\pi\left(\frac{uk}{M}+\frac{vl}{N}\right)} \tag{5.60}$$

where $k, u \in [0, M-1]$ and $l, v \in [0, N-1]$ define a discrete set of frequencies. The upper bound of the resolved frequencies is given by the so-called *Niquist frequency* $f_N = \frac{1}{2\Delta l}$, where Δl is the spatial sampling rate of the measurement device. The surface points $\hat{z}\,(x, y) \in C^\infty$ can then be calculated by inverse DFT

$$\hat{z}\,(x, y) = \sum_{k=0}^{M-1} \sum_{l=0}^{N-1} |Z\,(k, l)\,| \cos\left(2\pi\left(f_x^k x + f_y^l y\right) + \phi_{\text{off}}^{(k,l)}\right), \tag{5.61}$$

using the spatial frequencies f_x and f_y, the absolute amplitudes $|Z\,(k, l)\,|$ and offset phase angles ϕ_{off}, which are the imaginary parts of $\log(Z)$. Note that this evaluation is costly for surfaces with a large frequency spectrum and needs to be computed successively to

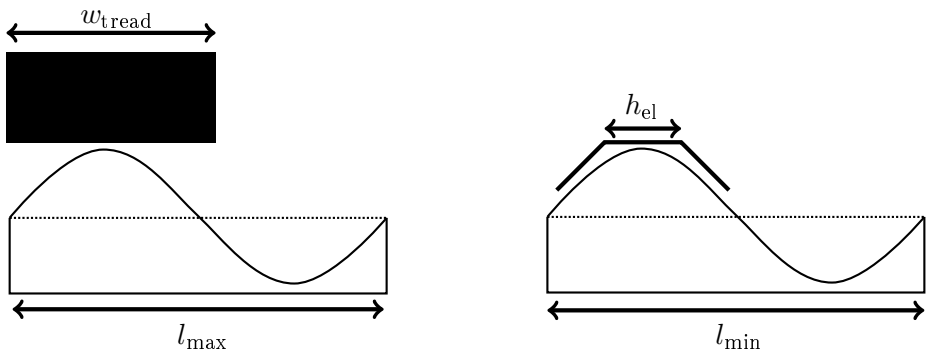

(a) Lower cut-off $1/l_{\text{max}}$ (b) Upper cut-off $1/l_{\text{min}}$

Figure 5.4: Definition of cut-off frequencies in the tread-road interaction simulations, based on the tread width w_{tread} and the contact element size h_{el}.

determine the closest point in the contact algorithm, see section 4.1. Especially for detailed tread models these surface evaluations may by far exceed computational costs of solving the resulting stiffness matrix.

In order to reduce the size of the frequency spectrum, a bandpass filter is applied that removes spatial frequencies without effective contribution to the contact interaction so that $f_x, f_y \in [f_{\text{low}}, f_{\text{high}}]$. Here, the lower cut-off frequency $f_{\text{low}} = \frac{1}{l_{\text{max}}}$ is defined by the maximum wavelength $l_{\text{max}} = 2w_{\text{tread}}$ and the width of the tread block w_{tread}, all larger wavelengths are regarded as waviness. The upper cut-off frequency $f_{\text{high}} = \frac{1}{l_{\text{min}}}$ is defined by the minimal wave length $l_{\text{min}} = 6h_{\text{el}}$ and the contact element size h_{el}, which ensures that the spatial frequencies can be detected by the mesh resolution. The amplitudes of frequencies $f > f_{\text{high}}$ are small and therefore assumed to have no significant contribution to rolling resistance, as will be shown in subsection 5.4.3.

5.3.2 Statistical characterization of rough road surfaces

The comparison of different measured road profiles requires their statistical characterization, which is defined in the DIN EN ISO norms:

- 4287: Definitions and characteristic quantities of surface properties: linear
- 4288: Methods to determine surface properties
- 13473: Road surface textures
- 11562: Definition of admissible filter operations
- 13565: Surfaces having stratified functional properties

- 25178: Definitions and characteristic quantities of surface properties: areal

The surface characteristics are evaluated for the measured height profile $z(x, y)$with methods known from digital image processing, see e.g. [Gonzalez et al., 2003]. In this context, the transformation of the raw data into a power spectrum by means of the DFT allows for the application of efficient algorithms.

Following [Brinkmeier, 2007], the surface amplitude $a(x, y) = z(x, y) - m(x, y)$ is introduced first, which describes all surface heights as variations about the mean plane $m(x, y)$ of the measured $N_x \times N_y$ points. In the following, a shorthand notation is used to describe discrete local values by $\bullet_{ij} = \bullet(x_i, y_j)$. With these definitions, the basic unbiased measures for the characterization of the height distribution are the first four discrete statistical moments of the amplitude:

1.	Mean amplitude	$\bar{a}$	$= \frac{1}{N_x N_y} \sum_{i=1}^{N_x} \sum_{j=1}^{N_y} a_{ij}$
2.	Standard deviation	σ	$= \sqrt{\frac{1}{N_x N_y} \sum_{i=1}^{N_x} \sum_{j=1}^{N_y} a_{ij}^2}$
3.	Skewness	S	$= \frac{1}{N_x N_y \sigma^3} \sum_{i=1}^{N_x} \sum_{j=1}^{N_y} a_{ij}^3$
4.	Kurtosis	K	$= \frac{1}{N_x N_y \sigma^4} \sum_{i=1}^{N_x} \sum_{j=1}^{N_y} a_{ij}^4$

As the distribution has been centered $\bar{a} = 0$, the mean absolute amplitude

$$\bar{a}_{\text{abs}} = \frac{1}{N_x N_y} \sum_{i=1}^{N_x} \sum_{j=1}^{N_y} |a_{ij}| \tag{5.62}$$

is introduced as the most common measure for surface roughness about the mean plane. Further common quantities are so-called hybrid parameters, e.g. the average slope

$$S_{\Delta q} = \sqrt{\frac{\sum_{i=1}^{N_x} \sum_{j=1}^{N_y} q_{ij}}{(N_x - 1)(N_y - 1)}}, \text{ with } q_{ij} = \left(\frac{a_{(i+1)j} - a_{ij}}{\Delta x} \right)^2 + \left(\frac{a_{i(j+1)} - a_{ij}}{\Delta y} \right)^2 \tag{5.63}$$

and the developed area ratio

$$S_{\Delta A} = \frac{A - A_0}{A_0} \text{ with } A = \sum_{i=1}^{N_x} \sum_{j=1}^{N_y} A_{i,j}. \tag{5.64}$$

It defines the relation of nominal surface area A_0 and real surface area A, see DIN EN ISO 25178. Here, the area increments $A_{i,j}$ can be obtained e.g. by surface tessellation.

A valuable insight into the height distribution of asperities can be obtained by the *Abbott-Firestone* or bearing-area curve, which describes the increase in real contact area over penetration depth, see Figure 5.7. Mathematically, this curve is the cumulative distribution function of the asperity amplitudes that are involved in the contact interaction. Additionally, the roughness can also be described as regional or local quantity, which

results in the formulations of uniformity and entropy of surface heights. Other common measures for texture descriptions are spectral measures, moment invariants, and principal components. For further details, the reader is referred to the norms cited above.

An important measure to check the surface randomness is the autocorrelation function

$$A_f(\boldsymbol{\xi}) = \frac{1}{A}\int_A a(\boldsymbol{x}_0)a(\boldsymbol{x}_0+\boldsymbol{\xi})\mathrm{d}x_0\mathrm{d}y_0, \tag{5.65}$$

which describes the correlation of surface heights with respect to the reference point $\boldsymbol{x}_0$ under a certain offset $\boldsymbol{\xi}$. At zero offset $A_f(\mathbf{0})$, the function has a maximum, which is the global maximum for non-periodic surfaces. If the function contains other local maximums representing offsets with high correlations of surface heights, a possible periodicity is indicated. In case of periodic surfaces, the function takes its maximal and minimal values at offsets that coincide with the wavelength. The indication of a periodic surface allows for the definition of a representative surface element.

5.3.3 Comparison of the measured and filtered road profiles

In this thesis, the rolling resistance contribution of a smooth and a rough asphalt road surface are compared. Both optically measured surfaces (sized 400x240 mm) served for the evaluation of tire rolling noise radiation in [Brinkmeier, 2007]. The evaluation of their autocorrelation functions yields that both surfaces are random, and therefore a stochastic homogenization using *Monte Carlo simulations* is performed to evaluate the average tread-road interaction in subsection 5.4.3. In order to reduce the numerical effort of the surface projections within these contact calculations, the frequency spectra for both surfaces were filtered by a bandpass filter, which severely reduced the number of frequencies to be evaluated. This filtering also reduces the oscillation of surface normals, which is beneficial for the convergence of the contact constraint enforcement algorithm. In this thesis, the bounds of the bandpass filter were chosen to be [1/120, 1/4] 1/mm for the smooth surface and [1/120, 1/5] 1/mm for the rough surface. In the following the surface characteristics of the raw data are compared to those of the filtered spectral representation.

The smooth asphalt surface

In Figure 5.5, the measured smooth surface (a), its bandpass filtered representation (b) and the difference plot (c) are illustrated. The removal of low-frequency contributions hardly effects the difference area, as the measured surface was already very smooth. Only high-frequency oscillations with relatively small amplitudes are visible. This results in the optically very good representation of the mesoscopic surface characteristics. In contrast to that the comparison of the statistical values given in Table 5.1 points out a severe impact of the filtering, especially for the higher order moments S and K.

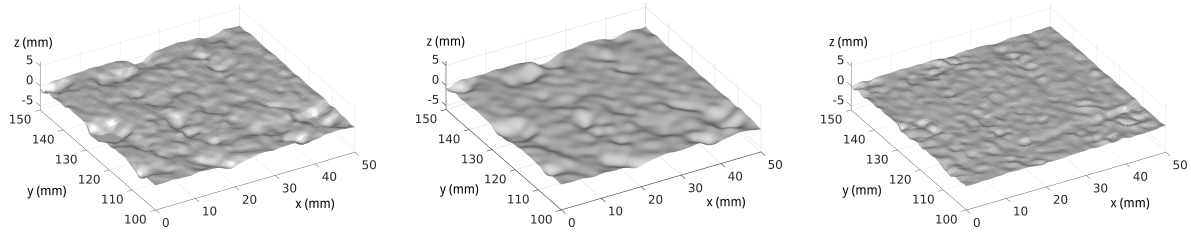

(a) Measured surface (b) Filtered surface (c) Δz - plot

Figure 5.5: Comparison of the unfiltered (a) with the filtered (b) smooth surface representation by inverse DFT and height difference of both surfaces (c).

	$\bar{a}_{\text{abs}}$	σ	S	K	$S_{\Delta q}$	$S_{\Delta A}$
Measurement	0.383 mm	0.489 mm	-0.443	3.423	0.309	4.375%
Bandpass filtered	0.262 mm	0.355 mm	-1.079	5.180	0.261	3.256%
Absolute percentage Error	32%	27%	144%	51%	16%	26%

Table 5.1: Statistical characterization surface of the smooth asphalt and the influence of the filtering upon it.

The rough asphalt surface

The rough surface illustrated in Figure 5.6 (a)-(c) clearly reveals that the removal of low-frequency contributions causes a waviness in the difference plot (c), which is superimposed by high-frequency oscillations. Nonetheless, the comparison of the filtered and the unfiltered surface representations as well as the statistical values given in Table 5.2 shows an acceptable preservation of the mesoscopic surface characteristics. Note that the amplitudes of the rough surface almost have a *Gaussian distribution*, which is centered around the mean value, and for this reason, the skewness is zero and the kurtosis equals 3.

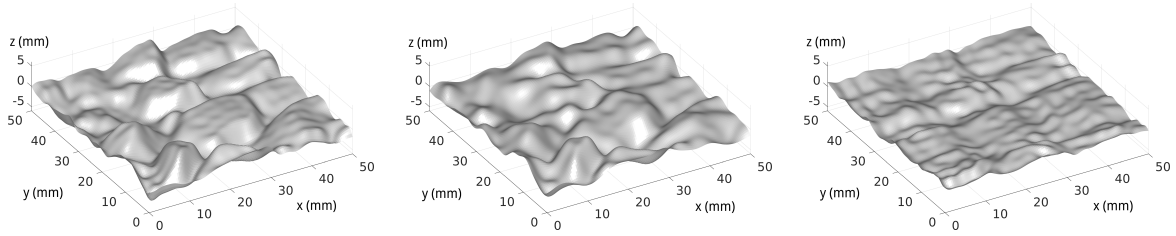

(a) Measured surface (b) Filtered surface (c) Δz - plot

Figure 5.6: Comparison of the unfiltered (a) with the filtered (b) smooth surface representation by inverse DFT and height difference of both surfaces (c).

	$\bar{a}_{\text{abs}}$	σ	S	K	$S_{\Delta q}$	$S_{\Delta A}$
Measurement	1.409 mm	1.726 mm	0.109	2.585	0.766	22.781%
Bandpass filtered	1.173 mm	1.452 mm	0.085	2.746	0.681	19.183%
Absolute percentage Error	17%	16%	22%	6%	11%	16%

Table 5.2: Statistical characterization surface of the rough asphalt and the influence of the filtering upon it.

Comparison of both surfaces

The comparison of the bearing area curves displayed in Figure 5.7 reveals that the increase in contact area with penetration depth is much smaller on the rough asphalt surface than on the smooth asphalt surface, which results in a smaller stiffness of the tread-road contact. Consequently, the same applied load results in larger penetrations of the tread block by the surface asperities, which causes larger local stretches, and finally results in a higher rolling resistance than on the smooth asphalt surface. Furthermore, it can be concluded from the

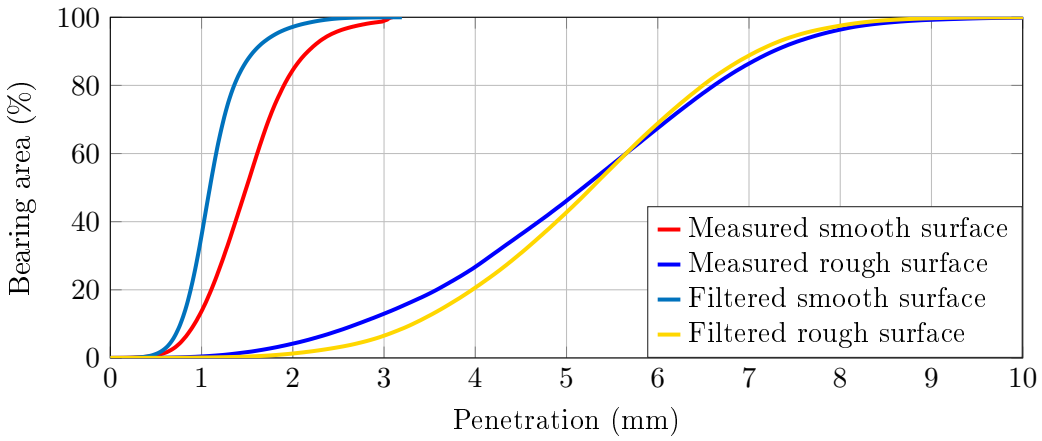

Figure 5.7: Bearing area over penetration for both measured asphalt surfaces and the resulting filtered representations, see Figure 5.5 and Figure 5.6.

comparison of the filtered and the unfiltered bearing area curves that the filtering reduces the fluctuation in surface heights, which results in steeper slopes and therefore in a stiffer contact behavior. This effect can be observed in the results of the convergence study on the reaction forces presented in subsection 5.4.3. Even though the filtering severely changes the surface characteristics, the effect on the reaction-force-penetration-relation is relatively small. The high-frequency small scale asperities basically cause a small offset in the resulting reaction forces. Only the peak values of the local pressures are affected by the bandpass filtering, which are damped out by the volumetric homogenization. This finally justifies the applied filtering approach in order to reduce the numerical effort.

5.4 Numerical examples

The following numerical examples for the homogenization of rough surface contact scenarios prove the consistency of energy of the presented approach. Furthermore, the material parameters of the constitutive contact model are identified in order to enable a representation of the average tread-road interaction. This representation is applied in the rolling resistance simulations of the next chapter. Initially however, the workflow for the homogenization procedure used in the following examples is explained.

5.4.1 Homogenization procedure

The homogenization of the tread behavior first requires the definition of the transition area $\partial\Omega_M$ which separates the macroscale and the mesoscale problem. This distance of this plane to the actual contact region must be sufficiently large, so that local oscillations of the stress field are homogenized in the mesoscale model. In case of the present tread pattern, the transition area was placed at the tread base, where the tread block is connected to the tire structure, see Figure 5.8. According to this definition, the contact interaction of the tread block with the rough surface is calculated with the separated mesoscale (homogenization) model. In these simulations, the tread rubber is described by the thermo-viscoelastic material model in the regime of finite strains (see chapter 3). Here, the quantities of interest are:

1. Average nominal pressure $\bar{P}\left(\bar{d}_N(t), \Theta\right)$
2. Volume average power $\left\langle \mathcal{P}\left(\bar{d}_N(t), \Theta\right)\right\rangle$
3. Volume average dissipation $\left\langle \mathcal{D}\left(\bar{d}_N(t), \Theta\right)\right\rangle$

as functions of the applied macroscopic boundary conditions:

- Partial fixation of lateral displacements at the top nodes, resulting in a unilateral deformation state
- Constant penetration increments $\Delta\bar{d}_N$ (linear increase in displacement) of the top nodes prescribing a constant penetration rate $\dot{\bar{d}}_N$
- Prescribed initial service temperature Θ

The workflow to homogenize a rough surface contact scenario is:

1. Calculate the stochastic average of the elastic response of the mesoscale model
2. Identify fitting polynomials for the stretch-penetration relation $\lambda^{1\mathrm{D}}(\bar{d}_N)$
3. Fit elastic response $P_{\mathrm{el}}^{1\mathrm{D}}(\bar{d}_N, \Theta) = \bar{P}_{\mathrm{el}}(\bar{d}_N, \Theta)$ by scaling factor c_{el}
4. Calculate one viscoelastic realization of a load cycle with the mesoscale model
5. Fit viscoelastic response $P_{\mathrm{visco}}^{1\mathrm{D}}\left(\bar{d}_N(t), \Theta\right) = \bar{P}_{\mathrm{visco}}\left(\bar{d}_N(t), \Theta\right)$ by scaling factor c_{visco}

In this study, the discrete evaluations of the stretch-penetration relation $\lambda^{1\mathrm{D}}(\bar{d}_N)$ obtained in the numerical experiments are fitted with a polynomial function

$$\tilde{\lambda}^{1\mathrm{D}}(\bar{d}_N) = \sum_{i=0}^{N} a_i \left(\bar{d}_N\right)^i . \tag{5.66}$$

The coefficients a_i for this fitting function $\tilde{\lambda}^{1\mathrm{D}}(\bar{d}_N)$ can be calculated by solving a linear least squares approximation

$$\min_{a_i} 0.5 \left| \tilde{\lambda}^{1\mathrm{D}}\left(\bar{d}_N\right) - \lambda^{1\mathrm{D}}\left(\bar{d}_N\right) \right|^2 . \tag{5.67}$$

Note that the evaluation of the constitutive contact model is very sensitive to the stretch. Therefore, a good representation of the contact pressure response requires a high approximation precision for the nonlinear stretch-penetration relation. Here, the proper polynomial order depends on the problem, but higher order polynomials are often necessary. In order to obtain consistent characteristics of the approximated stretch-penetration relation in the interval $[0, h_0]$, the solution is restricted by

$$\tilde{\lambda}^{1\mathrm{D}}(0) \stackrel{!}{=} 1,\ \tilde{\lambda}^{1\mathrm{D}}\left(\bar{d}_N > 0\right) < 1,\ \frac{1}{h_0} \leq \left(\tilde{\lambda}^{1\mathrm{D}}\right)'(\bar{d}_N) \leq 0 \ \forall\ \bar{d}_N \in [0, h_0], \tag{5.68}$$

which ensures that the stretch vanishes at zero penetration $\tilde{\lambda}^{1\mathrm{D}}(0) \stackrel{!}{=} 1$ and always represents a compression. Furthermore, the polynomial approximation needs to be monotonically decreasing in order to obtain a convex potential, which allows for a consistent contact pressure calculation. Though, the slope may not be larger than for flat surface contact. In order to solver the optimization problem (5.67), the target function and the restrictions are rewritten in a matrix notation that can be solved e.g. with the *Matlab*®algorithm *lsqlin*.

5.4.2 Homogenization of single asperity contact

In this first example, the penetration of a tread rubber block by a single spherical asperity is studied. The tread block has a size of 30x30x20 mm, its bedding has a height of 8 mm and the asperity diameter is 8 mm. The aim of this example is to identify the dominating effects in tread-road interaction and to illustrate the homogenization procedure. Furthermore, the accuracy of the representation of this contact scenario in terms of the homogenized constitutive contact model is validated in this investigation.

The reference solution for the contact interaction of the bedded tread on the sphere is obtained by computing a full scale finite element model, which is depicted in Figure 5.8 (a). The model is discretized with 1204 20-node brick elements (5415 nodes) with a spatial resolution of 1.6 x 1.6 mm above the contact zone. In this figure, the green tetrahedrons mark the nodal *Dirichlet boundary conditions* on the top surface. The application of the *Dirichlet boundary* is motivated by the steel belt, which is situated above the tread layer and assumed to be rigid. This assumption is based on the fact that the steel belt has

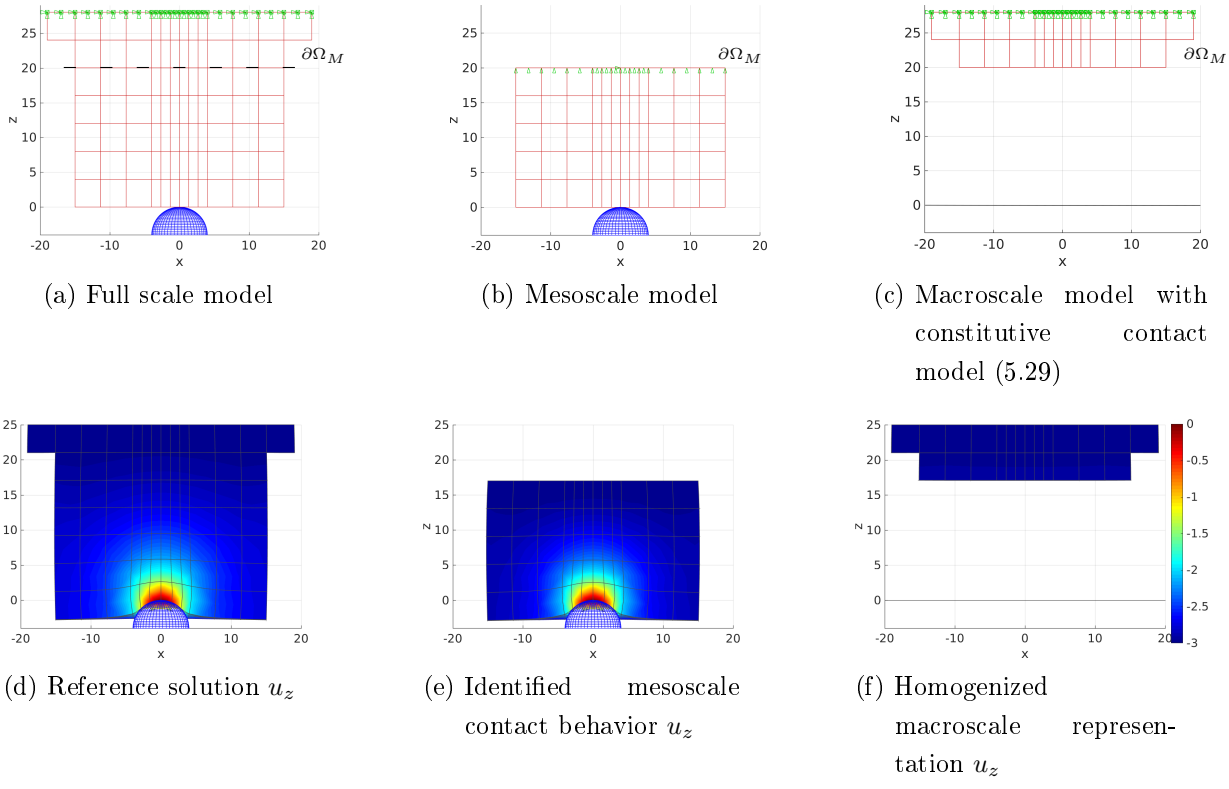

(a) Full scale model

(b) Mesoscale model

(c) Macroscale model with constitutive contact model (5.29)

(d) Reference solution u_z

(e) Identified mesoscale contact behavior u_z

(f) Homogenized macroscale representation u_z

Figure 5.8: (a)-(c) Tread block model (size 30x30x20 mm) with bedding (height: 8 mm) on spherical asperity (diameter = 8 mm). Green tetrahedrons represent *Dirichlet boundary conditions*. (d)-(e) Deformations u_z at the maximum prescribed penetration d_N.

Elastic properties		**Viscoelastic properties**	
Chemical shear modulus	$G_c = 3.0\ \mathrm{N/(mm^2)}$	Shear modulus	$\mu_{\mathrm{v}}^1 = 1\ \mathrm{N/(mm^2)}$
Topological shear modulus	$G_e = 1.3\ \mathrm{N/(mm^2)}$	Viscosity	$\eta_{\mathrm{v}}^1 = 0.02\ \mathrm{Ns/(mm^2)}$
Stretch restriction	$\delta = 0.3$	Relaxation time	$\tau_{\mathrm{v}}^1 = 0.01$ s
Poisson's ratio	$\nu = 0.49$	Thermal softening	$\xi_{\mathrm{v}}^1 = 10$
Thermal behavior			
Reference temperature	$\Theta_0 = 293$ K	Heat capacity	$\varrho_0 c_{p0} = 1.7385\ \mathrm{N/(mm^2\,K)}$
Thermal expansion	$\alpha_{\Theta 0} = 0.000222$ 1/K		$k_{cp} = 0.0024\ \mathrm{J/\ (kg\,K^2)}$
Density	$\varrho_0 = 800\ \mathrm{kg/m^3}$	Thermal conductivity	$k_{\Theta 0} = 0.2595 \cdot 10^{-4}$ 1/K
			$\omega_k = 0.004$ 1/K

Table 5.3: Material parameters for the tread material in the *extended tube model* (3.20).

much larger material stiffness than the tread block. The tread rubber is represented by the thermo-viscoelastic *extended tube model* (3.20) at a constant temperature of 293 K using the material parameters listed in Table 5.3. In this calculation, a linear loading cycle with a prescribed penetration $\bar{d}_N = 3$ mm and a duration of impact $T = 0.01$ s is calculated in 90 quasi-static load steps, whilst all lateral displacements are fixed.

This full scale tread model is then divided by the transition area $\partial\Omega_M$ that is situated at z = 20 mm into a mesoscale model (see Figure 5.8 (b)) and a macroscale model (Figure 5.8 (c)). The mesoscale model (864 elements, 3731 nodes) is used to identify the equivalent stretch-penetration relation $\lambda^{1\mathrm{D}}(\bar{d}_N)$ and the scaling factors c_{el} and c_{visco} for the constitutive contact model (5.51) based on the bulk material. In order to realize the assumed uniaxial compression test, the lateral displacements are held fixed only at the central axes ($u_x = 0$ at x=0 and $u_y = 0$ at y=0) of this model, which excludes rigid body motions. In the macroscale model (340 elements, 2165 nodes) only the behavior of the bedding is approximated by finite elements. The behavior of the mesoscale tread-sphere interaction is described by the homogenized constitutive contact model that is applied to the contact elements. The results of the macroscale model are finally compared to those of the full scale reference model in order to prove the accuracy of the presented approach.

The deformation u_z in the central plane y = 0 mm for all three simulated models at the maximum prescribed penetration $\bar{d}_N = 3$ mm is presented in Figure 5.8 (d)-(f). In Figure 5.8 (d) it can be observed that the large local deformation caused by the asperity becomes homogeneous towards the interface plane. Due to this fact, the chosen position for the separation by the interface plane and the prescription of a uniform displacement on the top side of the mesoscale model are plausible, as this motion precisely describes the behavior of the interface.

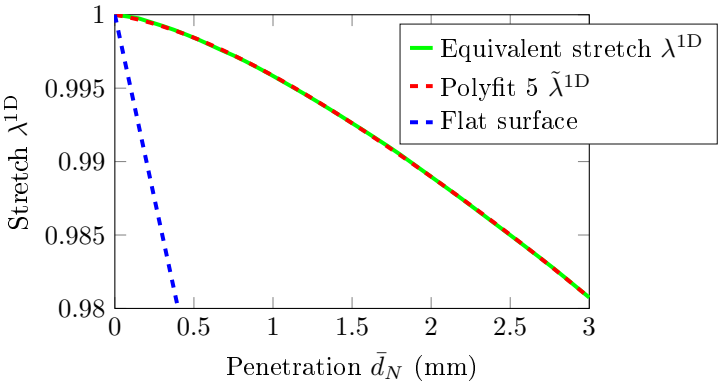

Figure 5.9: Approximation of the stretch-penetration relation for tread-sphere contact.

First the elastic response of the tread-sphere interaction (Figure 5.8 (b)) is calculated with the mesoscale model and homogenized. With the results of this step, both the scaling factor c_{el} for the elastic material parameters and the polynomial least squares approximation of the stretch-penetration relation $\tilde{\lambda}^{1D}(\bar{d}_N)$ are identified for this contact scenario. This approximation enables the evaluation of the equivalent kinematics of the uniaxial compression test and can be performed with freely available software packages, as described in section 5.4. The result of this approximation is depicted in Figure 5.9 and it can be observed that the the numerical results are fit well. Note that due to the nonlinearity of the resulting stretch-penetration a fifth-order polynomial is required to obtain a high-accuracy representation in this example. This accuracy is necessary, as the pressure calculation using the constitutive contact model is very sensitive to the stretch. Due to this high polynomial order, the least squares optimization must be restricted by the conditions Equation 5.68. The fulfillment of these restrictions prevents oscillations and non-monotonic behavior of the approximation, which is of crucial importance for the stability of the contact algorithm in the further course of this study.

Comparing the resulting nonlinear stretch-penetration relation on the sphere with those on a flat surface (dashed blue line) it can be observed that the slope is much smaller on the sphere. The slope on the flat surface is known a priori and forms the upper bound. The smaller slope on the sphere yields the conclusion that the contact behavior is also much softer than on the flat surface.

After the homogenization of the elastic behavior, the scaling factor c_{visco} for the viscoelastic material constants is evaluated based on a viscoelastic simulation. Here, the same linear loading cycle (maximum penetration $\bar{d}_N = 3$ mm, duration of the impact 0.01 s, 90 quasi-static load steps) as used for the full scale model was applied. The scaling factors for this example were identified as

$$c_{\text{el}} = 1.023 \text{ and } c_{\text{visco}} = 0.801. \tag{5.69}$$

The approximation of the response of the mesoscale model (Figure 5.8 (b)) in terms of the constitutive contact model (5.51) is shown in Figure 5.10 (a)-(d). Both, the elastic and the viscoelastic response of the vertical reaction force R_z over the prescribed penetration $\bar{d}_N$ (depicted in Figure 5.10 (a)) are represented very well. Here, the nonlinear reaction force stems from the hyper-elastic material formulation and the continuous increase in contact area. As expected, the time-dependent response has a hysteresis that results from viscoelastic effects in the material. This effect can be observed also in the volume average external power $\mathcal{P}_{\text{ext}}$, which is therefore unsymmetric and finally causes a loss of external energy

$$E_{\text{ext}} = \int_{\mathcal{B}} \int_{t_0}^{t} \mathcal{P}_{\text{ext}} \, \mathrm{d}V \, \mathrm{d}t, \tag{5.70}$$

see Figure 5.10 (b) and (c). Note that one difficulty in optimizing the viscoelastic scaling parameter c_{visco} is the accurate representation of the uplift and separation of the tread block. Due to the applied displacement controlled evaluation of the constitutive contact model, the uplift effect is not properly depicted, which causes the strong increase in dissipation at the end of the load cycle, see Figure 5.10 (c). As a result of this error balancing, the internal dissipation is depicted with a maximum deviation of $\approx 15\%$ for the present contact scenario, see Figure 5.10 (c). This error can be reduced by increasing the scaling factor c_{visco}, which however causes a severe reduction in the accuracy of the mechanic response. This impaired accuracy can be regarded as a restriction of the presented approach and requires further development in order to be overcome.

The homogenized constitutive contact model is then applied to the macroscale model (Figure 5.8 (c)) in order to validate the approximation quality with the results obtained from the full scale model (Figure 5.8 (a)). In this study, both models were simulated isothermally at different loading frequencies (1 Hz, 10 Hz and 100 Hz) and service temperatures (273 K, 293 K and 333 K). The absolute percentage approximation error was evaluated at the maximum penetration $\bar{d}_{\text{max}} = 3$ mm and at the end of the load cycle in each simulation. All resulting errors are depicted in Figure 5.11, which all lie below a tolerance of 10%. It can be observed that the change in frequency positively influences the error in the reaction force and the external energy at maximum penetration, see Figure 5.11 (a). This influence is plausible, as viscous effects are less pronounced when the period of the load cycle is much larger or much smaller than the relaxation time. On the other hand, the error in the energy loss at the end of the cycle increases with decreasing frequency. This fact is based on the difficulty to capture the separation of tread block and surface accurately. Due to the equivalence of frequency and temperature a similar behavior can be observed for the influence of the service temperature, illustrated in Figure 5.11 (b). At lower temperatures viscoelastic effects are much more pronounced, see section 3.5.

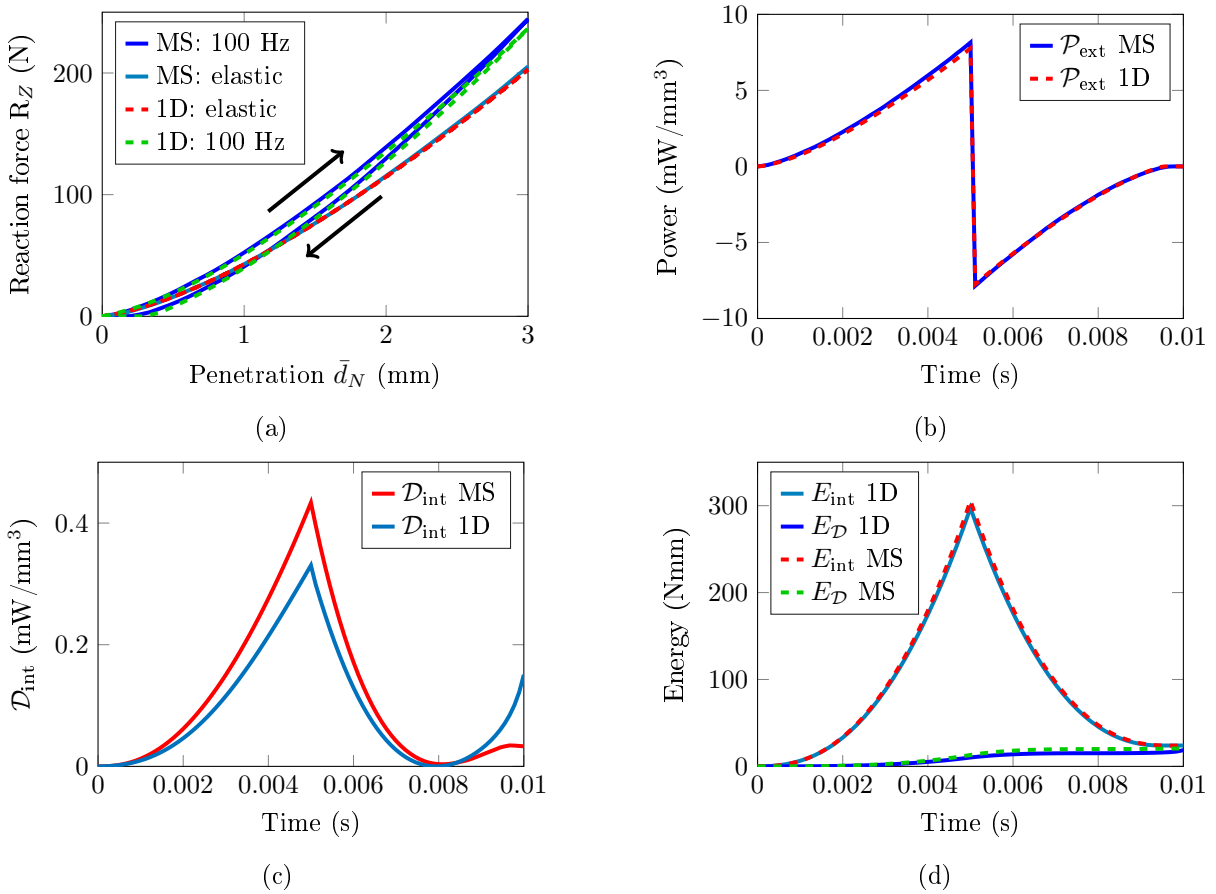

Figure 5.10: Comparison of the mechanical behavior of the mesoscale model (MS) and its representation by the constitutive contact model (1D).

Therefore, the energy loss in the cycle is approximated better, but the resulting reaction force and the stored external energy at maximum penetration are less accurate. This behavior arises from the fact that the stretch-penetration relation is not affected by the change of service temperature. Therefore, it can be concluded that for practical applications the scaling parameters need to be evaluated only at a single temperature. This fact significantly reduces the testing effort compared to covering the entire parametric space of penetration depth, loading frequency and temperature.

In the next step of this study, a coupled thermomechanical simulation was conducted in order to demonstrate the extensibility of this approach. Here, the initial temperature was set to 273 K and a loading frequency of 10 Hz was chosen. Additionally, the material model was extended by a second *Maxwell-element* with $\mu_{\text{v}}^2 = 0.5$ N/(mm^2) and $\eta_{\text{v}}^2 = 0.03$ Ns/(mm^2) (relaxation time $\tau_{\text{v}}^2 = 0.03$ s). Analogous to the previous examples, the parameters of the constitutive material model were scaled by the factors given in Equation 5.69,

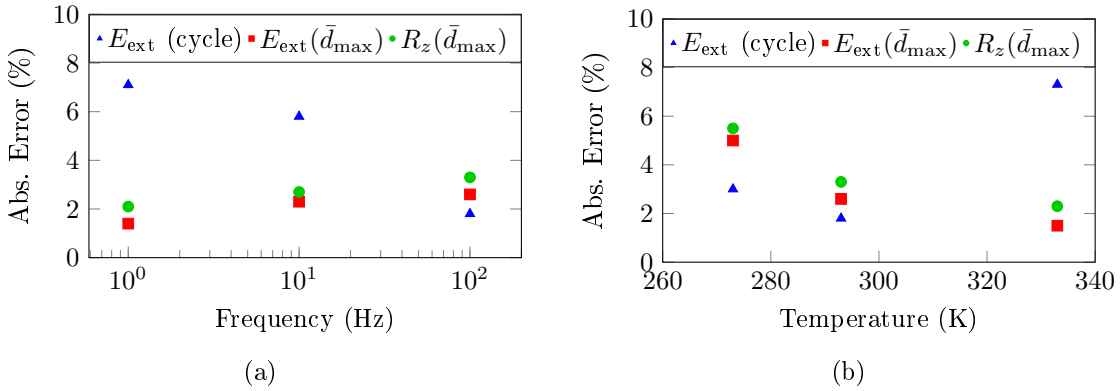

(a) (b)

Figure 5.11: Resulting approximation error of the macroscale model for different loading frequencies (a) and service temperatures (b).

which were identified at the mesoscale level model with just one *Maxwell-element*. The comparison of the resulting reaction forces over penetration and the external energy over the time of the load cycle is displayed in Figure 5.12. Even though the dissipated energy acts as a heat source in this simulation, the increase in service temperature is restricted to the local area of large deformation, see Figure 5.8 (d). The figure reveals that the increase in volume average temperature is negligible, see also [Beyer and Nackenhorst, 2014]. In this simulation, the absolute percentage error of the maximum reaction force was 4.5%, that of the maximum stored external energy was 4.4%, and the energy loss at the end of the cycle contained an error of 5.5%. The high quality of the macroscale representation allows for the conclusion that the identified scaling parameters are valid for a variety of material models.

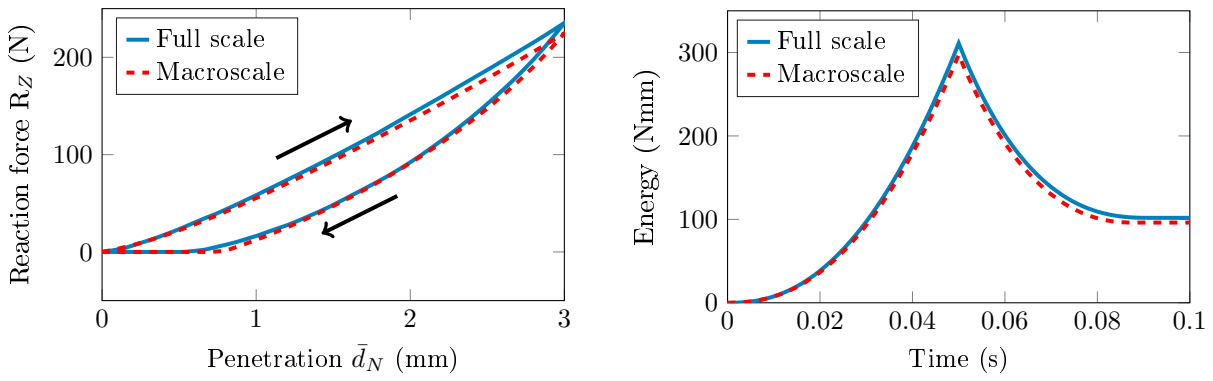

(a) (b)

Figure 5.12: Representation of the thermomechanical contact behavior of a tread block at 273 K, with a load frequency of 10 Hz and two *Maxwell-elements*.

5.4.3 Stochastic homogenization of tread-road interaction

In this second example, the average viscoelastic contact interaction of tread blocks with the rough and the smooth measured road surfaces (see subsection 5.3.2) is computed. This stochastically averaged tread-road interaction is then represented by a homogenized constitutive contact model. Analogous to the previous example, a polynomial approximation for the equivalent uniaxial stretch $\tilde{\lambda}^{1D}(\bar{d}_N)$ as well as the scaling c_{el} and c_{visco} for the material parameters are identified based on this solution. The fulfillment of these goals requires the solution of the stochastic contact problem (5.56), introduced in section 5.2, which is obtained by a *Quasi Monte Carlo simulation* (QMC-simulation). In this simulation, first the elastic and then the viscoelastic average tread-road interaction is identified on both road surfaces. In order to demonstrate the practical relevance of the homogenization ap-

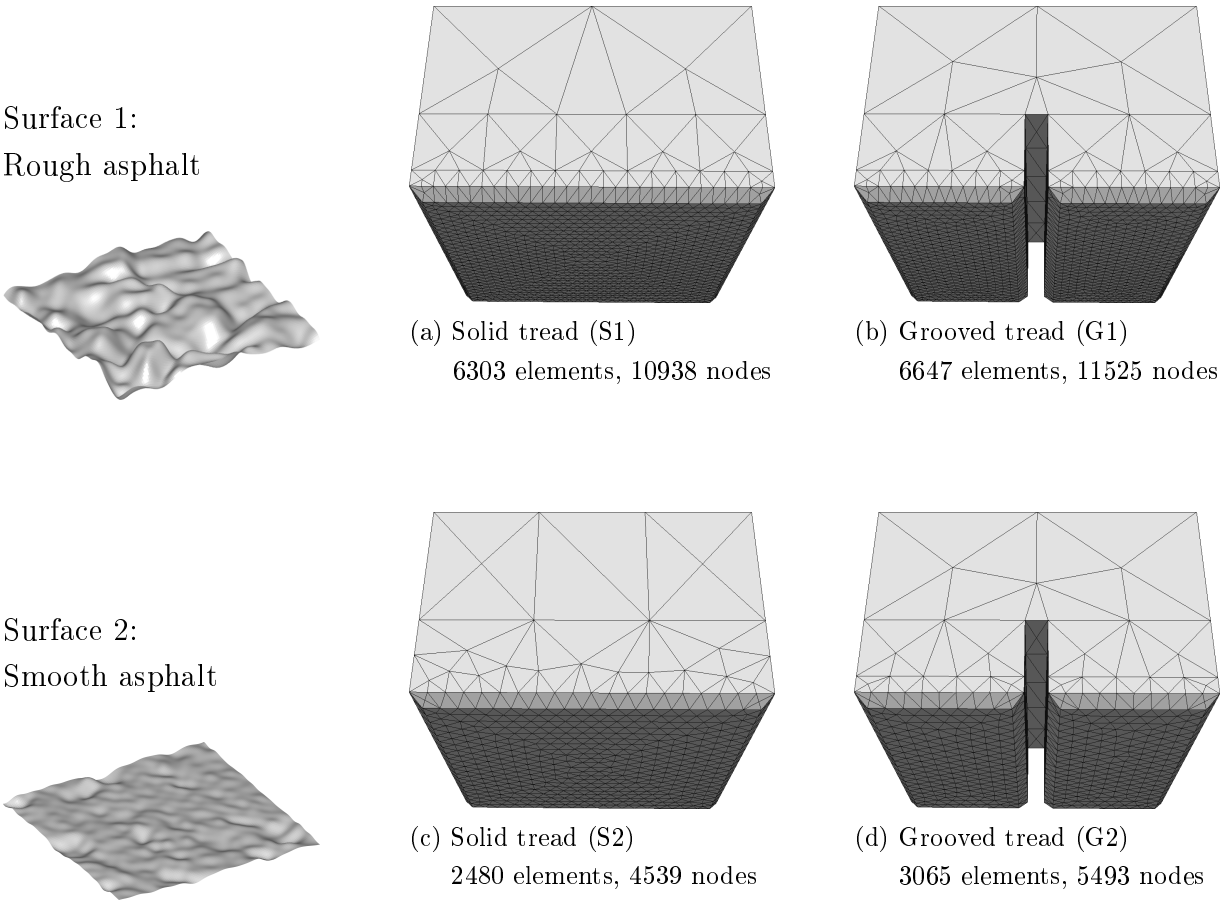

(a) Solid tread (S1)
6303 elements, 10938 nodes

(b) Grooved tread (G1)
6647 elements, 11525 nodes

(c) Solid tread (S2)
2480 elements, 4539 nodes

(d) Grooved tread (G2)
3065 elements, 5493 nodes

Figure 5.13: Tread block models (solid and grooved) used in the QMC-simulations to obtain their average contact behavior on the rough and on the smooth asphalt.

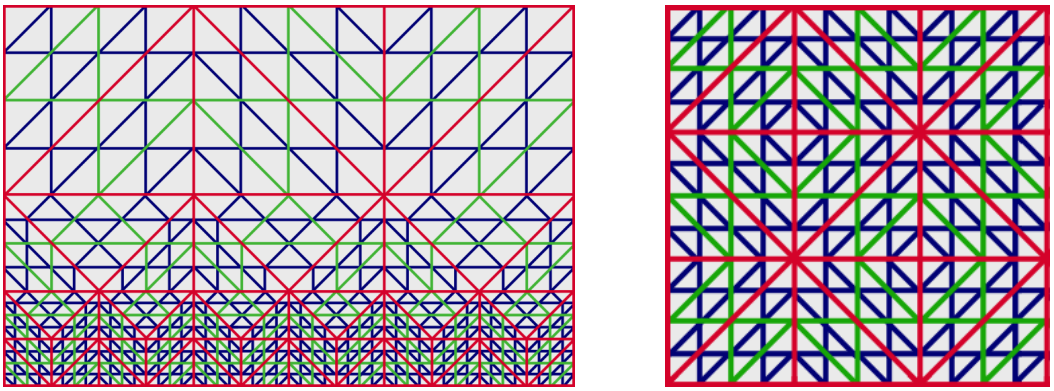

(a) Lateral view

(b) Magnified view onto the contact surface

Figure 5.14: Nested FE-meshes of the solid tread block models for the convergence study. The line colors mark the level of refinement as follows: red is the first, green is the second, and blue is the third level.

proach, the contact behavior of a solid as well a grooved tread block are calculated and homogenized. In general, tread designs have a far more complex structure, but this simple example proves that differences in the average structural response due to design changes can be represented. The resulting constitutive contact models are applied in the next chapter in order to evaluate the influence of surface roughness on rolling resistance.

The finite element models, which were used to perform the QMC-simulations, are depicted in Figure 5.13 together with the surface they are pressed upon. In order to resolve the asperities of the rough asphalt a finer spatial resolution (max. edge length 1.41 mm) than on the smooth surface (max. edge length 2.12 mm) was necessary. For the sake of computation time a coarser mesh was used on the smooth asphalt. Analogous to the previous example, all vertical displacements of the top nodes are prescribed, and the lateral displacements are constrained only in the central axis in order to mimic a uniaxial compression test. Furthermore, the same viscoelastic *extended tube model* is used with the material parameters given in Table 5.3. In order to resemble real tread blocks and to improve numerical stability, all edges in the contact zone were cut at an angle of 45°.

In order to approximate the accuracy of the meshes that were used in the QMC-simulations a convergence study on the resulting reaction forces was conducted. Therefore, a rectangular tread block was meshed with three different element size levels, in which the longest edge of each contact element are 1: 3.54 mm; 2: 1.76 mm; and 3: 0.88 mm. The lateral view and a magnification of the contact area of these meshes are presented in Figure 5.14 (a) and (b). It can be observed that the mesh of the first refinement level (marked by the red lines) has a regular structure, which yields tetrahedrons with an optimal aspect

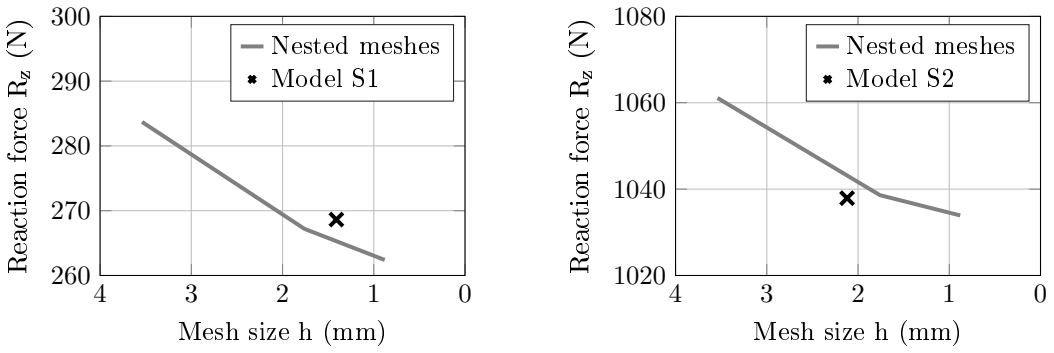

(a) Rough asphalt surface

(b) Smooth asphalt surface

Figure 5.15: Convergence of the maximum reaction force over mesh size using red refined nested meshes (gray line) compared to the result of the locally fine meshes used in the QMC-simulations (black cross) in contact with both asphalt surfaces.

ratio. Both subsequent levels were constructed by so-called "red refinement" in order to maintain the initial mesh quality. These nested meshes also allow for an exact projection of the results from a coarser to a finer mesh level. As for the other models, the applied displacement boundary conditions resemble a uniaxial compression test with a prescribed maximum penetration of $\bar{d}_N = 2.5$ mm.

The resulting reaction forces at maximum penetration on both surfaces are depicted in Figure 5.15 (a) and (b). As expected, the reaction forces decrease with element size and converge to a final value that has not yet been reached. Nonetheless, it is concluded that the accuracy of the meshes S1 and S2 (values at the black crosses) is sufficient for the intended application in the QMC-simulations later on in this study.

In a second preliminary investigation, the influence of the applied bandpass filtering (see subsection 5.3.3) on the reaction force was observed. Therefore, the finest mesh level of the models used in the previous study (longest edge of each contact element 0.88 mm) was simulated, which is most sensitive to high-frequency small asperities. The coarsest filters used in this study are those, which were later on applied for the QMC-simulations, with a minimal wavelength (WL-min) of 4 mm on the smooth asphalt and WL-min = 5 mm on the rough asphalt. These filters were compared to a finer filtering with WL-min = 3 mm, and a quasi unfiltered surface with WL-min = 1 mm. The upper bound of a maximal wavelength (WL-max) of 120 mm was not altered, as the influence of waviness effects was not under observation here.

The resulting reaction force penetration curves for these bandpass filter levels are shown in Figure 5.16 . When comparing the different results, a negligible softening of the

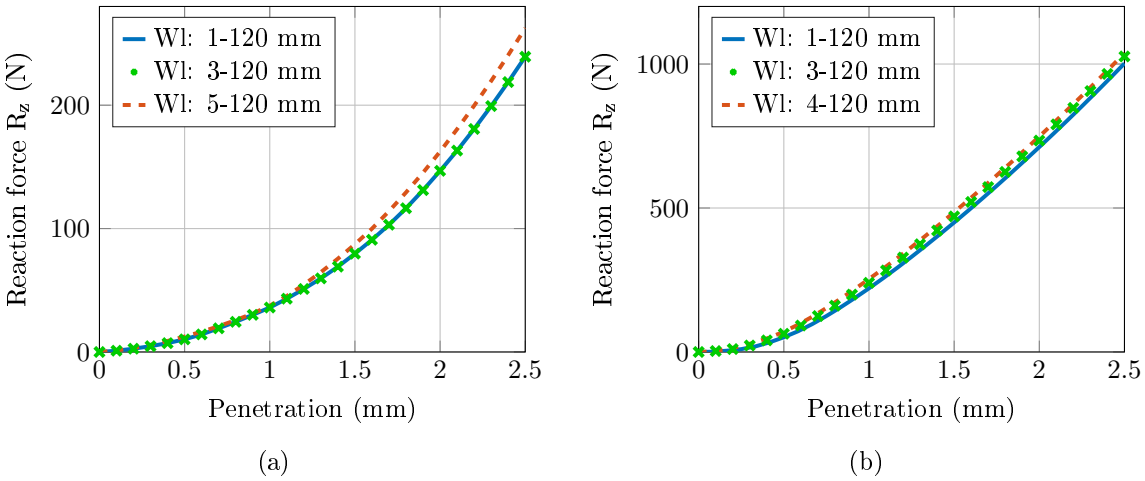

Figure 5.16: Resulting reaction forces over penetration for different bandpass filters, which define a wavelength range (Wl) for the surface representations of (a) the rough asphalt and (b) the smooth asphalt.

reaction forces can be observed when accounting for smaller wave-lengths (larger number of high-frequency contributions). On the rough surface presented in subsection 5.3.3 (c), the force penetration curve of the finest and the next coarser level with a wavelength of 3-120 mm coincide, which indicates that the filtering does not at all affect these results. For the results obtained on the smooth surface, shown in subsection 5.3.3 (d), the filtering has a small offset effect. Here, the block is almost in full contact, so that the contribution of small frequencies is more strongly pronounced. Nonetheless, the gain of information is negligible in this study of mesoscale contact interaction. Therefore, the 20 times higher computation time to evaluate the unfiltered surface with 180000 frequencies, compared to $\approx$ 10000 frequencies in the filtered representation, was avoided due to the fact that it is computed multiple times in every closest point projection at every integration point in order to calculate the contact contribution.

The average elastic response of the tread blocks on the road surfaces is identified by solving the random rough surface contact problem (5.56) using a QMC-simulation. Herein, 600 uniformely distributed samples were calculated, where each realization was located at a different position $\boldsymbol{\phi}$ on the surface that was determined from the Sobol-sequence. Prior to each calculation, the tread block was positioned on top of the highest asperity in order to remove unphysical offsets in the reaction force response caused by waviness effects. In this study, the final vertical displacement $\bar{d}_N$ was set to 3 mm for all models, and was applied in 30 load steps on the rough asphalt surface and 25 load steps were used on the smooth asphalt surface. All simulations in this study were calculated isothermally at a reference

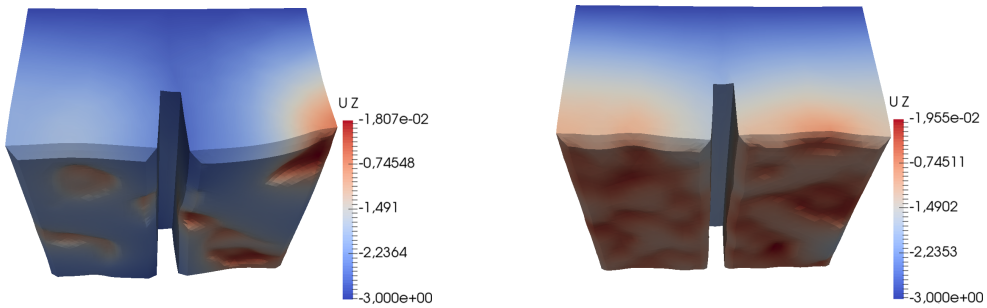

(a) Rough asphalt (b) Smooth asphalt

Figure 5.17: Deformation of the grooved tread blocks at maximum penetration in one exemplary realization.

temperature of 293 K using the same thermo-viscoelastic *extended tube model* as in the previous studies with the material parameters given in Table 5.3.

In each realization of this QMC-simulation, the contacting surface asperities caused local deformations of the tread blocks. An example for the deformation of the grooved tread on each surface is depicted in Figure 5.17. On the rough asphalt surface Figure 5.17 (a), the large surface asperities cause a quite complex deformation of the tread block with large local changes in curvature. In contrast to this, the deformation on the smooth surface Figure 5.17 (b) is rather uniform and exhibits only small waves.

In view of this complex deformation, the solution for the rough surface contact problems proves to be a challenging task, especially with respect to the robustness of the applied contact constrained enforcement algorithm. Due to the quasi incompressible material behavior, the penetration by an asperity is compensated by large tangential relative motions, which push integration points from peeks to gaps changing the active set. In this context, instabilities are caused by rapid changes in the surface normal direction due to high-frequency roughness on top of the mesoscale surface asperities. This effect can hardly be resolved by small load steps or by reducing the penalty parameter used in the *Uzawa algorithm*, and it is most pronounced when approaching full contact. The only possibility to achieve a higher stability in the current algorithmic framework was observed in the relaxation of the volume preservation restriction by reducing the *Poisson ratio*.

For these reasons, 34.7% of the solid tread samples and 45.8% of the grooved tread samples failed on the rough asphalt surface in this QMC- simulation. The number of completed samples in area sections sized 30x30 mm (tread block size) of the sampling region is presented in Figure 5.18. It can be observed that the distribution of the completed samples cover most of the surface. In case of the solid tread block model, three area sections were not sampled, and four area sections were not covered in case of the grooved model.

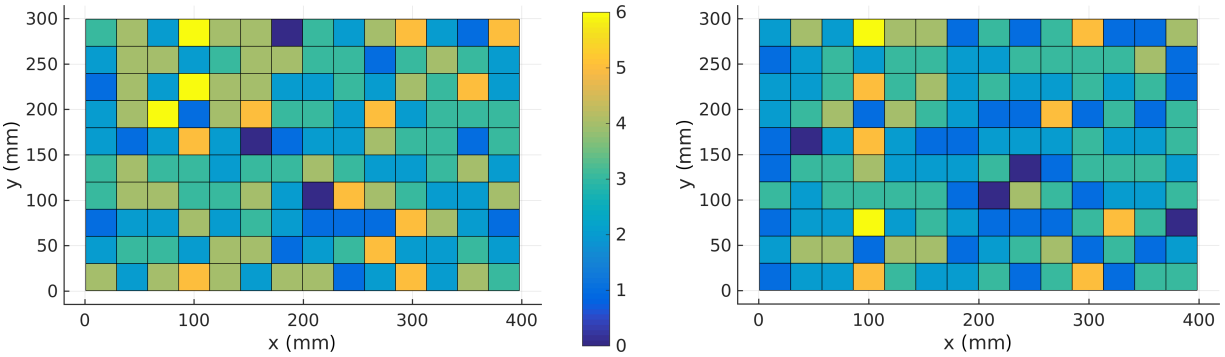

(a) Solid tread: 65.3% completed samples.

(b) Grooved tread: 54.2% completed samples.

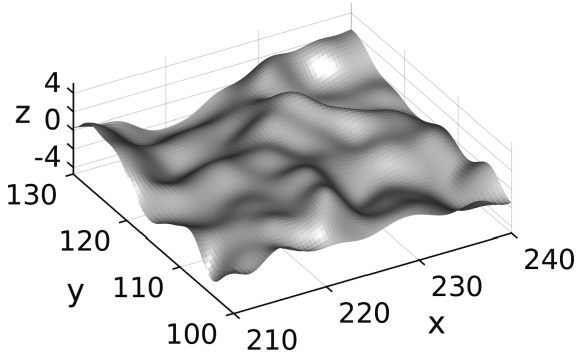

(c) Fail region

Figure 5.18: Number of completed samples per area section (30x30 mm) for both tread models on the rough surface and magnified view of a surface region ($x \in [210, 240]$ mm, $y \in [90, 120]$ mm) with no completed samples.

Furthermore, failed samples can be observed to cluster in some regions. In Figure 5.18 (c) a magnified view onto the surface of one of these failing sections is shown in order to point out the reasons for the failure of the contact algorithm. Steeply flanked asperities can be observed in this area, and accordingly, the material is squeezed into the valleys causing very high local strains and relative motion. It was therefore concluded that the obtained results are biased, but still representative. As on the smooth asphalt only 5.2% of the solid tread samples and 12.5% of the grooved tread samples failed, this distribution is not depicted.

The resulting average displacements for both models on the rough asphalt are presented in Figure 5.19. As expected, the average deformation of the contact surface (bottom of the tread block) is quite homogeneous, but due to the large distance in between the asperities a certain variation can still be observed, which does not contradict a convergence of the normal reaction forces. Regarding the evolution of the mean reaction forces at maximum penetration, the results appears to change by less than 4 N ($\approx 1\%$) from 80 to 100%, which

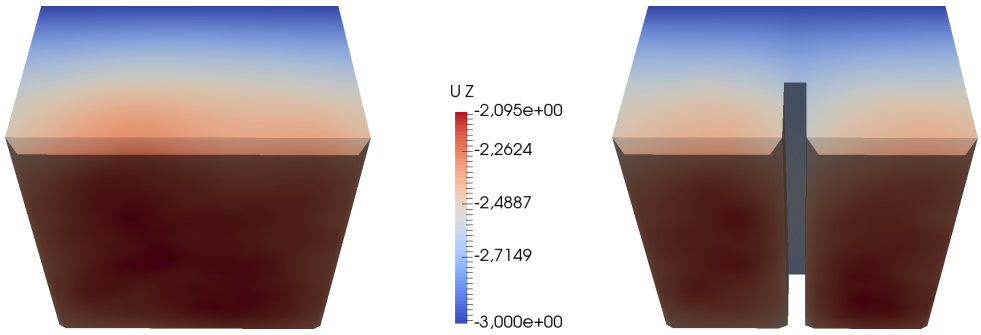

Figure 5.19: Average deformation of the tread blocks on the rough asphalt surface.

fulfills the accuracy requirements of this study, see Figure 5.20. Furthermore, the grooved tread block has a smaller contact stiffness than the solid tread block, as its material can be squeezed to the sides to the block more easily. This fact generally results in larger dissipation. Additionally, the hypothesis that the thermo-viscoelastic contact behavior can be represented by an equivalent uni-axial compression test is validated by the fact that the tangential reaction forces vanish in the stochastic average, which can also be regarded as a measure for convergence.

The average deformation of the contact surface of both tread blocks on the smooth surface is ≈ 0 (see Figure 5.21), which results from the structure of this surface being relatively flat except for some valleys. Due to the surface topology of the smooth surface, the vertical deformation is much smaller than on the rough surface, where only single asperities penetrate the tread block. This larger contact area results in a much higher contact stiffness of the interface, see [Persson, 2006a], which then causes less dissipation, as the volume average stretch velocities occurring in a load cycle are smaller. This can also be observed from the convergence behavior of the reaction forces, in which the difference of the mean value does not exceed 15 N ($\approx 1\%$) for any illustrated percentage of the samples,

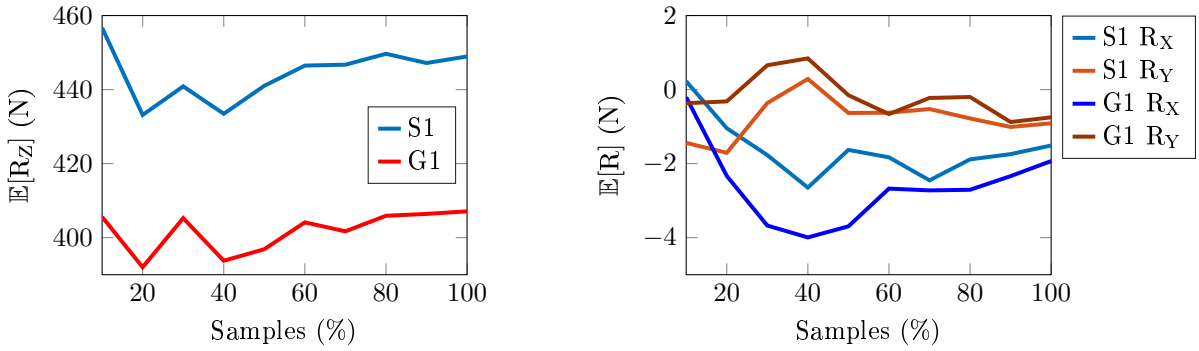

Figure 5.20: Convergence of mean reaction forces for the solid (S1) and the grooved (G1) tread model on the rough asphalt at maximum penetration.

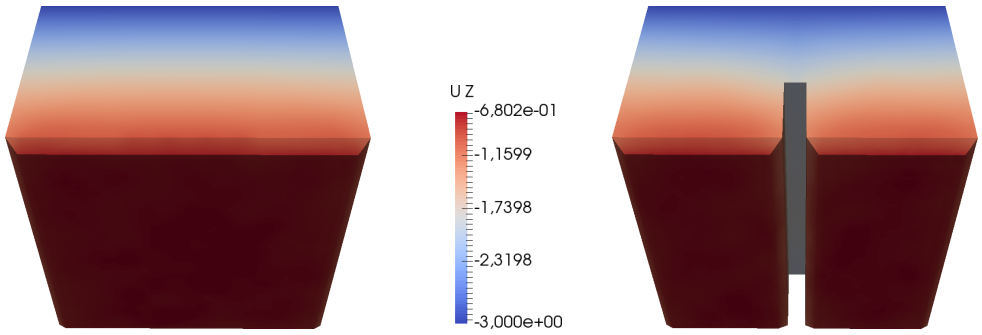

Figure 5.21: Average deformation of the tread blocks on the smooth asphalt surface.

which means that only 60 samples would have been sufficient for the stochastic averaging on this surface, see Figure 5.21.

Finally, the resulting stochastically averaged force-penetration curves and their approximation by means of the homogenized constitutive contact model (5.51) is presented in Figure 5.23. It can be observed that the resulting contact behavior of all four contact pairings is depicted with a high accuracy.

After the identification of the average elastic response, an additional QMC-simulation with 50 samples was conducted in order to obtain the average viscoelastic behavior. Therefore, the viscoelastic contribution of the *extended tube model* was set active again. In this study, a complete load cycle was simulated in each realization, in which the impact duration of the tread blocks the surfaces was 0.01 s that was subdivided into 60 load steps.

The results of this study revealed that the stored volumetric energy converges after a few cycles. According to this finding, this quantity was used to adapt the viscoelastic material scaling factor c_{visco}, where the stretch-penetration relation $\tilde{\lambda}^{\text{1D}}(\bar{d}_N)$ (see Appendix B) and the elastic scaling factor c_{el} were known from the previous study.

The approximation of the visco-elastic contact behavior is presented exemplary for the

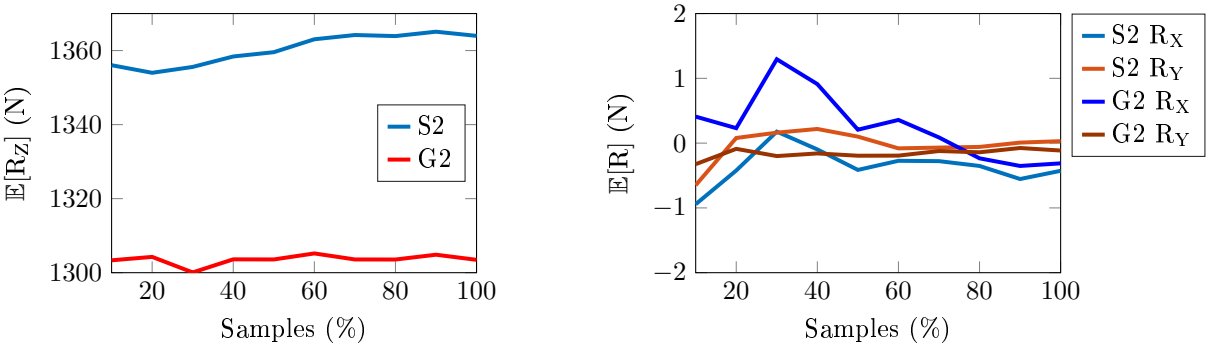

Figure 5.22: Convergence of mean reaction forces for the solid (S2) and the grooved (G2) tread model on the smooth asphalt at maximum penetration.

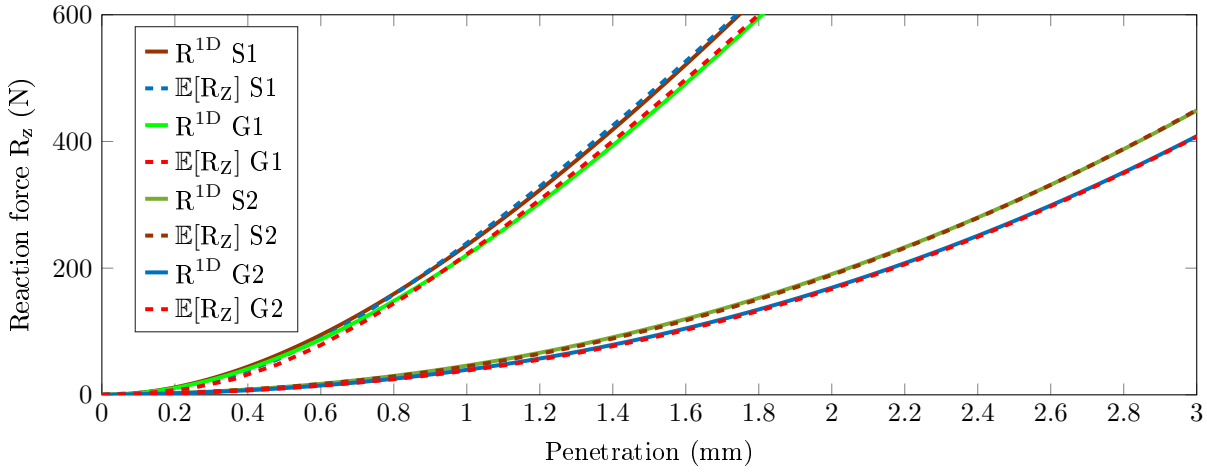

Figure 5.23: Elastic force-penetration curves on the rough and on the smooth asphalt.

grooved tread block on the smooth asphalt surface in Figure 5.24. Here, the smaller values of the reaction force (see Figure 5.24 (a)) and the stored volumetric energy (see Figure 5.24 (b)) compared to the homogenization model at maximum penetration result from the small viscoelastic scaling factor c_{visco}. This parameter was identified to minimize the difference of the dissipated energy at the end of the load cycle for this scenario. Note that an increase of this factor results in a better approximation of the force penetration curve as well as for the stored volumetric energy, but reduces the accuracy of the dissipated energy $E_{\mathcal{D}}$.

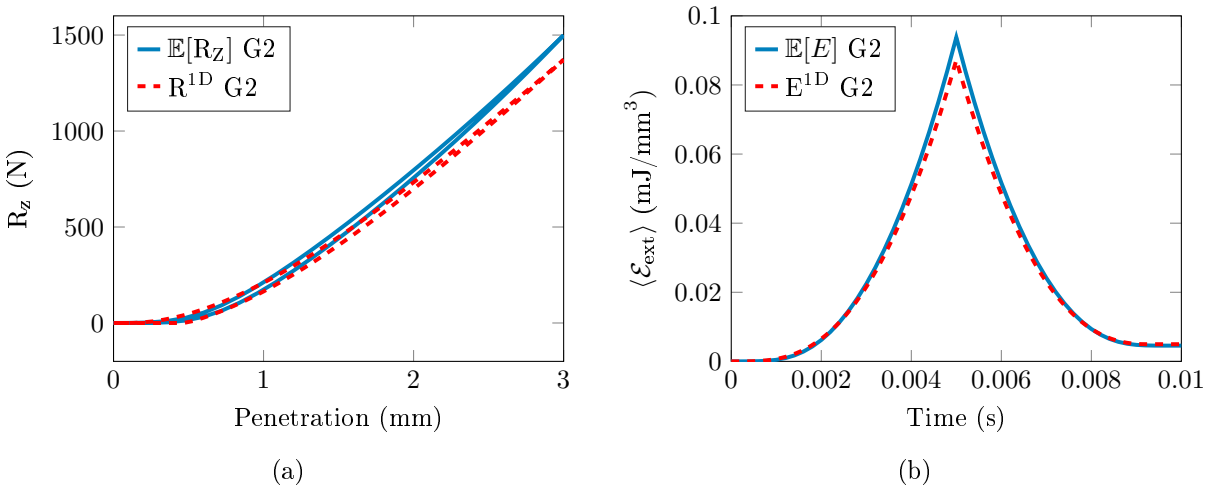

Figure 5.24: Approximation of visco-elastic force-penetration response (a) and stored volumetric energy (b) for model G2 at 100 Hz.

Table 5.4: Material scaling factors and absolute approximation error of the uniaxial constitutive contact model.

Model	c_{el}	c_{visco}	Err. $R_z(\bar{d}_{\max})$	Err. $\max \mathcal{E}_{\mathrm{ext}}$	Err. $E_{\mathcal{D}}$
Surface 1: Rough asphalt					
S1	1.0	0.49	5.7%	7.2%	8.6%
G1	0.97	0.5	7.8%	8.4%	10.0%
Surface 2: Smooth asphalt					
S2	1.045	0.75	6.0%	2.3%	9.2%
G2	1.02	0.72	8.5%	7.0%	9.0%

The scaling factors for the material parameters (see Table 5.3) as well as the approximation quality for all identified average contact behaviors are summarized in Table 5.4. In conclusion, the obtained results give a good approximation of the stochastically averaged tread-road interaction.

6 Rolling resistance simulations

In this chapter, the numerical framework for the rolling resistance calculation of tires accounting for stochastically averaged homogenized tread-road interaction is presented. This extension of the existing institute framework is realized by means of the constitutive contact model developed in subsection 5.1.3. In this framework, the mathematical model is formulated in terms of *Arbitrary Lagrangian Eulerian kinematics* (ALE-kinematics) presented in [Nackenhorst, 2000, 2004], which was briefly introduced in section 2.1. The treatment for frictional contact and transport of internal variables in the isothermal regime were developed in [Ziefle, 2007; Ziefle and Nackenhorst, 2008]. In order to account for the temperature dependence of tire rubber compounds, a thermo-viscoelastic material model as well as an isentropic operator split scheme to resolve the thermomechanical coupling were introduced in [Suwannachit, 2013; Suwannachit and Nackenhorst, 2013] for frictionless rolling contact.

The extension of this framework by the homogenized constitutive contact model (see subsection 5.1.3) enables the quantification of the influence of surface roughness and tread design on rolling resistance. In this context, the developments of [Ziefle, 2007] and [Suwannachit, 2013] have been united, allowing for the calculation of the pressure distribution within the tire's footprint in tractive rolling contact. In addition, frictional heating effects can be taken into account with the present framework, which is demonstrated in combination with sophisticated phenomenological friction law for rubber friction presented in [Huemer et al., 2001a].

In the following, the algorithmic treatment of the different nonlinearities occurring in the coupled thermomechanical problem of tractive rolling contact is briefly introduced. Thereafter, numerical examples demonstrating the capability of the extended numerical framework to quantify the influence of surface roughness on rolling resistance are presented. The amount of increase in rolling resistance is compared to the results presented in [van Haaster et al., 2015; Willis et al., 2014], who measured a difference of 8-10% in rolling resistance between a coarse and a smooth asphalt.

6.1 Statement of the mathematical problem

As a consequence of the severe temperature dependence of tire rubber, the calculation of the rolling resistance requires the solution of both the balance of linear momentum (2.40)

and the heat conduction equation (2.49). In the context of stationary rolling contact the choice of an ALE-kinematic formulation enables the expression of material time derivatives (2.23) in terms of spatial gradients for both transient problems. Due to this fact, they can be reformulated as boundary value problems without neglecting inertia effects, see [Nackenhorst, 2000; Suwannachit, 2013]. As a result of the kinematic description, material particles are not fixed to the mesh and therefore the evolution of the material history describing inelastic effects, e.g. viscoelasticity (3.45), cannot be calculated with algorithms developed in *Lagrangian kinematics*. The same applies for the direct enforcement of the stick condition (4.7) in case of tractive rolling contact.

In the present framework, these difficulties are solved within a staggered scheme, in which the material time derivative (2.23) is separated into

$$\dot{\boldsymbol{\alpha}}_{\mathrm{v}} \;=\; \left.\frac{\partial \boldsymbol{\alpha}_{\mathrm{v}}}{\partial t}\right|_{\boldsymbol{X}} + \mathrm{Grad}\boldsymbol{\alpha}_{\mathrm{v}}^{(i)} \cdot \boldsymbol{w} \tag{6.1}$$

a *Lagrangian* contribution $\dot{\boldsymbol{\alpha}}_{\mathrm{v}} = \frac{\partial \boldsymbol{\alpha}_{\mathrm{v}}}{\partial t}\big|_{\boldsymbol{X}}$, assuming $\boldsymbol{w} = 0$, and an advective *Eulerian* part $0 = \frac{\partial \boldsymbol{\alpha}_{\mathrm{v}}}{\partial t}\big|_{\boldsymbol{X}} + \mathrm{Grad}\boldsymbol{\alpha}_{\mathrm{v}} \cdot \boldsymbol{w}$. By means of this separation, the material history can be integrated using algorithms developed in *Lagrangian kinematics* within the local evolution phase. The updated material history (internal variables) is then transported about an angular increment $\Delta\phi$ in the advective transport phase. The size of this angular increment in conjunction with the angular velocity ω determines the incremental time step $\Delta t = \Delta\phi/\omega$ in the local evolution phase.

In this thesis, the thermo-viscoelastic rolling contact problem is solved with a modified version of the three-phase fractional step approach presented in [Suwannachit, 2013] in order to enable the calculation of the tire's rolling resistance. In this fractional step approach, the thermomechanical coupling is treated with the isentropic operator split scheme (see section 3.4) whilst the material history evolution is calculated in incremental time steps, which results in the following subproblems:

1. Mechanical tractive rolling contact (6.4)
2. Stationary heat conduction in the rotating system (6.13)
3. Advective transport of material history (6.18)

The nonlinear Galerkin approximations of the mechanical and the thermal subproblem are both obtained with the *Newton-Raphson method*, see section 3.4. Then, the advective transport problem of the internal variables in the tire structure is solved using the *time discontinuous Galerkin method*. In case of using the newly developed constitutive contact model to represent the thermo-viscoelastic tread-road interaction, this transport problem

also needs to be solved in the contact area. After the advection problem is solved, the local internal variables are updated. Note that the transport of the internal variables alters their contribution to the local entropy (3.49) calculated in the thermal phase. The consistent solution of the isentropic mechanical problem in the next time step therefore requires a recalculation of the local entropy after the transport phase has been completed. At the end of each time step the convergence of the material history evolution

$$\left\| \dot{\boldsymbol{A}}_{\mathrm{v}} \right\|_{\max} = \max \sqrt{\sum \left(\dot{A}_{\mathrm{v}} \right)^2_{ij}} < tol \tag{6.2}$$

is checked, so that the solution fulfills the stationarity condition (2.25). The convergence of the material history evolution depends on the ratio of relaxation time to angular velocity and is in general reached after few revolutions. Finally, the rolling resistance as well as the tractive response can be calculated in a post-processing step.

6.1.1 Mechanical subproblem

Following the discussion in [Nackenhorst, 2000], the direct evaluation of material acceleration (2.27) requires a C^1-continuous discretization of the body. Alternatively, [Govindjee et al., 2014b] introduced the velocity as primary variable in a C^0-continuous approach. However, both approaches result in non-symmetric system matrices.

This issue was solved in [Nackenhorst, 2000] by reformulation of the inertia term and application of the divergence theorem, which results in

$$\int_{\mathcal{B}} (\varrho \mathrm{Grad}\boldsymbol{v} \cdot \boldsymbol{w}) \cdot \delta\boldsymbol{u} \mathrm{d}V = \int_{\partial\mathcal{B}} \varrho \delta\boldsymbol{u} \cdot \boldsymbol{v}\boldsymbol{w} \cdot \boldsymbol{N} \mathrm{d}A - \int_{\mathcal{B}} \boldsymbol{v} \cdot \delta\boldsymbol{u} \mathrm{Div}(\varrho\boldsymbol{w}) - \varrho\boldsymbol{v} \cdot (\mathrm{Grad}\delta\boldsymbol{u} \cdot \boldsymbol{w}) \mathrm{d}V. \tag{6.3}$$

Here, the first term represents the momentum flux across the system boundary, which is neglected assuming $\boldsymbol{w} \cdot \boldsymbol{N} = 0$, see [Nackenhorst, 2000]. Later on, it has been shown in [Ziefle, 2007] that this assumption is not valid for discretized structures in general and therefore the neglect causes jumps in the inertia forces along the surface in case of varying circumferential element size. The last term vanishes due to conservation of mass in the rotational symmetric body $\mathrm{Div}(\varrho\boldsymbol{w}) = 0$. The remaining second term can be evaluated directly in terms of a C^0-continuous discretization and results in a symmetric contribution of the inertia term, which is characteristic for conservative systems. The mechanical weak form of the stationary rolling contact problem then reads

$$\mathcal{G}_{\boldsymbol{u}}(\boldsymbol{u}, \delta\boldsymbol{u}) \stackrel{!}{=} 0 = \int_{\mathcal{B}} -\varrho\boldsymbol{v} \cdot (\mathrm{Grad}\delta\boldsymbol{u} \cdot \boldsymbol{w}) + \boldsymbol{S} : \delta\boldsymbol{E} \mathrm{d}V + \int_{\partial_t\mathcal{B}_t} \boldsymbol{t} \cdot \delta\boldsymbol{u} \mathrm{d}a + \int_{\partial_c\mathcal{B}} \boldsymbol{T}_c \cdot \delta\boldsymbol{u} \mathrm{d}A. \tag{6.4}$$

In this study, body forces are neglected. The boundary conditions are defined as

$$\boldsymbol{u}(\boldsymbol{X}, t) = \bar{\boldsymbol{u}}(\boldsymbol{X}, t) \; \forall \boldsymbol{X} \in \partial_{\boldsymbol{u}}\mathcal{B} \quad \text{and} \quad \boldsymbol{\sigma}(\boldsymbol{x}) \cdot \boldsymbol{n}(\boldsymbol{x}) = \boldsymbol{t}(\boldsymbol{x}) \; \forall \boldsymbol{x} \in \partial_{\boldsymbol{t}}\mathcal{B}_t, \tag{6.5}$$

on the separated boundary $\partial\mathcal{B} = \partial_{\boldsymbol{u}}\mathcal{B} \cup \partial_{\boldsymbol{t}}\mathcal{B} \cup \partial_c\mathcal{B} \wedge \partial_{\boldsymbol{u}}\mathcal{B} \cap \partial_{\boldsymbol{t}}\mathcal{B} \cap \partial_c\mathcal{B} = \emptyset$ using the projection $\partial_{\boldsymbol{t}}\mathcal{B}_t = \boldsymbol{\Phi}(\partial_{\boldsymbol{t}}\mathcal{B})$. Here, the surface tractions $\boldsymbol{t}$ are defined in the current configuration $\mathcal{B}_t$ in order to account for follower loads such as the inflation pressure

$$\boldsymbol{t}_{\text{Infl}} = -p_{\text{Infl}}\boldsymbol{n}(\boldsymbol{x}), \tag{6.6}$$

which acts along the surface normal $\boldsymbol{n}(\boldsymbol{x})$ with the magnitude p_{Infl}, see [Wriggers, 2008].

In this thesis, the tire is assumed to be in contact with a flat and rigid surface, which has a constant surface temperature and moves with a prescribed velocity $\boldsymbol{v}_R$. The non-penetration condition (4.23) is enforced with the *Augmented Lagrangian multiplier method* presented in section 4.3. Thus, no algorithmic changes are required as the normal contact contribution directly constrains the relative deformation $\boldsymbol{u}$. However, due to the fact that material particles are not fixed to the mesh, the stick condition $\dot{\boldsymbol{s}} = \boldsymbol{0}$ cannot be enforced using standard formulations, which are based on the direct evaluation of the relative slip. In this thesis, the stick condition is enforced with the algorithm presented in [Ziefle, 2007]. Here, the relative slip $\boldsymbol{s}$ is introduced as an additional nodal degree of freedom in the contact zone, which is formulated in the convective coordinates of the master surface. By means of this, the sliding velocity is defined by

$$\dot{\boldsymbol{s}} = (\boldsymbol{c} - \boldsymbol{v}_R) \cdot \boldsymbol{A} = \text{Grad}\boldsymbol{s} \cdot \boldsymbol{w}, \tag{6.7}$$

so that the slip can then be calculated in a weak sense by solving

$$\int_{\partial_c\mathcal{B}} ((\boldsymbol{c} - \boldsymbol{v}_R) \cdot \boldsymbol{A})\, \text{Grad}\delta\boldsymbol{s} \cdot \boldsymbol{w}\, \text{d}A = \int_{\partial_c\mathcal{B}} (\text{Grad}\boldsymbol{s} \cdot \boldsymbol{w})\, \text{Grad}\delta\boldsymbol{s} \cdot \boldsymbol{w}\, \text{d}A, \tag{6.8}$$

in which $\boldsymbol{A} = \{\boldsymbol{a}_1, \boldsymbol{a}_2\}$ is a tangent vector matrix, $\delta\dot{\boldsymbol{s}} = \text{Grad}\delta\boldsymbol{s} \cdot \boldsymbol{w}$ is the material time derivative (2.23) of the variation of slip, and the left side of the equation is the local sliding velocity in terms of the convective speed. The solution of this boundary value problem requires *Dirichlet boundary conditions* $s = s_0$, which are imposed on the leading edge of the footprint, where material particles enter the contact zone. The global slip distribution can be interpreted as the result of the local slip evolution

$$\boldsymbol{s} = \boldsymbol{s}_0 + \int_{t_0}^{t} \dot{\boldsymbol{s}} \text{d}\tau \tag{6.9}$$

of a material particle traveling through the contact zone. By means of this approach, both the standard return mapping algorithm formulated in *Lagrangian kinematics* and phenomenological friction laws can be applied. In this context, the sliding velocity$\dot{\boldsymbol{s}}$ can be used directly for the evaluation of the friction law (4.26) and the calculation of friction loss, which causes frictional heating. Note that in case of linear shape functions in the element

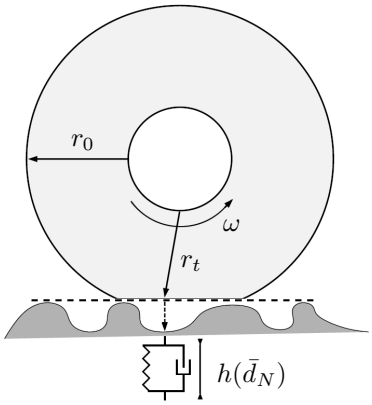

Figure 6.1: Relative kinematics of the projected integration point.

formulation the common approach to integrate the contact contribution using additional two-dimensional membrane elements, which discretize the contact surface of the three-dimensional body, does not allow for a consistent computation of the convective velocity $\boldsymbol{c}$. These linear membrane elements can only depict in-plane deformations and therefore the required displacement gradient Grad$\boldsymbol{u}$ cannot be calculated correctly, see [Chapelle and Bathe, 2011] for details. In this case, the integration needs to be performed on the surface of the parent element, so that Grad$\boldsymbol{u}$ can be evaluated correctly and $\boldsymbol{c} = \boldsymbol{w}$ for $\boldsymbol{u} = \boldsymbol{0}$.

Accounting for mesoscale tread-road interaction

In order to account for homogenized mesoscale tread road interaction in macroscale rolling resistance calculations, the constitutive contact model (5.51), which has been developed in subsection 5.1.3, is attached to the contact elements. This treatment results in a nonlinear, thermo-viscoelastic regularization of the normal contact constraint, see Figure 6.1. Here, the penetration $\bar{d}_N$ is assumed to compress the tread layer with initial height h_0, so that its current height is

$$h(\bar{d}_N) = h_0 - \bar{d}_N. \tag{6.10}$$

By means of this kinematic assumption, the contact contribution can be directly integrated on the contact boundary of the tire model.

6.1.2 Thermal subproblem

In order to obtain the stationary temperature distribution the heat conduction equation (3.10) needs to be solved. Following the argument presented in [Suwannachit, 2013], the calculation of the entropy rate is redefined as

$$\dot{s} = \dot{s}_e + \dot{s}_{\hat{c}} + \dot{s}_{ve} = -\frac{\partial s}{\partial \boldsymbol{C}} : \dot{\boldsymbol{C}} - \frac{\partial s}{\partial \Theta}\dot{\Theta} - \sum_i \frac{\partial s}{\partial \boldsymbol{\alpha}_{\mathrm{v}}^{(i)}} : \dot{\boldsymbol{\alpha}}_{\mathrm{v}}^{(i)}, \tag{6.11}$$

which can be separated into a thermoelastic contribution $\dot{s}_e$, the change of heat capacity $\dot{s}_c$ and a thermo-viscoelastic part $\dot{s}_{ve}$. The entropy rate was then reduced to

$$\varrho\dot{s} = -\frac{\partial\Psi(\boldsymbol{C},\Theta)}{\partial\Theta}\dot{\Theta} = \hat{c}(\Theta)\dot{\Theta} \quad \text{with } \frac{\dot{s}_e}{\mathcal{D}_{\text{int}}} \approx 0 \text{ and } \frac{\dot{s}_{ve}}{\mathcal{D}_{\text{int}}} \approx 0, \tag{6.12}$$

neglecting thermoelastic $\dot{s}_e$ and thermo-viscoelastic $\dot{s}_{ve}$ structural heating effects caused by mechanical deformation, which are of minor influence compared to the viscous dissipation. The remainder is the rate at which thermal energy is stored in the material.

The weak form of the heat conduction equation then yields

$$\begin{aligned}\mathcal{G}_\Theta(\boldsymbol{\Theta},\delta\boldsymbol{\Theta}) \overset{!}{=} \quad 0 = & \int_{\mathcal{B}} \left(\hat{c}(\Theta)\text{Grad}\Theta\cdot\boldsymbol{w} - \mathcal{D}_{\text{int}} - \varrho r\right)\delta\Theta + \text{Grad}\delta\Theta\cdot\boldsymbol{Q}\,\mathrm{d}V \\ & + \int_{\partial_q\mathcal{B}} Q_N\delta\Theta\,\mathrm{d}A + \int_{\partial_c\mathcal{B}} Q_c\delta\Theta\,\mathrm{d}A,\end{aligned} \tag{6.13}$$

which is subjected to the following boundary conditions

$$\Theta(\boldsymbol{X},t) = \bar{\Theta}(\boldsymbol{X},t)\;\forall\boldsymbol{X}\in\partial_\Theta\mathcal{B} \quad \text{and} \quad \boldsymbol{Q}(\boldsymbol{X},t)\cdot\boldsymbol{N}(\boldsymbol{X}) = Q_N(\boldsymbol{X},t)\;\forall\boldsymbol{X}\in\partial_q\mathcal{B}. \tag{6.14}$$

The boundary of the domain $\partial\mathcal{B}$ is separated into a non-contact set $\partial_t\mathcal{B}$ in which general heat fluxes Q_N are applied, and into a contact part $\partial_c\mathcal{B}$ with dominant heat conduction Q_c, both of which fulfill $\partial\mathcal{B} = \partial_\Theta\mathcal{B}\cup\partial_q\mathcal{B}\cup\partial_c\mathcal{B} \wedge \partial_\Theta\mathcal{B}\cap\partial_q\mathcal{B}\cap\partial_c\mathcal{B} = \emptyset$. Due the applied operator split scheme, the displacement is constant in the thermal solution phase $\Delta\boldsymbol{u} = \boldsymbol{0}$ and therefore the boundary separation does not change throughout a load step.

The internal heat flux in the material is calculated via

$$\boldsymbol{Q} = -k_{\Theta 0}(\Theta)\boldsymbol{C}^{-1}\cdot\text{Grad}\Theta \text{ with } k_{\Theta 0}(\Theta) = [1-\omega_k(\Theta-\Theta_0)], \tag{6.15}$$

which depicts a linear temperature dependence of the thermal conductivity with a softening parameter ω_k. The heat flux into the ambient air is computed with

$$Q_N = \gamma_{\text{env}}(\Theta-\Theta_{\text{env}}), \tag{6.16}$$

at non-contact surfaces, where γ_{env} is a convection coefficient and Θ_{env} is the environmental temperature. The heat flux in the contact zone Q_c defined in (4.20) accounts for conductive heat transfer over the contacting asperities, and for mechanical dissipation due to friction loss and viscous dissipation. It is assumed that the dissipation is completely transferred into a heat flux, of which only a fraction $\rho_{\mathcal{D}}$ enters the tire whilst the remainder $1-\rho_{\mathcal{D}}$ is transferred into the road. In this thesis, the heat up of the road surface is neglected due to the high traveling speed of the tire. Analogous to the convective heat transport, the heat conduction coefficient is also assumed to be constant for the sake of simplicity.

6.1.3 Advective transport of material history

The final step in the staggered approach for the treatment of the present thermo-viscoelastic rolling contact problem is the advective transport of material history, see [Ziefle, 2007]. In this phase the *Eulerian* part $\frac{\partial \boldsymbol{\alpha}_\mathrm{v}}{\partial t}\big|_{\boldsymbol{X}} + \mathrm{Grad}\boldsymbol{\alpha}_\mathrm{v} \cdot \boldsymbol{w} = 0$ of the material time derivative (6.1) is computed in order to enable a time-discrete evaluation of the material history evolution (3.45) in the next load step. Therefore, the current values of the deviatoric part of Green-Lagrange strain $\bar{\boldsymbol{E}}$, which yields the stretch rate $\dot{\bar{\boldsymbol{E}}}$, and the internal variables $\boldsymbol{\alpha}_\mathrm{v}^{(i)}$ for each *Maxwell-element* are transported by an angular increment $\Delta\phi$. In addition to the transport problem in the bulk material, the penetration d_N and the internal variables $h_N^{(i)}$ and $h_T^{(i)}$ (5.53) describing the viscoelastic material response of the tread block in terms of the constitutive contact model have to be transported along the contact surface as well.

Before solving the transport problem, a L^2-projection onto to the nodes is performed for all local material history quantities $(\bullet)$, which are calculated at the integration points during the mechanical phase. The advective transport problem for the nodal values reads

$$\left.\frac{\partial(\bullet)}{\partial t}\right|_{\chi} + \frac{\partial(\bullet)}{\partial \chi} \cdot \frac{\partial \chi}{\partial t} = \mathbf{0}. \tag{6.17}$$

Following [Ziefle, 2007], this transport problem is treated with a *time-discontinuous Galerkin method* (TDG-method). This technique is based on the idea that the transported quantity $(\bullet)$ can be discontinuous at the endpoints of time-intervals (temporal nodes). In order to illustrate this approach, the integration over the current time interval $[t_n, t_{n+1}]$, which is the successive interval of $[t_{n-1}, t_n]$, is observed. Here, the discontinuity at t_n is described by the jump operator $[\![\bullet]\!] = \bullet^+ - \bullet^-$, where $\bullet^-$ is the nodal value at the end of the last time interval and $\bullet^+$ denotes the value at the beginning of the current interval. Now, the aim is to calculate the integral over the current time interval whilst minimizing the jump at t_n. Here, the value $\bullet^-$ is known from the last solution.

In order to obtain this solution, a temporal shape function η is introduced to discretize the time interval. The introduction of this shape function in combination with the definition of the jump yields the weak form of the advection equation

$$\int_{\mathcal{T}_n} \int_{\mathcal{B}} \eta^n \left(\frac{\partial(\bullet)}{\partial t} + \frac{\partial(\bullet)}{\partial \chi} \cdot \frac{\partial \chi}{\partial t} \right) \mathrm{d}t \, \mathrm{d}V + \int_{\mathcal{B}} \eta^{n-1} \left(\bullet^+ - \bullet^- \right) \mathrm{d}V = \mathbf{0}, \tag{6.18}$$

where η^{n-1} denotes the shape function value at t_n, and the second term can be regarded as a residual. Note that the discretization of this problem results in an equation system sized $n_\mathrm{space} \times n_\mathrm{time}$.

6.2 Numerical examples

In this chapter, the application of the developed constitutive contact model, see subsection 5.1.3, is demonstrated in coupled thermo-viscoelastic rolling resistance calculations of solid rubber wheels and air-inflated radial tires. In a first example, the convergence of the calculated rolling resistance in dependence of angular increment size is studied for a rubber wheel. Then, the influence of surface roughness on the rolling resistance is quantified for this rubber wheel. In the last example, the influence of surface roughness on the rolling resistance is investigated for a large scale radial tire model.

Before analyzing the results of these calculations, some preliminary information regarding term definitions are given as well as a summary of the computation algorithm. A good overview of basic rolling contact phenomena such as slip, traction, and rolling resistance can be obtained from the textbook by [Johnson, 1985].

In the following tractive rolling contact simulations, a measure is required for the classification of different driving states (acceleration, free-rolling, braking and cornering). Therefore, the global slip factor is defined as

$$\boldsymbol{s}_0 = \frac{\boldsymbol{v}_r - \boldsymbol{\omega} \times \boldsymbol{r}_0}{|\boldsymbol{\omega} \times \boldsymbol{r}_0|}, \tag{6.19}$$

which prescribes a percentile difference of convective velocities. Here, $|\boldsymbol{\omega} \times \boldsymbol{r}_0| = \omega r_0$ is the convective velocity in the circumferential direction $\boldsymbol{a}_1$ of the undeformed tire that rotates around a central axis. The global slip factor consists of circumferential slip

$$s_c = \frac{\boldsymbol{v}_r \cdot \boldsymbol{a}_1 - \omega r_0}{\omega r_0}, \text{ with } \begin{cases} < 1, & \text{acceleration slip} \\ = 0, & \text{free rolling} \\ > 1, & \text{braking slip} \end{cases} \tag{6.20}$$

(6.21)

and lateral slip s_l in the direction $\boldsymbol{a}_2$ with

$$s_l = \frac{\boldsymbol{v}_r \cdot \boldsymbol{a}_2}{\omega r_0}, \text{ with } \begin{cases} \neq 0, & \text{cornering} \\ = 0, & \text{straight rolling.} \end{cases} \tag{6.22}$$

Furthermore, the road velocity vector can be expressed in terms of a slip-angle α_s as

$$\boldsymbol{v}_r = v_r(\cos\alpha_s \boldsymbol{a}_1 + \sin\alpha_s \boldsymbol{a}_2), \text{ with } v_r = \|\boldsymbol{v}_r\|. \tag{6.23}$$

In order to solve the nonlinear rolling contact problem and to gain better numerical convergence, the applied loading and displacement boundary conditions are separated into increments, which are applied in load steps. The global solution is then obtained in the following solution phases:

1. Initialization phase:
   - Apply inflation pressure load
   - Apply angular velocity ω in order to calculate inertia effects
2. Frictionless, unilateral contact phase:
   Apply vertical displacement boundary conditions in n_{vert} increments
3. Tangential contact phase:
   - Calculate stick state
   - Apply prescribed slip factor in n_{slip} increments
4. Material history evolution:
   - Calculate advective transport of internal variables using n_{adv} angular increments per revolution
   - Convergence check: If $\left\|\dot{\boldsymbol{A}}_{\mathrm{v}}\right\|_{\max} < tol$ steady state is reached

In every load step of these solution phases, the complete algorithm for the solution of the mathematical problem stated in section 6.1 is executed. Therein, the advective transport problem is treated with an angular increment size of

$$\Delta\phi = \frac{2\pi}{n_{adv}}, \text{ with a time increment size of } \Delta t = \frac{2\pi}{\omega n_{adv}}. \tag{6.24}$$

Due to this treatment, the number of load increments n_{vert} and n_{slip} does not affect the final solution and the rolling resistance by varying time step sizes. In case of thermoelastic material behavior, this algorithm reduces to the first three phases, and no advective transport problem needs to be solved.

Finally, the rolling resistance is calculated as a torque around the central axis

$$M_R = \int_{\partial_c \mathcal{B}} P(\boldsymbol{X}) \boldsymbol{X} \cdot \boldsymbol{A}_1 \, \mathrm{d}A, \tag{6.25}$$

which results from the nonsymmetry of the contact pressure distribution. The rolling resistance coefficient is then evaluated via

$$C_{RR} = \frac{M_R}{\|\boldsymbol{r}_0 \times \boldsymbol{F}_N\|}, \tag{6.26}$$

where $\boldsymbol{r}_0$ is the initial radius, and $\boldsymbol{F}_N$ is the axial load.

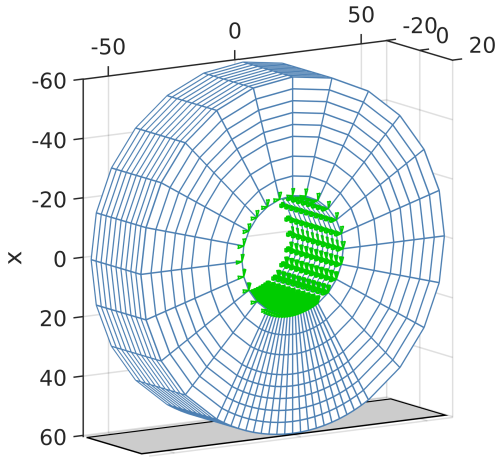

Figure 6.2: Rubber wheel boundary conditions at the central axis (green tetrahedrons).

6.2.1 Convergence study of material history evolution

The numerical convergence of the stationary solution of material history evolution (6.1) strongly depends on the number of angular increments (time steps) n_{adv} per revolution. These increments determine the angular distance over which the material history is transported using the time discontinuous Galerkin method (TDG). Further factors of influence are the mesh size h, the order of temporal shape functions o^t, and the ratio of relaxation times τ_i to angular velocity ω.

The focus of this study lies on the influence of the number of angular increments per revolution, on the order of temporal shape functions used for the TDG, and on the ratio of relaxation time to angular velocity. For this reason, the stationary rolling contact of a solid rubber wheel is observed by varying these parameters of influence, but the mesh size and the material parameters are the same in all calculations.

The discretized model of the solid rubber wheel is depicted in Figure 6.2. Here, the green tetrahedrons mark the bounded nodes of the central axis, where all mechanical and thermal degrees of freedom are held fixed in all following calculations. The wheel has a rectangular cross section, a radius of 60 mm, a width of 30 mm, and a diameter of 40 mm rim. The model is meshed with 3520 8-node brick elements. The exterior surfaces are covered by a total number of 1144 4-node shell elements, which serve as integration domains for the contact interaction and the convective heat transport. All non-contacting surfaces allow for a convective heat flux, and in the contact area (footprint) heat can be transferred into the ground by heat conduction. The material parameters of the applied thermo-viscoelastic material are displayed in Table 5.3.

The convergence of axial torque for the rubber wheel on the flat surface was calculated at angular velocities of $\omega = 5$, 10, 20 and 50 rad/s, see Figure 6.3. It can be observed

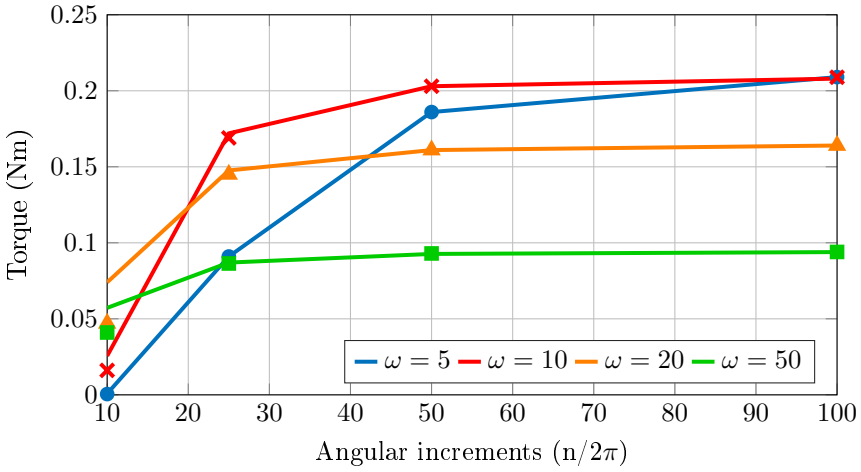

Figure 6.3: Convergence of torque for the solid rubber wheel over angular increments. Solid line: 1st-order TDG, Colored Markers: 2nd-order TDG.

from the results of this study that the necessary number of angular increments in order to obtain convergence increases with decreasing angular velocity here. This comes along with an increase in axial torque for the presented results. In the present case of a single relaxation time, the axial torque, which is related to the rolling resistance via (6.26), has a maximum at a specific angular velocity (frequency) and tends towards zero for $\omega \to 0$ and also for $\omega \to \infty$. A similar behavior has been observed in the numerical study presented in [Suwannachit, 2013]. This effect is induced by the viscous material behavior and depends on the ratio of relaxation time τ (0.01 s in this study) to angular velocity ω. Here, high rolling resistance is caused by a steep gradient in the internal variable field, e.g. the distribution of α_{11} depicted in Figure 6.4. The precise solution of this convective transport problem requires small time steps (angular increment). For large angular increments implicit methods such as the TDG tend to introduce artificial numerical diffusion, which causes a softening of the gradients in the transport phase and results in an underestimation of the rolling resistance. The observed behavior agrees with the findings in [Govindjee and Mihalic, 1998], where a reduced influence of the advective transport was observed for small relaxation times.

These basic effects of the viscoelastic material response in rolling structures are pronounced even more strongly in case of thermo-viscoelastic material behavior. Due to the internal dissipation, the stationary temperature increases (see Figure 6.4 (b)) causing an increase in elastic material stiffness and a reduction of viscous effects.

In addition to the convergence behavior with angular increment size using linear temporal shape functions, the effect of quadratic temporal shape functions on the solution is studied. In general higher order shape functions allow for higher accuracy in the advective

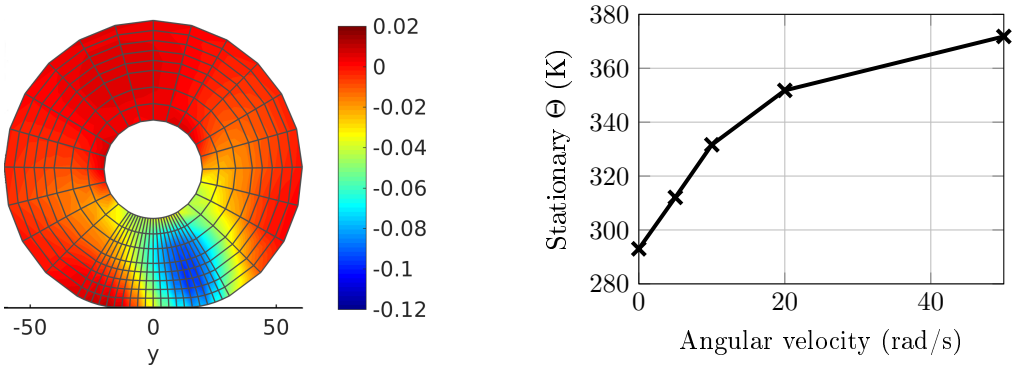

(a) (b)

Figure 6.4: Internal variable distribution α_{11} at $\omega = 5$ (a) and increase in maximum stationary temperature Θ over angular velocity (b).

transport of fields with steep gradients. The results of the second order TDG-solutions for the respective angular velocity and the number of angular increments per revolution are illustrated by the colored markers in Figure 6.3. In this example, the improvement by higher order shape functions is rather small. This contradiction can be explained only by the necessity to capture local sources above the contact zone. In fact, the resulting rolling resistance for large angular increments is smaller than the solution using first order TDG with the same increment size. No improvement of numerical effort (total number of load steps) for obtaining the wheel's rolling resistance could be achieved. For all angular increment sizes the solution required the same total angle, e.g. $\approx$ a half revolution is required at $\omega = 20$ [rad/s] to obtain $\|\Delta \boldsymbol{A}\| < 10^{-8}$. This confirms the dominant dependency on the ratio of relaxation time to angular velocity. Analogously it can be said that if the relaxation time is larger than the period of an entire revolution, the material has not fully relaxed when it is reloaded, which consequently requires more increments (revolutions) to reach the steady state.

6.2.2 Rolling resistance calculation of a rubber-wheel

In this example, the presented numerical framework is applied in order to study the influence of surface roughness on the rolling resistance of a solid rubber wheel. Therefore, the rolling resistance on a flat surface is compared to the results on the rough and the smooth asphalt. This study also aims for the evaluation of the modeling error in this application resulting from the assumption of a uniaxial compression. In this sense, an additional constitutive contact model (CCM) is introduced, which represents the contact behavior of the tread block on a flat surface. This representation is realized with the equivalent

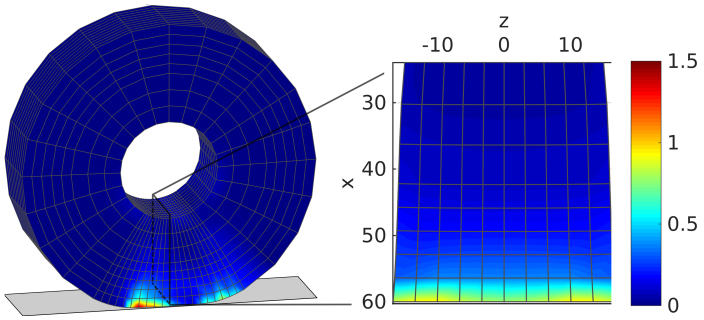

Figure 6.5: Stationary dissipation (mW/mm^3) in the rubber wheel.

stretch-penetration relation

$$\tilde{\lambda}^{1D}(d_N) = 1 - d_N/h_0,$$

in which h_0 is the initial tread height of 20 mm, and the scaling factors for the material parameters are $c_{\text{el}} = c_{\text{visco}} = 1$.

For this study, the same finite element model of a solid rubber wheel with a diameter of 60 mm is studied at an angular velocity of $\omega = 20$ rad/s, see Figure 6.2. Here, the reference solution on the flat surface is calculated using the *Uzawa algorithm* with a gap-tolerance of d_N <0.001 mm. The rough surface contact interaction is represented by adding the constitutive contact model (CCM) to the contact interface. In order to avoid confusion of results obtained by different models the results obtained with the flat surface representation are called CCM flat, those for the smooth asphalt surface CCM smooth and the results on the rough surface are denoted CCM rough.

The reference model is pressed onto the flat surface with a prescribed displacement of 4 mm, which causes a reaction force of $\approx$ 1950 N. The displacements of the other models were adapted so that the same normal reaction force was obtained, resulting in 6 mm for the CCM flat model, 6.7 mm for the CCM smooth model, and 8.5 mm for the CCM rough model. Note that the larger normal displacement to enforce the axial load is caused by the softer contact compliance of the constitutive contact models. Again, heat can be transferred over all free surfaces as well as in the footprint of the wheel. In order to investigate only the influence of the constitutive contact model frictionless rolling is assumed in this study.

In Figure 6.5, the resulting dissipation for the stationary rolling reference model is illustrated for the entire wheel and its central cross section. The highest rates in the structure occur above the leading edge of the contact zone (left of the center). Furthermore, the view into the cross section reveals that this effect concentrates at the lateral edges, at which the material is squeezed outwards due to its quasi-incompressible behavior.

Due to the viscous dissipation, the temperature increases inside the wheel. The resulting temperature distribution is quite homogeneous within the structure, reaching its maximum

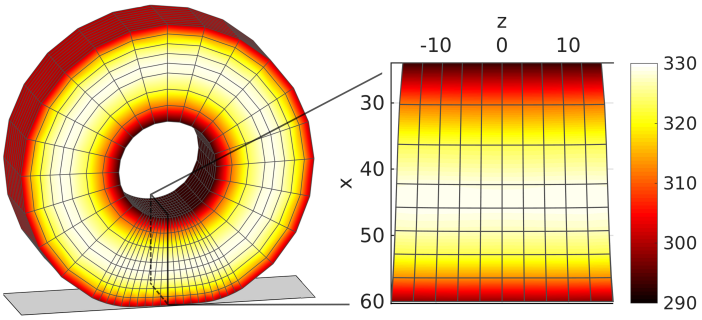

Figure 6.6: Stationary temperature (K) distribution.

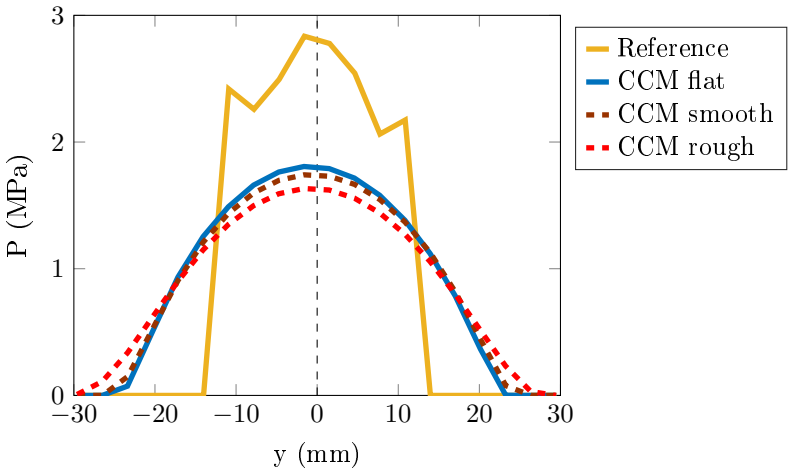

Figure 6.7: Contact pressure distribution in the center of the footprint.

value in the center of the cross section, see Figure 6.6. This fact results from the fixed temperature at the rim and the applied flux boundary conditions on the external surfaces.

The resulting contact pressure distributions in the circumferential center line of the footprint for the different calculations are illustrated in Figure 6.7. It can be observed that the contact area increases due to the application of the constitutive contact model resulting in smaller nominal pressures. The softer response of the CCM model with the flat surface approximation compared to the reference solution results from the neglect of shear deformations. As expected, this effect increases for larger surface roughness, due to the reduction of contact stiffness. Furthermore, all contact pressure distributions are unsymmetric, which results from the viscous effects in the rubber material and yields the rolling resistance. This nonsymmetry of the contact pressure distribution is most pronounced on the rough surface.

The resulting interface temperatures, axial torques, the percentile difference in axial torque compared to the CCM flat model and the rolling resistance coefficient are summarized in Table 6.1. It can be observed that the application of the constitutive contact

Table 6.1: Influence of surface roughness on the stationary response, where the model with the flat surface approximation (CCM flat) serves as base value.

Model	$\Theta_{\max}$ (K)	M_p (Nm)	ΔM_p (%)	C_{RR}
Reference	329.4	0.458	-59.3	0.0017
CCM flat	321.3	1.126	-	0.0113
CCM smooth	320.4	0.809	-28.2	0.0082
CCM rough	318.3	1.202	6,7	0.0123

model in the contact interface results in an increase in rolling resistance, which is plausible as the constitutive material model only depicts normal contact interaction. The softer response of CCM flat model, approximating the flat surface interaction, consequently results in higher rolling resistance compared to reference solution. Furthermore, a positive correlation of rolling resistance and surface roughness is observed in between the smooth and the rough asphalt surface, resulting in a 48% increase of torque. But the comparison of the results for the flat and the smooth surface yields a negative correlation, which is not in accordance with experimental observations. This finding points out a weak point of the current approach to depict the rolling resistance contribution of surface roughness for rubber wheels with small radius. It is assumed that this effect is related to large curvature of this model, which causes a lot of shear strain that is not be depicted by the present approach.

6.2.3 Rolling resistance calculation of a tire

In this last example the rolling resistance contribution of the tread-road interaction is quantified for detailed large scale models of radial tires. The tire model used in this study and its cross section are depicted in Figure 6.8 (a) and (b). Analogous to the previous example the green tetrahedrons illustrate bounded nodes with *Dirichlet boundary conditions* prescribing displacements and temperature. This detailed model is discretized by 12690 8-node brick elements and consists of 16 different material layers, including a steel belt and a fibre-reinforced carcass. The entire model is covered with membrane elements, which serve as integration domains for the contributions of the contact interaction, the inflation pressure and the convective heat flux.

In this study, the inflation pressure is modeled as a perpendicular follower load with a magnitude of 0.32 MPa. Additionally, a vertical displacement of 30 mm is applied at the boundary nodes, which results in an axial load of $\approx$ 10600 N. The angular velocity of the tire is set to 50.95 rad/s, which is equivalent to a traveling speed of $\approx$ 80 km/h. Aiming for the calculation of the influence of surface roughness in this study, 0% global slip was

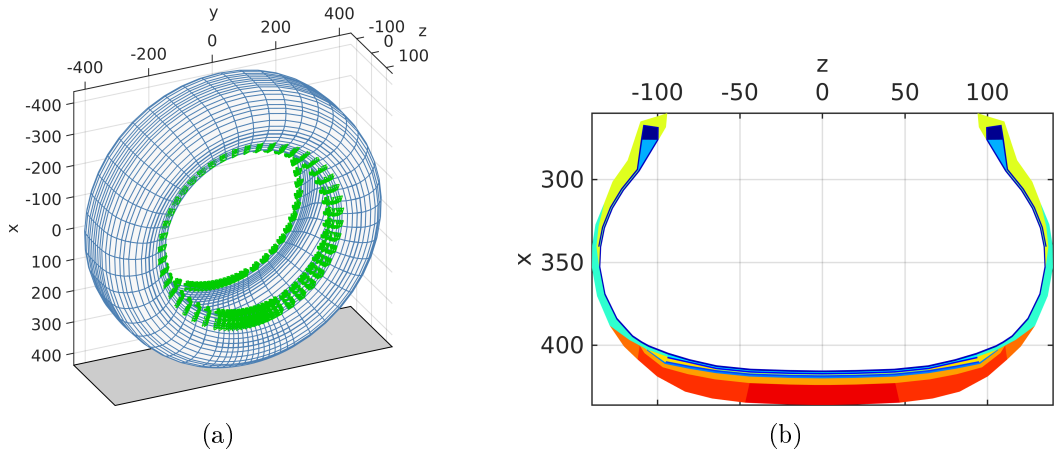

(a) (b)

Figure 6.8: Tire model with boundary conditions (green tetrahedrons) (a) and cross section with the 16 different material groups (b).

prescribed assuming a free rolling trailer tire. For the solution of the thermal problem the rim temperature was kept constant at the initial temperature of 293 K. The heat flux into the ambient (293 K) and the contained air (313 K) was modeled with (6.16) using the heat conduction coefficients presented in [Behnke and Kaliske, 2015], which amount to $\gamma_{\text{env}} = 50\ \text{W}/(\text{m}^2\,\text{K})$ and $\gamma_{\text{cont}} = 20\ \text{W}/(\text{m}^2\,\text{K})$.

The material behavior of the tire rubber was represented using the thermo-viscoelastic material model presented in section 3.2 using the *Mooney-Rivlin model* (3.19) for the thermoelastic response. The viscoelastic material parameters for the different layers were adapted from [Ziefle, 2007; Suwannachit, 2013]. Furthermore, this model was combined with a fraction layer approach to account for fibre-reinforcement, where the mechanical behavior of the fibres was modeled with the exponential law presented in [Polley, 1999], see Appendix C for details. The material parameters for this exponential model were obtained using the *Matlab®Curve Fitting Toolbox*™ approximating the stiffness of the bilinear approach used in [Ziefle, 2007]. The thermal material parameters stem from the works of [Höfer, 2009; Hofstetter, 2004; Suwannachit, 2013]. In this study, rubber friction is modeled with the pressure, temperature and velocity dependent friction law (4.26) presented in [Huemer et al., 2001a].

The calculation was executed with the algorithm described in the beginning of this section. In a first step, the internal pressure was applied, which was followed by an incremental increase of normal displacement and angular velocity (10 steps). Thereafter, contact tractions were calculated using the algorithm suggested in [Ziefle, 2007]. After the calculation of contact tractions, the steady state of the material history evolution was iterated. In this last phase of the algorithm the mechanical and thermal subproblem

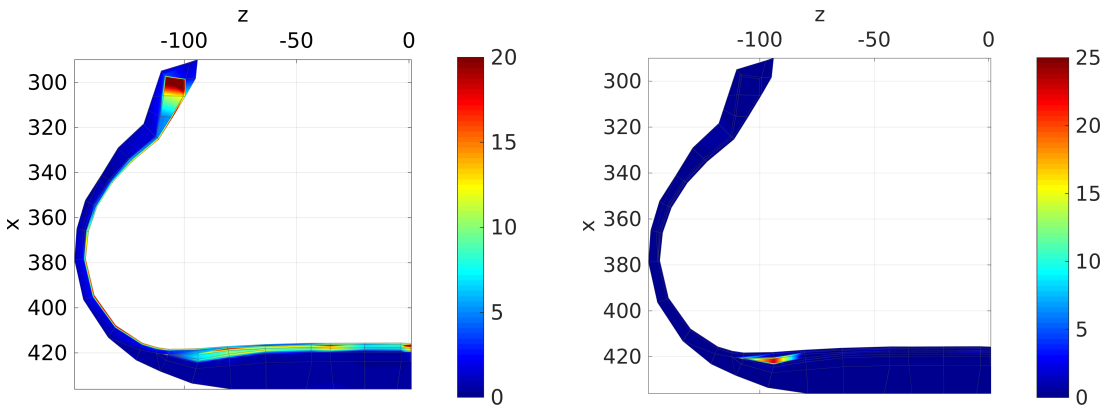

(a) *Von Mises stress* (MPa) (b) Viscous dissipation (mW/mm^3).

Figure 6.9: Distribution of *von Mises stress* (a) and dissipation (b) depicted in the tire cross section above the contact region.

as well as the transport of material history were solved repeatedly until the convergence criterion was fulfilled. In the entire calculation the angular increment for material history transport was 7.2°, which is equivalent to 50 transport steps per revolution.

In order to point out the influence of surface roughness on the thermomechanical behavior, the structural response of the reference model rolling on a flat surface, is observed first. The distribution of the *von Mises stress* in the tire's cross section is illustrated in Figure 6.12 (a), where the maximum value was limited to 20 MPa in order to improve the contrast in the contact zone. The maximum stress value of 35 MPa, which occurs in the bead wire, was not subject of observation in this study. It can be observed that the highest stresses occur in the central steel belt, which is much stiffer than the tire rubber. Therefore, the belt can ensure the flat shape of the tire's tread cap by taking up the inflation pressure and resisting the bending, which results from its connection to the sidewalls that transfer the axial load into the ground. This construction results in a larger contact area and a more homogeneous distribution of contact pressure in the footprint compared to a bias tire.

Due to the much higher material stiffness of the belt, the adjacent rubber layer is subjected to large local strains at high strain rates, which causes a large amount of dissipated energy in each revolution, see Figure 6.12 (b). The mechanical dissipation is transferred into heat and thereby significantly increases the tire's service temperature. The resulting temperature of the tire model and the temperature distribution within the cross section are shown in Figure 6.12. As a consequence of the high local dissipation and the low conductivity of tire rubber compounds the maximum temperature is situated next to the belt. On the exterior and also on the interior surfaces the temperature decreases due to

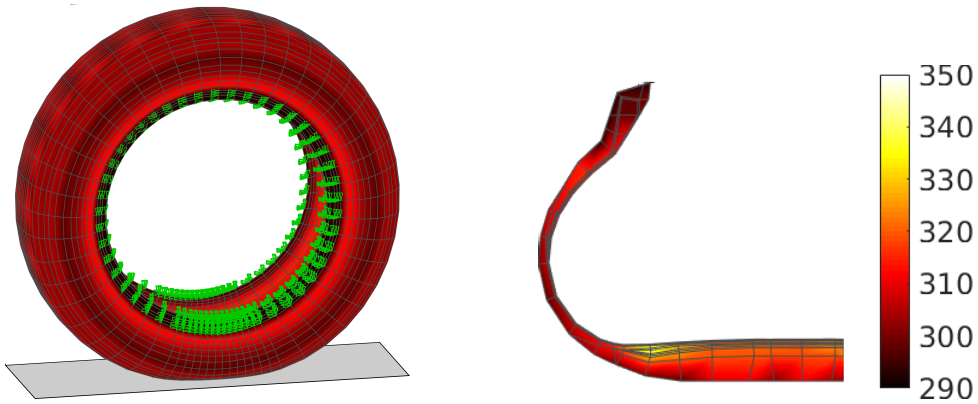

(a) (b)

Figure 6.10: Stationary temperature distribution (K) in the tire structure (a) and in its cross section (b) for the free rolling reference model on a flat surface.

convective heat flux. This result is in good agreement with the combined experimental and numerical study presented in [Behnke and Kaliske, 2015]. Note that only small frictional heating occurs due to the calculation of free rolling.

In order to study the influence of surface roughness on the thermomechanical behavior of the tire, the results using the constitutive contact model representing the solid tread block on the smooth and the rough surface are compared. The smaller contact stiffness of the homogenized contact interaction with the rough surface results in smaller local pressures, which are distributed more homogeneously over a slightly larger footprint than for the smooth surface, see Figure 6.11 (a) and (b). These higher local pressures result in larger maximum circumferential tractions on the smooth asphalt surface, which can be observed in Figure 6.11 (c) and (d). Here, the steep decrease at the trailing edge value results from an exceed of the friction limit. In this area the sliding material causes frictional heating, which is found to be dominant in the contact area, see Figure 6.11 (e) and (f). It follows from the distribution of contact pressure and circumferential traction that also the maximum value of dissipation is larger on the smooth surface.

The resulting temperature distribution in the cross section for both models is illustrated in Figure 6.12. As a result of the additional heat source in the contact interface, the temperature in the tread is larger than in the reference model (see Figure 6.12). In comparison, the temperature on the rough asphalt is higher than on the smooth surface, which results from the dissipation being integrated in the larger footprint.

The results of this comparative study are summarized in Table 6.2. As observed in the results of the rubber wheel example, the application of the constitutive contact model introduces an initial difference of 19.2% rolling resistance (C_{RR}). But in this study, the

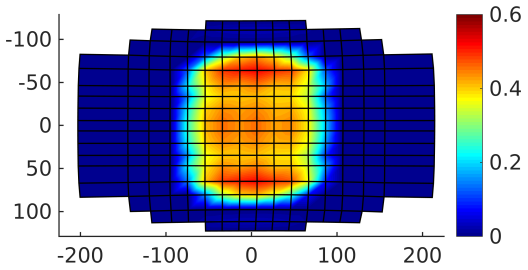

(a) Pressure distribution using CCM smooth (MPa).

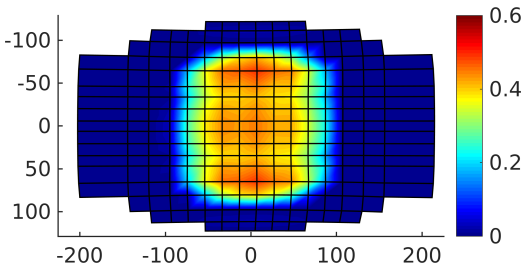

(b) Pressure distribution using CCM rough (MPa).

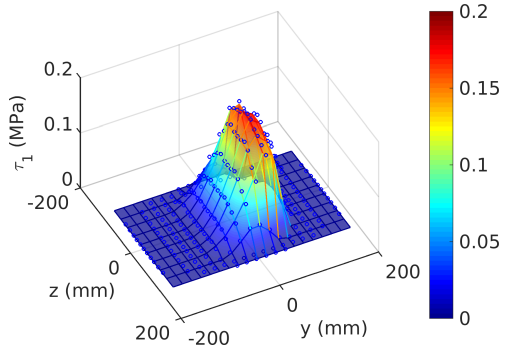

(c) Circumferential traction using CCM smooth (MPa).

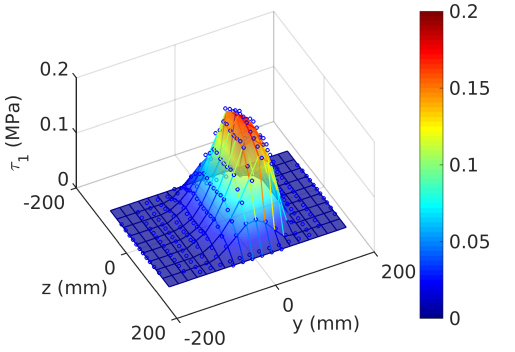

(d) Circumferential traction using CCM rough(MPa).

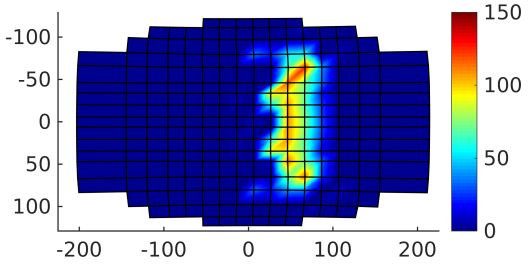

(e) Interface dissipation using CCM smooth (mW/mm^2).

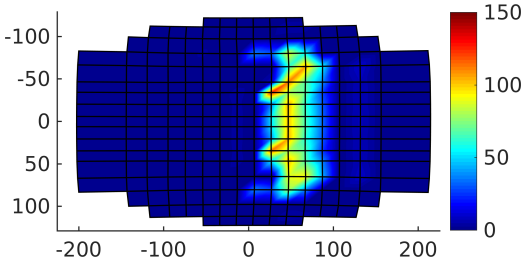

(f) Interface dissipation using CCM rough (mW/mm^2).

Figure 6.11: Contact behavior of the free rolling tire on the smooth and the rough asphalt surface.

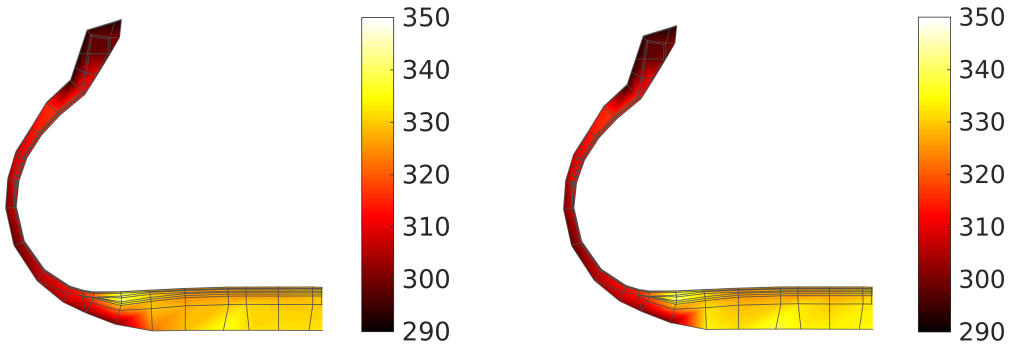

(a) (b)

Figure 6.12: Stationary temperature distribution (K) in the cross section of the tire rolling on the smooth (a) and on the rough asphalt (b).

Table 6.2: Influence of surface roughness on the stationary response, where the model with the flat surface approximation (CCM flat) serves as base value.

Model	$\Theta_{\max}$ (K)	$M_p(Nm)$	ΔM_p (%)	C_{RR}
Reference flat	341.7	30.8	-23.2	0.0067
CCM flat	340.2	40.1	-	0.0083
CCM smooth	341.7	41.8	4.2	0.0087
CCM smooth grooved	341.5	41.8	4.2	0.0087
CCM rough	342.1	45.9	14.5	0.0094
CCM rough grooved	342.2	46.7	16.5	0.0095

expected positive correlation of surface roughness and the tire's rolling resistance can be observed. Comparing the results of the smooth surface with those for the flat surface model a small increase in rolling resistance can be observed, which results from the relatively flat topology. The resulting difference of rolling resistance of 8% (C_{RR}) between the rough and the smooth asphalt surface is in good agreement with the measured range of 8-10% difference in rolling resistance presented in [van Haaster et al., 2015] and also with those results published in [Willis et al., 2014]. Furthermore, an increase of rolling resistance for the grooved tread block on the rough road surface can be observed. These results demonstrate the capability of the developed approach to quantify the rolling resistance contribution of the tread layer in large scale applications and also to recognize the influence of different tread shapes.

In future research this approach can be combined with the anisotropic continuum model, presented in [Kaliske and Timmel, 2005], in order to account also for shear deformations of the structured tread.

7 Conclusion and Outlook

Coupled thermomechanical finite element calculations of rolling tires can create detailed insight into material phenomena occurring at service conditions. These findings are of crucial importance for tire manufacturers aiming to optimize tire designs for their intended application, especially for the reduction of rolling resistance. Frameworks formulated in *Arbitrary Eulerian Lagrangian kinematics* have proven to be highly efficient for these computations. However, this kinematic description does not allow for a direct application of algorithms developed in *Lagrangian kinematics* in order to take into account inelastic material behavior and friction. Handling these difficulties is thus a challenging task in the development of tire computation frameworks. In this context, taking into account the rolling resistance contribution of tread-road interaction into macroscale (mm; cm) computations has been an unsolved issue. This contribution results from the penetration of the tire's tread blocks by the mesoscale (mm) asperities of the rough road surface, causing large strains at high strain rates.

In this thesis, a one-dimensional homogenized constitutive contact model has been developed that represents the stochastic average thermo-viscoelastic structural response of a three-dimensional tread block in unilateral frictionless contact with a mesoscale random rough road surfaces in the context of finite deformations. Its application in coupled thermo-viscoelastic rolling resistance calculations allows for a quantification of the influence of surface roughness on rolling resistance, which is demonstrated for tractive stationary rolling contact of solid rubber wheels and air-inflated radial tires.

The stochastic average tread-road interaction was identified for a solid rubber and a grooved tread block model, which were brought into contact with a rough and a smooth asphalt surface. The measured raw data sets of these road surfaces were transferred into a spectral representation using *discrete Fourier transform*. A bandpass filter was then applied to the resulting frequency spectrum in order to remove low-frequency macroscale waviness and high-frequency microscale (μm) oscillations, as the focus was put on the rolling resistance contribution that results from mesoscale roughness. The solution of the random rough surface contact problem was achieved by a *Monte Carlo integration* over uniformely distributed surface locations. In that study the bulk material of the tread blocks was modeled quasi-incompressible in combination with a viscoelastic *extended tube model*.

The basic idea for the constitutive contact model lies in the identification of an equivalent

kinematics based on the volume average stretch of the tread block as function of prescribed penetration, which is dominated by uniaxial contributions. With this equivalent stretch-penetration relation the pressure and volume average dissipation (heat flux) of the tread block in the coupling interface can be evaluated directly from the constitutive material model of the treads bulk material, assuming a unilateral, incompressible compression test. The accuracy of this approach in depicting uni-lateral contact scenarios and the preservation of external energy in the load cycle, has been verified with full scale numerical calculations, see section 5.4.

The homogenized stochastic average interaction of the tread with the rough and the smooth measured road surface has been included into the thermomechanical framework for the stationary rolling contact, presented in [Suwannachit, 2013]. In order to account for tractive rolling, this framework was enhanced with the approach presented in [Ziefle, 2007], proving its compatibility with arbitrary phenomenological models for rubber friction. The resulting program environment allowed for rolling resistance calculation of rubber wheels and air-inflated radial tires accounting for thermo-viscoelastic effects in the structure, energy dissipation in the tread-road interface, and frictional heating. A comparison of the calculated rolling resistances for the rough and the smooth asphalt quantified the influence of surface roughness to increase by $\approx 8\%$, which is in good agreement with the studies presented in [van Haaster et al., 2015]. These studies measured an influence of surface roughness of $8 - 10\%$. Additionally, the softer contact response of the grooved tread blocks lead to an increase in rolling resistance of 1% on the rough asphalt. According to these results, the presented rolling resistance calculation approach enables the manufacturer to evaluate and to compare different tread designs. By means of this, the description of homogenized tread-road interaction presented in this thesis can yield more detailed insight into the multi-scale processes occurring within the tire, which is necessary for the optimization of future tire designs to suit their intended application.

The next step in elaborating the outcomes of this thesis is seen in the combination with the anisotropic continuum model presented in [Kaliske and Timmel, 2005] in order to represent both the unilateral rough surface contact as well as the shear deformation of the tread structure. Furthermore, the efficiency of the evaluation of the rough surface contact problem can be significantly increased by using *Multi-Level Monte Carlo methods*, which optimize the cost balancing of reducing stochastic and discretization error, see [Chernov and Bierig, 2013]. The solution of the rough surface contact problem also requires a more robust contact constraint enforcement algorithm, such as the *Augmented Lagrangian multiplier* formulation presented in [Pietrzak and Curnier, 1999], which yields a C^1-continuous contact potential.

A Calculation of tangent matrices

In this chapter the calculation of material tangent operators is presented, which are necessary to solve the nonlinear mechanical problems (3.50) and (6.4) using the *Newton-Raphson method*. For further information on the calculus the reader is referred to the textbook by [Holzapfel, 2000], which provides detailed descriptions of the derivations and their results.

Due to the introduction of the thermally expanded intermediate configuration (see subsection 2.1.1), the enforcement of the quasi incompressible material behavior differs from the formulation presented in [Suwannachit, 2013]. In the constitutive material model presented in section 3.2, the contribution of the volumetric penalty function (3.16) is calculated via

$$\frac{\partial U^{\infty}(J_M)}{\partial \boldsymbol{C}} = \frac{\partial U^{\infty}(J_M)}{\partial J_M}\frac{\partial J_M}{\partial \boldsymbol{C}_M}\frac{\partial \boldsymbol{C}_M}{\partial \boldsymbol{C}} \tag{A.1}$$

using

$$\frac{\partial J_M}{\partial \boldsymbol{C}_M} = 0.5 J_M {\boldsymbol{C}_M}^{-1}, \frac{\partial \boldsymbol{C}_M}{\partial \boldsymbol{C}} = \varphi_{\Theta}^{-\frac{2}{3}}\mathbf{1}, \boldsymbol{C}_M^{-1} = \varphi_{\Theta}(\Theta)^{\frac{2}{3}}\boldsymbol{C}^{-1}. \tag{A.2}$$

In the context of the applied isentropic operator split scheme (see section 3.4), the total derivative of stress (material tangent) is calculated via

$$\mathrm{d}\boldsymbol{S} = 2\frac{\partial \boldsymbol{S}}{\partial \boldsymbol{C}} : \frac{1}{2}\mathrm{d}\boldsymbol{C} + \frac{\partial \boldsymbol{S}}{\partial \Theta} : \mathrm{d}\Theta, \tag{A.3}$$

which results in the material tangent. In this phase, the entropy is assumed to be constant and therefore its rate must vanish

$$\mathrm{d}s = 2\frac{\partial s}{\partial \boldsymbol{C}} : \frac{1}{2}\mathrm{d}\boldsymbol{C} + \frac{\partial s}{\partial \Theta} : \mathrm{d}\Theta \stackrel{!}{=} 0, \tag{A.4}$$

which yields the thermal tangent modulus

$$\mathrm{d}\Theta = \left(-2\frac{\partial s}{\partial \boldsymbol{C}} : \frac{1}{2}\mathrm{d}\boldsymbol{C}\right)\left(\frac{\partial s}{\partial \Theta}\right)^{-1}. \tag{A.5}$$

For the presented thermo-viscoelastic material model the derivative of stress with respect to the Cauchy-Green tensor is calculated via

$$\frac{\partial \boldsymbol{S}}{\partial \boldsymbol{C}} = 4\frac{\partial^2 U^{\infty}(J_M,\Theta)}{\partial \boldsymbol{C}\partial \boldsymbol{C}} + 4\frac{\partial^2 W^{\infty}(\bar{\boldsymbol{C}},\Theta)}{\partial \boldsymbol{C}\partial \boldsymbol{C}} + 4\frac{\partial^2 \sum_i \Upsilon(\alpha_i,\Theta)}{\partial \boldsymbol{C}\partial \boldsymbol{C}} = \mathbb{C}_{ISO} + \sum_i \mathbb{C}_{\boldsymbol{\alpha}_{\mathrm{v}}^{(i)}}, \tag{A.6}$$

and the derivative of stress with respect to temperature is defined by

$$\frac{\partial \boldsymbol{S}}{\partial \Theta} = 2\frac{\partial^2 U^{\infty}(J_M,\Theta)}{\partial \boldsymbol{C}\partial \Theta} + 2\frac{\partial^2 W^{\infty}(\bar{\boldsymbol{C}},\Theta)}{\partial \boldsymbol{C}\partial \Theta}. \tag{A.7}$$

Finally, the derivative entropy with respect to the Cauchy-Green tensor yields

$$\frac{\partial s}{\partial \boldsymbol{C}} = \frac{3\alpha_{\Theta 0}\kappa_0}{4}(J_M^5 + J_M^{-5})\boldsymbol{C}^{-1} - \frac{\partial^2 U^\infty(J_M,\Theta)}{\partial\Theta\partial\boldsymbol{C}} - \frac{\partial^2 W^\infty(\bar{\boldsymbol{C}},\Theta)}{\partial\Theta\partial\boldsymbol{C}} - \frac{\partial^2 T^\infty(\Theta)}{\partial\Theta\partial\boldsymbol{C}}, \tag{A.8}$$

where the last term vanishes due to the independence of deformation $\boldsymbol{C}$. With these definitions the thermomechanical material tangent operator is computed by

$$\mathbb{C}_{ISE} = \mathbb{C}^\infty + \mathbb{C}_\Upsilon + \left(\frac{\partial s}{\partial\Theta}\right)^{-1}\frac{\partial \boldsymbol{S}}{\partial\Theta} \otimes -2\frac{\partial s}{\partial \boldsymbol{C}} \tag{A.9}$$

B Rough surface contact data

In Table B.1 the coefficients for the polynomial approximation of the stretch-penetration relation $\tilde{\lambda}^{1D}(\bar{d}_N) = \sum_i a_i d_N^i$ are given. Note that $a_0 = 1$ is predefined in order to obtain $\tilde{\lambda}^{1D}(0) = 1$ and $P(0) = 0$. On the flat surface the stretch penetration relation is linear and therefore $a_1 = -1/h_0$ is defined by the initial height of the tread block h_0.

	a_1	a_2	a_3	a_4	a_5	a_6	a_7
Flat surface							
Solid tread	-0.05	0	0	0	0	0	0
Smooth asphalt							
Solid tread	1.921e-23	-3.063e-2	9.383e-3	-1.413e-3	1.091e-4	-4.129e-6	6.067e-8
Grooved tread	-6.383e-21	-2.910e-2	8.427e-3	-1.186e-3	8.491e-5	-2.952e-6	3.954e-8
Rough asphalt							
Solid tread	-6.768e-4	-2.961e-3	-8.468e-4	1.697-4	-1.028e-5	2.0444e-7	0
Grooved tread	-6.799e-4	-2.265e-3	-1.035e-3	1.898e-4	-1.120e-5	2.197e-7	0

Table B.1: Amplitudes of the fitting polynomial stretch-penetration relation

C Fibre reinforcement

The fibre reinforcement of tire rubber applied in section 6.1 is modeled by a homogenized anisotropic volume fraction approach

$$\Psi = \phi_F \Psi_{\text{Fiber}} + (1 - \phi_F)\Psi_{\text{Mat}}, \tag{C.1}$$

where the total strain energy density is the sum of fibre Ψ_{Fiber} and matrix Ψ_{Mat} contribution weighted by the volume fraction ϕ_F of the cord layer. The embedded fibres are assumed to have much higher stiffness than the surrounding rubber matrix in the tensile regime. However, they buckle under compression, resulting in a low stiffness, which is neglected in this study. In order to obtain a smooth transition between tension and compression, the exponential model by [Polley, 1999]

$$\Psi_F = \frac{a}{2b^2}(\exp(b(\lambda_F - 1)) - b\lambda_F) \text{ with } \lambda_F = \boldsymbol{C} : \boldsymbol{A}_F, \tag{C.2}$$

is applied. The actual fibre stretch λ_F is evaluated in the tangential fibre direction $\boldsymbol{t}$ via the structure tensor $\boldsymbol{A} = \boldsymbol{t}^{\mathrm{T}}\boldsymbol{t}$, and a and b are material parameters. The stress is then calculated by

$$\boldsymbol{S}_F = \frac{a}{2b}(\exp(b(\lambda_F - 1)) - 1)\boldsymbol{A}_F, \tag{C.3}$$

and its consistent tangent yields

$$\Delta\boldsymbol{S}_F = \frac{a}{2}\exp(b(\lambda_F - 1))\boldsymbol{A}_F^{\mathrm{T}}\boldsymbol{A}_F. \tag{C.4}$$

For further information on fiber reinforcement models the reader is referred to [Schröder et al., 2005].

List of Figures

List of Tables

List of Symbols

In this thesis different configurations were introduced in order to describe the tire's motion and the change of thermomechanical state. In order to simplify the mathematical problem formulation, the following notation convention was introduced using distinct super- and subscripts , which is adapted from [Suwannachit, 2013]. In the context of

	Configuration			
	Material	Reference	Thermally expanded	Spatial
Symbol	$\mathcal{B}_0$	$\mathcal{B}$	$\breve{\mathcal{B}}$	$\mathcal{B}_t$
Variables	A_0	A	$\breve{A}$	a
Vectors	$\boldsymbol{N}_0$	$\boldsymbol{N}$	$\breve{\boldsymbol{N}}$	$\boldsymbol{n}$
Operators	GRAD	Grad	Grad_Θ	grad

general homogenization problems and microscale contact homogenization techniques, seesection 5.1, the domain of representative volume element $\mathcal{B}_m$ with its boundary $\partial\mathcal{B}_m$, which is coupling interface. The mesoscale contact homogenization was conducted with a domain Ω_M, which was separated from the macroscale model by introducing the transition area$\partial\Omega_M$. At this interface the homogenized contact behavior is identified, which is denoted with the superscript $\bar{\bullet}$. All equivalent uniaxial quantities to represent this contact behavior in terms of the developed constitutive contact model are denoted $\bullet^{1D}$.

Mathematical operators

d	Total material derivative	Grad	Spatial gradient operator
∂	Partial derivative	Div	Spatial divergence operator
$\dot{\bullet}$	Material time derivative	$\cdot$	Single tensor contraction
Δ	Discrete increment	:	Double tensor contraction
$\| \bullet \|$	Euclidean norm	I, II, III	Invariants of a tensor
$\circ$	Composition operator		

Latin symbols

$\boldsymbol{a}$	Acceleration vector
$\boldsymbol{A}_i$	Tangent vector
$\boldsymbol{A}_{\mathrm{v}}^{(i)}$	Conjugate thermodynamic stress tensor
$\mathcal{B}_m$	Microscale RVE domain
c_p	Isobaric heat capacity
$\boldsymbol{c}$	Convective velocity vector
$\boldsymbol{C}$	*Right Cauchy-Green tensor*
d_N	Normal penetration
$\mathrm{d}V$	Finite volume element
$\mathrm{d}X$	Finite line element
$\boldsymbol{d}$	Symmetric rate of deformation tensor
$\mathcal{D}_{\mathrm{int}}$	Internal dissipation
e	Mass-specific internal energy
$\boldsymbol{E}$	*Green-Lagrange strain*
$\boldsymbol{f}$	Force vector
$\boldsymbol{F}$	Deformation gradient
J	*Jacobian determinant*
k_{cp}	Temperature dependence coefficient of heat capacity
k_Θ	Heat conduction coefficient
$\boldsymbol{L}$	Velocity gradient
m	Mass
$\boldsymbol{N}$	Normal vector
$\boldsymbol{P}$	*First Piola-Kirchhoff stress tensor*
$\mathcal{P}$	Mechanical power
$\boldsymbol{Q}$	Heat flux vector
r	Internal heat source
$\tilde{\boldsymbol{R}}$	ALE rotation tensor
s	Entropy
s_i	Tangential slip
$\boldsymbol{S}$	*Second Piola-Kirchhoff stress tensor*
t	Time
T^∞	Thermal stored energy
$\boldsymbol{T}$	Nominal traction vector
U^∞	Volumetric penalty function
$\boldsymbol{u}$	Displacement vector
$\boldsymbol{v}$	Velocity vector
W	Mechanical work
W^∞	Deviatoric strain energy function
$\boldsymbol{w}$	ALE guiding velocity vector
$\boldsymbol{X}$	Coordinate of a material point

Greek symbols

α_Θ	Thermal expansion coefficient
$\boldsymbol{\alpha}_\mathrm{v}^{(i)}$	Internal variable
γ_Θ	Thermal coupling parameter
γ_env	Surface convection coefficient
Θ	Temperature
κ	Compression modulus
λ	Stretch
μ	Shear modulus
ϱ	Density
$\rho_\mathcal{D}$	Heat flux partition coefficient
$\boldsymbol{\sigma}$	*Cauchy stress tensor*
$\tau_\mathrm{v}^{(i)}$	Relaxation time
Υ	Potential function for viscoelastic overstress
φ_Θ	Thermal extension function
ϕ	Rotation angle
ψ	Mass-specific *Helmholtz free energy*
Ψ	Strain energy function
Ψ_c	Contact strain energy function
$\boldsymbol{\xi}$	Convective coordinates
ω_k	Thermal softening parameter
Ω_M	Domain of the mesoscale model
$\boldsymbol{\omega}$	Angular velocity vector
$\boldsymbol{\Omega}$	Angular velocity tensor

Nomenclature

ALE	Arbitrary Lagrangian Eulerian
CCM . . .	Constitutive contact model
DFT	Discrete Fourier transform
FE	Finite element
FE^2	Coupled multiscale FEM
FEM . . .	Finite element method
$KKT - condition$	Karush-Kuhn-Tucker condition
$NURBS$ . .	Non Uniform Rational Beziér Splines
$QMC - simulation$	*Quasi Monte Carlo simulation*
RCE	Representative contact element
RVE	Representative volume element
TDG	Time discontinuous Galerkin

References

Argyris, J. H., Doltsinis, J., and Doltsinid, J. S. (1981). On the natural formulation and analysis of large deformation coupled thermomechanical problems. *Computer Methods in Applied Mechanics and Engineering*, 25:195–253.

Armero, F. and Simo, J. C. (1992). A new unconditionally stable fractional step method for non-linear coupled thermomechanical problems. *International Journal for Numerical Methods in Engineering*, 35(4):737–766.

Bandeira, A. A., Wriggers, P., and de Mattos Pimenta, P. (2004). Numerical derivation of contact mechanics interface laws using a finite element approach for large 3D deformation. *International Journal for Numerical Methods in Engineering*, 59(2):173–195.

Beyer, R. and Nackenhorst, U. (2014). Thermomechanical contact of rubber-like solids on rough surfaces. *PAMM*, 14(1):231–232.

Behnke, R. and Kaliske, M. (2015). Thermo-mechanically coupled investigation of steady state rolling tires by numerical simulation and experiment. *International Journal of Non-Linear Mechanics*, 68:101–131.

Brinkmeier, M. (2007). *Modellierung und Simulation der hochfrequenten Dynamik rollender Reifen*. Dissertation, Leibniz Universität Hannover.

Castañeda, P. (1996). Exact second-order estimates for the effective mechanical properties of nonlinear composite materials. *Journal of the Mechanics and Physics of Solids*, 44(6):827–862.

Chadwick, P. (1974). Thermo-Mechanics of Rubberlike Materials. *Philosophical Transactions of the Royal Society A: Mathematical, Physical and Engineering Sciences*, 276(1260):371–403.

Chapelle, D. and Bathe, K.-J. (2011). *The Finite Element Analysis of Shells - Fundamentals*. Computational Fluid and Solid Mechanics. Springer, Berlin, Heidelberg, 2. edition.

Chen, W. W. (2013a). Numerical Methods for Elastic Contact Problems. In *Encyclopedia of Tribology*, pages 2449–2454. Springer US, Boston, MA.

Chen, W. W. (2013b). Numerical Thermoelastic Contact Simulation. In *Encyclopedia of Tribology*, pages 2465–2465. Springer US, Boston, MA.

Chernov, A. and Bierig, C. (2013). Convergence analysis of multilevel sample variance estimators in multilevel Monte Carlo Methods and application for random obstacle problems. Technical Report 1309, University of Bonn.

Cullen, J. M., Allwood, J. M., and Borgstein, E. H. (2011). Reducing Energy Demand: What Are the Practical Limits? *Environmental Science & Technology*, 45(4):1711–1718.

De Lorenzis, L. and Wriggers, P. (2013). Computational homogenization of rubber friction on rough rigid surfaces. *Computational Materials Science*, 77:264–280.

De Lorenzis, L., Wriggers, P., and Zavarise, G. (2011). A mortar formulation for 3D large deformation contact using NURBS-based isogeometric analysis and the augmented Lagrangian method. *Computational Mechanics*, 49(1):1–20.

Donea, J., Huerta, A., Ponthot, J.-P., and Rodriguez-Ferran, A. (2004). Arbitrary Lagrangian-Eulerian Methods. In Stein, E., Hughes, T. J., and de Borst, R., editors, *Encyclopedia of Computational Mechanics*, volume 1, chapter 14, pages 1–25. John Wiley & Sons, Ltd, Chichester, UK.

Faria, L. O., Oden, J. T., Yavari, B., Tworzydlo, W. W., Bass, J. M., and Becker, E. B. (1992). Tire Modeling by Finite Elements. *Tire Science and Technology*, 20(1):33–56.

Ganguly, A. and Wadhwa, K. (1997). On Random Variational Inequalities. *Journal of Mathematical Analysis and Applications*, 206(1):315–321.

Geers, M., Kouznetsova, V., and Brekelmans, W. (2010). Multi-scale computational homogenization: Trends and challenges. *Journal of Computational and Applied Mathematics*, 234(7):2175–2182.

Ghoreishy, M. H. R. (2008). A state of the art review of the finite element modelling of rolling tyres. *Iranian Polymer Journal*, 17(8):571–597.

Gonzalez, R. C., Woods, R. E., and Eddins, S. L. (2003). *Digital image processing using Matlab*. Prentice-Hall, Inc., Upper Saddle River, NJ.

Govindjee, S. and Mihalic, P. A. (1998). Viscoelastic Constitutive Relations for the Steady Spinning of a Cylinder. Technical report, Department of Civil Engineering, University of California at Berkeley, Berkeley.

Govindjee, S., Potter, T., and Wilkening, J. (2014a). Cyclic steady states of treaded rolling bodies. *International Journal for Numerical Methods in Engineering*, 99(3):203–220.

Govindjee, S., Potter, T., and Wilkening, J. (2014b). Dynamic stability of spinning viscoelastic cylinders at finite deformation. *International Journal of Solids and Structures*, 51(21-22):3589–3603.

Greenwood, J. A. and Williamson, J. B. P. (1966). Contact of Nominally Flat Surfaces. *Proceedings of the Royal Society A: Mathematical, Physical and Engineering Sciences*, 295(1442):300–319.

Hartmann, S. (2012). Comparison of the multiplicative decompositions F = FQFM and F = FMFQ in finite strain thermo-elasticity. Technical report, Faculty of Mathematics/Computer Science and Mechanical Engineering, Clausthal University of Technology.

Hartmann, S. and Neff, P. (2003). Polyconvexity of generalized polynomial-type hyperelastic strain energy functions for near-incompressibility. *International Journal of Solids and Structures*, 40(11):2767–2791.

Haupt, P. (2002). *Continuum Mechanics and Theory of Materials*. Advanced Texts in Physics. Springer, Berlin, Heidelberg.

Heimes, T. (2005). *Finite Thermoinelastizität: Experimente, Materialmodellierung und Implementierung in die FEM am Beispiel einer technischen Gummimischung*. Dissertation, Universität der Bundeswehr München.

Hoever, C. (2012). *The influence of modelling parameters on the simulation of car tyre rolling losses and rolling noise*. PhD thesis, Chalmers University of Technology, Gothenburg.

Höfer, P. (2009). *Dynamische Eigenschaften technischer Gummiwerkstoffe : Experimente, thermomechanische Materialmodellierung & Implementierung in die FEM*. Dissertation, Universität der Bundeswehr München.

Hofstetter, K. (2004). *Thermo-mechanical simulation of rubber tread blocks during frictional sliding*. PhD thesis, Vienna University of Technology.

Hofstetter, K., Grohs, C., Eberhardsteiner, J., and Mang, H. (2006). Sliding behaviour of simplified tire tread patterns investigated by means of FEM. *Computers and Structures*, 84(17-18):1151–1163.

Holmberg, K., Andersson, P., and Erdemir, A. (2012). Global energy consumption due to friction in passenger cars. *Tribology International*, 47:221–234.

Holzapfel, G. and Simo, J. (1996a). Entropy elasticity of isotropic rubber-like solids at finite strains. *Computer Methods in Applied Mechanics and Engineering*, 132(1-2):17–44.

Holzapfel, G. A. (2000). *Nonlinear solid mechanis: a continuum approach for engineers*. John Wiley & Sons Ltd., Chichester, UK, 1st edition.

Holzapfel, G. A. and Simo, J. (1996b). A new viscoelastic constitutive model for continuous media at finite thermomechanical changes. *International Journal of Solids and Structures*, 33(20-22):3019–3034.

Huemer, T., Liu, W. N., Eberhardsteiner, J., and Mang, H. A. (2001a). A 3D finite element formulation describing the frictional behavior of rubber on ice and concrete surfaces. *Engineering Computations*, 18(3/4):417–437.

Huemer, T., Liu, W. N., Eberhardsteiner, J., Mang, H. A., and Meschke, G. (2001b). Sliding Behavior of Rubber on Snow and Concrete Surfaces. *Engineering Computations*, 18(3/9):458–462.

Johlitz, M., Scharding, D., Diebels, S., Retka, J., and Lion, A. (2010). Modelling of thermo-viscoelastic material behaviour of polyurethane close to the glass transition temperature. *ZAMM*, 90(5):387–398.

Johnson, K. L. (1985). *Contact mechanics*. Cambridge University Press, Cambridge, UK.

Kaliske, M. and Heinrich, G. (1999). An Extended Tube-Model for Rubber Elasticity: Statistical-Mechanical Theory and Finite Element Implementation. *Rubber Chemistry and Technology*, 72(4):602–632.

Kaliske, M. and Timmel, M. (2005). Representation of geometric structural pattern in elastomeric solids by a non-linear anisotropic model. *Plastics, Rubber and Composites*, 34(8):357–364.

Konyukhov, A. and Schweizerhof, K. (2013). *Computational Contact Mechanics*, volume 67 of *Lecture Notes in Applied and Computational Mechanics*. Springer, Berlin, Heidelberg.

Kornhuber, R., Schwab, C., and Wolf, M.-W. (2014). Multilevel Monte Carlo Finite Element Methods for Stochastic Elliptic Variational Inequalities. *SIAM Journal on Numerical Analysis*, 52(3):1243–1268.

Kouznetsova, V. G., Geers, M. G. D., and Brekelmans, W. A. M. (2004). Multi-scale second-order computational homogenization of multi-phase materials: a nested finite element solution strategy. *Computer Methods in Applied Mechanics and Engineering*, 193(48-51):5525–5550.

Laursen, T. (2003). *Computational Contact and Impact Mechanics*. Springer, Berlin, Heidelberg, New York.

Le Tallec, P., Rahier, C., and Le, P. (1994). Numerical models of steady rolling for non-linear viscoelastic structures in finite deformations. *International Journal for Numerical Methods in Engnineering*, 37(7):1159–1186.

Liu, G., (Jane) Wang, Q., and Lin, C. (1999). A Survey of Current Models for Simulating the Contact between Rough Surfaces. *Tribology Transactions*, 42(3):581–591.

Liu, I.-S. (2002). *Continuum Mechanics*. Advanced Texts in Physics. Springer, Berlin, Heidelberg.

Lopez-Pamies, O. and Ponte Castañeda, P. (2003). Second-order estimates for the large-deformation response of particle-reinforced rubbers. *Comptes Rendus - Mecanique*, 331(1):1–8.

Lorenz, B., Persson, B. N. J., Dieluweit, S., and Tada, T. (2011). Rubber friction: Comparison of theory with experiment. *The European Physical Journal E*, 34(12):129.

Louhghalam, A., Tootkaboni, M., and Ulm, F. (2015). Roughness-Induced Vehicle Energy Dissipation: Statistical Analysis and Scaling. *Journal of Engineering Mechanics*, 141(11):04015046.

Lu, S. and Pister, K. (1975). Decomposition of deformation and representation of the free energy function for isotropic thermoelastic solids. *International Journal of Solids and Structures*, 11(7-8):927–934.

Lubliner, J. (2006). *Plasticity Theory*. Dover Publications Inc., Mineola, New York.

Mackerle, J. (1998). Rubber and rubber-like materials, finite-element analyses and simulations: a bibliography (1976-1997). *Modelling and Simulation in Materials Science and Engineering*, 6(2):171–198.

Mackerle, J. (2004). Rubber and rubber-like materials, finite-element analyses and simulations, an addendum: a bibliography (1997–2003). *Modelling and Simulation in Materials Science and Engineering*, 12(5):1031–1053.

Michalowski, R. and Mroz, Z. (1978). Associated and non-associated sliding rules in contact friction problems.

Miehe, C. (2003). Computational micro-to-macro transitions for discretized micro-structures of heterogeneous materials at finite strains based on the minimization of averaged incremental energy. *Computer Methods in Applied Mechanics and Engineering*, 192(5-6):559–591.

Moore, D. F. (1972). *The Friction and Lubrication of Elastomers* International series of monographs on material science and technology, volume 9. Pergamon Press Ltd, Oxford, UK.

Nackenhorst, U. (1993). Zur Berechnung von Rollkontaktproblemen mit der Finite Element Methode. *ZAMM - Journal of Applied Mathematics and Mechanics / Zeitschrift für Angewandte Mathematik und Mechanik*, 73(4-5):363–366.

Nackenhorst, U. (2000). *Rollkontaktdynamik – Numerische Analyse der Dynamik rollender Körper mit der Finite Elemente Methode.* Habilitationsschrift, Universität der Bundeswehr Hamburg.

Nackenhorst, U. (2004). The ALE-formulation of bodies in rolling contact. *Computer Methods in Applied Mechanics and Engineering*, 193(39-41):4299–4322.

Nasdala, L. (2000). *Ein viskoelastisches Schädigungsgesetz für den stationär rollenden Reifen.* Dissertation, Universität Hannover.

Nasdala, L., Kaliske, M., Becker, A., and Rothert, H. (1998). An efficient viscoelastic formulation for steady-state rolling structures. *Computational Mechanics*, 22(5):395–403.

Oden, J. T. and Lin, T. L. (1986). On the general rolling contact problem for finite deformations of a viscoelastic cylinder. *Computer Methods in Applied Mechanics and Engineering*, 57(3):297–367.

Oden, J. T., Lin, T. L., and Bass, J. M. (1988). A Finite Element Analysis of the General Rolling Contact Problem for a Viscoelastic Rubber Cylinder. *Tire Science and Technology*, 16(1):18–43.

Özdemir, I., Brekelmans, W., and Geers, M. (2008). Computational homogenization for the thermo-mechanical analysis of heterogeneous solids. *Computer Methods in Applied Mechanics and Engineering*, 198(3-4):602–613.

Persson, B. (2006a). Contact mechanics for randomly rough surfaces. *Surface Science Reports*, 61(4):201–227.

Persson, B. N. J. (2001). Theory of rubber friction and contact mechanics. *Journal of Chemical Physics*, 115(8):3840–3861.

Persson, B. N. J. (2006b). Rubber friction: role of the flash temperature. *Journal of physics: Condensed matter*, 18(32):7789–7823.

Pietrzak, G. and Curnier, A. (1999). Large deformation frictional contact mechanics: continuum formulation and augmented Lagrangian treatment. *Computer Methods in Applied Mechanics and Engineering*, 177(3-4):351–381.

Polley, A. (1999). *Zur Korrelation von Simulationsrechnungen und Ausfallphänomenen bei Rollbalgluftfedern*. Dissertation, Universität Hannover.

Popov, V. L., Voll, L., Li, Q., Chai, Y. S., and Popov, M. (2014). Generalized law of friction between elastomers and differently shaped rough bodies. *Scientific Reports*, 4:3750.

Puglisi, G. and Saccomandi, G. (2016). Multi-scale modelling of rubber-like materials and soft tissues: an appraisal. *Proceedings of the Royal Society A: Mathematical, Physical and Engineering Science*, 472(2187):20160060.

Reinelt, J. and Wriggers, P. (2010). Multi-scale Approach for Frictional Contact of Elastomers on Rough Rigid Surfaces. In *Lecture Notes in Applied and Computational Mechanics*, pages 53–94. Springer, Berlin, Heidelberg.

Schröder, J., Neff, P., and Balzani, D. (2005). A variational approach for materially stable anisotropic hyperelasticity. *International Journal of Solids and Structures*, 42(15):4352–4371.

Suwannachit, A. (2013). *Thermomechanical Analysis of Tire Rubber Compounds in Rolling Contact*. Dissertation, Leibniz Universität Hannover.

Suwannachit, A. and Nackenhorst, U. (2013). A Novel Approach for Thermomechanical Analysis of Stationary Rolling Tires within an ALE-Kinematic Framework. *Tire Science and Technology*, 41(3):174–195.

Temizer, I. and Wriggers, P. (2008). A multiscale contact homogenization technique for the modeling of third bodies in the contact interface. *Computer Methods in Applied Mechanics and Engineering*, 198(3-4):377–396.

Temizer, I. and Wriggers, P. (2010a). Inelastic analysis of granular interfaces via computational contact homogenization. *International Journal for Numerical Methods in Engineering*, 84(8):883–915.

Temizer, I. and Wriggers, P. (2010b). Thermal contact conductance characterization via computational contact homogenization: A finite deformation theory framework. *International Journal for Numerical Methods in Engineering*, 83(1):27–58.

Temizer, I. and Zohdi, T. I. (2007). A numerical method for homogenization in non-linear elasticity. *Computational Mechanics*, 40(2):281–298.

Treloar, L. R. G. (1949). *The physics of rubber elasticity*. Oxford University Press.

van Haaster, B., Worrell, E., F. Fortuin, J., and van Vliet, W. (2015). Potential Energy Savings by Reducing Rolling Resistance of Dutch Road Pavements. *Journal of Materials in Civil Engineering*, 27(1):04014101.

Williams, M. L., Landel, R. F., and Ferry, J. D. (1955). The Temperature Dependence of Relaxation Mechanisms in Amorphous Polymers and Other Glass-forming Liquids. *American Chemical Society*, 77:3701–3707.

Willis, J. R., Robbins, M. M., and Thompson, M. (2014). Effects of Pavement Properties on Vehicular Rolling Resistance: a Literature Review. Technical report, National Center for Asphalt Technology (NCAT), Auburn University, Alabama.

Willner, K. (2003). *Kontinuums- und Kontaktmechanik*. Springer, Berlin, Heidelberg.

Wollny, I. and Kaliske, M. (2013). Numerical simulation of pavement structures with inelastic material behaviour under rolling tyres based on an arbitrary Lagrangian Eulerian (ALE) formulation. *Road Materials and Pavement Design*, 14(1):71–89.

Wriggers, P. (2006). *Computational Contact Mechanics*. Springer, Berlin, Heidelberg, 2nd edition.

Wriggers, P. (2008). *Nonlinear Finite Element Methods*. Springer, Berlin, Heidelberg.

Wriggers, P. and Miehe, C. (1994). Contact constraints within coupled thermomechanical analysis – A finite element model. *Computer Methods in Applied Mechanics and Engineering*, 113(3-4):301–319.

Wriggers, P. and Nettingsmeier, J. (2007). Homogenization and Multi-Scale Approaches for Contact Problems. In *Computational Contact Mechanics*, pages 129–161. Springer, Vienna.

Yastrebov, V. A. (2013). *Numerical Methods in Contact Mechanics*. John Wiley & Sons, Inc., Hoboken, NJ.

Zavarise, G., Borri-Brunetto, M., and Paggi, M. (2004). On the reliability of microscopical contact models. *Wear*, 257(3-4):229–245.

Ziefle, M. (2007). *Numerische Konzepte zur Behandlung inelastischer Effekte beim reibungsbehafteten Rollkontakt*. Dissertation, Leibniz Universität Hannover.

Ziefle, M. and Nackenhorst, U. (2008). Numerical techniques for rolling rubber wheels: treatment of inelastic material properties and frictional contact. *Computational Mechanics*, 42(3):337–356.

Zinatbakhsh, S., Markert, B., and Ehlers, W. (2010). On the General Solution of Coupled Problems: Comparison of Monolithic and Partitioning Approaches. *PAMM*, 10(1):395–396.

Zmitrowicz, A. (2009). Contact stresses: a short survey of models and methods of computations. *Archive of Applied Mechanics*, 80(12):1407–1428.

Curriculum Vitae

Personal Information

Robert Beyer
born on Febuary 7, 1988
in Greifswald, Germany

Education

08/1998–07/2007	Christian-Ludwig-Liscow Gymnasium, Wittenburg, Germany
10/2007–09/2011	Undergraduate studies of Computational Engineering, Leibniz Universität Hannover, Germany, Graduation to Bachelor of Science
10/2011–01/2013	Graduate studies of Computational Engineering, Leibniz Universität Hannover, Germany, Graduation to Master of Science

Professional Experience

02/2013–06/2016	Research Assistant, Institute of Mechanics and Computational Mechanics, Leibniz Universität Hannover, Germany

Forschungs- und Seminarberichte

Institut für Baumechanik und Numerische Mechanik
Gottfried Wilhelm Leibniz Universität Hannover

Bisher in dieser Schriftenreihe erschienene Berichte:

S 73/1 Seminar über Thermodynamik und Kontinuumsmechanik, Hannover 1973

F 75/1 "Die Spannungsberechnung im Rahmen der Finite–Element–Methode",
R. Ahmad, Dissertation, April 1975

F 76/1 "Zur Theorie und Anwendung der Stoffgleichungen elastisch–plastisch–viskoser Werkstoffe",
H. Mentlein, Dissertation, April 1976

S 77/1 Seminar über lineare und geometrisch nichtlineare Schalentheorie einschließlich Stabilitätstheorie, Hannover 1977

F 77/2 "Beitrag zur Berechnung von Gründungsplatten mit Hilfe der Finite–Element–Methode",
H. Meyer, Dissertation, Juli 1977

F 77/3 "Zur Berechnung der Eigenfrequenzen und Eigenschwingungsformen räumlich vorgekrümmter und vorverwundener Stäbe",
J. Möhlenkamp, Dissertation, Dezember 1977

F 77/4 "Zur Theorie und Berechnung geometrisch und physikalisch nichtlinearer Kontinua mit Anwendung der Methode der finiten Elemente",
J. Paulun, Dissertation, Dezember 1977

S 78/1 2. Seminar über Thermodynamik und Kontinuumsmechanik,
Hannover 1978

F 79/1 "Theoretische und numerische Behandlung geometrisch nichtlinearer viskoplastischer Kontinua",
K.–D. Klee, Dissertation, Februar 1979

F 79/2 "Zur Konstruierbarkeit von Variationsfunktionalen für nichtlineare Probleme der Kontinuumsmechanik",
J. Siefer, Dissertation, Oktober 1979

F 80/1 "Theoretische und numerische Behandlung gerader Stäbe mit endlichen Drehungen",
M. Kessel, Dissertation, Februar 1980

F 81/1 "Zur Berechnung von Kontakt– und Stoßproblemen elastischer Körper mit Hilfe der Finite–Element–Methode",
P. Wriggers, Dissertation, Januar 1981

F 81/2 "Stoffgleichungen für Steinsalze unter mechanischer und thermischer Beanspruchung",
J. Olschewski, E. Stein, W. Wagner, D. Wetjen, geänderte Fassung eines Zwischenberichtes zum BMFT–Forschungsvorhaben KWA 1608/5

F 82/1 "Konvergenz und Fehlerabschätzung bei der Methode der Finiten Elemente",
R. Rohrbach, E. Stein, Abschlußbericht eines VW–Forschungsvorhabens, Februar 1982

F 82/2 "Alternative Spannungsberechnung in Finite–Element–Verschiebungsmodellen",
C. Klöhn, Dissertation, November 1982

F 83/1 Seminar über nichtlineare Stabtheorie, Hannover 1983

F 83/2 "Beiträge zur nichtlinearen Theorie und inkrementellen Finite–Element– Berechnung dünner elastischer Schalen",
A. Berg, Dissertation, Juli 1983

F 83/3 "Elastoplastische Plattenbiegung bei kleinen Verzerrungen und großen Drehungen",
J. Paulun, Habilitation, September 1983

F 83/4 "Geometrisch nichtlineare FE–Berechnung von Faltwerken mit plastisch / viskoplastischem Deformationsverhalten",
M. Krog, Dissertation, Dezember 1983

F 85/1 Verleihung der Ehrendoktorwürde des Fachbereichs Bauingenieur– und Vermessungswesen der Universität Hannover an die Herren Prof. Dr. Drs. h.c. J.H. Argyris, Dr.–Ing. H.Wittmeyer

F 85/2 "Eine geometrisch nichtlineare Theorie schubelastischer Schalen mit Anwendung auf Finite–Element–Berechnungen von Durchschlag– und Kontaktproblemen",
W. Wagner, Dissertation, März 1985

F 85/3 "Geometrisch/physikalisch nichtlineare Probleme — Struktur und Algorithmen — ", GAMM–Seminar im Februar 1985 in Hannover

F 87/1 "Finite–Elemente–Berechnungen ebener Stabtragwerke mit Fließgelenken und großen Verschiebungen",
R.Kahn, Dissertation, Oktober 1987

F 88/1 "Theorie und Numerik schubelastischer Schalen mit endlichen Drehungen unter Verwendung der Biot–Spannungen",
F. Gruttmann, Dissertation, Juni 1988

F 88/2 "Optimale Formgebung von Stabtragwerken mit Nichtlinearitäten in der Zielfunktion und in den Restriktionen unter Verwendung der Finite-Element-Methode",
V. Berkhahn, Dissertation, Oktober 1988

F 88/3 "Beiträge zur Theorie und Numerik großer plastischer und kleiner elastischer Deformationen mit Schädigungseinfluß",
R. Lammering, Dissertation, November 1988

F 88/4 "Konsistente Linearisierungen in der Kontinuumsmechanik und ihrer Anwendung auf die Finite–Elemente–Methode",
P. Wriggers, Habilitation, November 1988

F 88/5 "Mathematische Formulierung und numerische Methoden für Kontaktprobleme auf der Grundlage von Extremalprinzipien",
D. Bischoff, Habilitation, Dezember 1988

F 88/6 "Zur numerischen Behandlung thermomechanischer Prozesse",
C. Miehe, Dissertation, Dezember 1988

F 89/1 "Zur Stabilität und Konvergenz gemischter finiter Elemente in der linearen Elastizitätstheorie",
R. Rolfes, Dissertation, Juni 1989

F 89/2 "Traglastberechnungen von Faltwerken mit elastoplastischen Deformationen",
K.-H. Lambertz, Dissertation, Oktober 1989

F 89/3 "Transientes Kriechen und Kriechbruch im Steinsalz",
U. Heemann, Dissertation, November 1989

F 89/4 "Materialgesetze zum Verhalten von Betonkonstruktionen bei harten Stößen",
E. Stein, P. Wriggers, T. Vu Van & T. Wedemeier, Dezember 1989

F 89/5 "Lineare Konstruktion und Anwendungen von Begleitmatrizen",
C. Carstensen, Dissertation, Dezember 1989

F 90/1 "Zur Berechnung prismatischer Stahlbetonbalken mit verschiedenen Querschnittsformen für allgemeine Beanspruchungen",
H. N. Lucero–Cimas, Dissertation, April 1990

F 90/2 "Zur Behandlung von Stoß- Kontaktproblemen mit Reibung unter Verwendung der Finite–Element–Methode",
T. Vu Van, Dissertation, Juni 1990

F 90/3 "Netzadaption und Mehrgitterverfahren für die numerische Behandlung von Faltwerken",
L. Plank, Dissertation, September 1990

F 90/4 "Beiträge zur Theorie und Numerik finiter inelastischer Deformationen",
N. Müller–Hoeppe, Dissertation, Oktober 1990

F 90/5 "Beiträge zur Theorie und Numerik von Materialien mit innerer
Reibung am Beispiel des Werkstoffes Beton",
T. Wedemeier, Dissertation, Oktober 1990

F 91/1 "Zur Behandlung von Stabilitätsproblemen der Elastostatik mit der Methode der Finiten Elemente",
W. Wagner, Habilitation, April 1991

F 91/2 "Mehrgitterverfahren und Netzadaption für lineare und nichtlineare statische Finite–Elemente–Berechnungen von Flächentragwerken",
W. Rust, Dissertation, Oktober 1991

F 91/3 "Finite Elemente Formulierungen im Trefftzschen Sinne für dreidimensionale anisotrop–elastische Faserverbundstrukturen",
K. Peters, Dissertation, Dezember 1991

F 92/1 "Einspielen und dessen numerische Behandlung von Flächentragwerken aus ideal plastischem bzw. kinematisch verfestigendem Material",
G. Zhang, Dissertation, Februar 1992

F 92/2 "Strukturoptimierung stabilitätsgefährdeter Systeme mittels analytischer Gradientenermittlung",
A. Becker, Dissertation, April 1992

F 92/3 "Duale Methoden für nichtlineare Optimierungsprobleme in der Strukturmechanik",
R. Mahnken, Dissertation, April 1992

F 93/1 "Kanonische Modelle multiplikativer Elasto–Plastizität. Thermodynamische Formulierung und numerische Implementation",
C. Miehe, Habilitation, Dezember 1993

F 93/2 "Theorie und Numerik zur Berechnung und Optimierung von Strukturen aus isotropen, hyperelastischen Materialien",
F.–J. Barthold, Dissertation, Dezember 1993

F 94/1 "Adaptive Verfeinerung von Finite-Element-Netzen für Stabilitätsprobleme von Flächentragwerken",
E. Stein, B. Seifert, W. Rust, Forschungsbericht, Oktober 1994

F 95/1 "Adaptive Verfahren für die Formoptimierung von Flächentragwerken unter Berücksichtigung der CAD–FEM–Kopplung",
A. Falk, Dissertation, Juni 1995

F 96/1 "Theorie und Numerik dünnwandiger Faserverbundstrukturen",
F. Gruttmann, Habilitation, Januar 1996

F 96/2 "Zur Theorie und Numerik finiter elastoplastischer Deformationen von Schalenstrukturen",
B. Seifert, Dissertation, März 1996

F 96/3 "Theoretische und algorithmische Konzepte zur phänomenologischen Beschreibung anisotropen Materialverhaltens",
J. Schröder, Dissertation, März 1996

F 96/4 "Statische und dynamische Berechnungen von Schalen endlicher elastischer Deformationen mit gemischten finiten Elementen",
P. Betsch, Dissertation, März 1996

F 96/5 "Kopplung von Finiten Elementen und Randelementen für ebene Elastoplastizität mit Implementierung auf Parallelrechnern",
M. Kreienmeyer, Dissertation, März 1996

F 96/6 "Theorie und Numerik dimensions- und modelladaptiver Finite-Elemente-Methoden von Flächentragwerken",
S. Ohnimus, Dissertation, Juni 1996

F 96/7 "Adaptive Finite Elemente Methoden für MIMD-Parallelrechner zur Behandlung von Strukturproblemen mit Anwendung auf Stabilitätsprobleme",
O. Klaas, Dissertation, Juli 1996

F 96/8 "Institutsbericht 1971–1996 aus Anlaß des 25-jährigen Dienstjubiläums von Prof. Dr.-Ing. Dr.-Ing. E.h. Dr. h.c. mult. Erwin Stein, Dezember 1996

F 97/1 "Modellierung und Numerik duktiler kristalliner Werkstoffe",
P. Steinmann, Habilitation, August 1997

F 97/2 “Formoptimierung in der Strukturdynamik”,
L. Meyer, Dissertation, September 1997

F 97/3 “Modellbildung und Numerik für Versagensprozesse in Gründungen von Caisonwellenbrechern”,
M. Lengnick, Dissertation, November 1997

F 98/1 “Adaptive gemischte finite Elemente in der nichtlinearen Elastostatik und deren Kopplung mit Randelementen”,
U. Brink, Dissertation, Februar 1998

F 98/2 “Theoretische und numerische Aspekte zur Parameteridentifikation und Modellierung bei metallischen Werkstoffen”,
R. Mahnken, Habilitation, Juli 1998

F 98/3 “Lokalisierung und Stabilität der Deformation wassergesättigter bindiger und granularer Böden”,
J. M. Panesso, Dissertation, August 1998

F 98/4 “Theoretische und numerische Methoden in der angewandten Mechanik mit Praxisbeispielen”,
R. Mahnken (Hrsg.), Festschrift anlässlich der Emeritierung von Prof. Dr.–Ing. Dr.–Ing. E.h. h.c. mult. Erwin Stein, November 1998

F 99/1 “Eine h-adaptive Finite–Element–Methode für elasto–plastische Schalenprobleme in unilateralem Kontakt”,
C.-S. Han, Dissertation, Juli 1999

F 00/1 “Ein diskontinuierliches Finite–Element–Modell für Lokalisierungsversagen in metallischen und granularen Materialien”,
C. Leppin, Dissertation, März 2000

F 00/2 “Untersuchungen von Strömungen in zeitlich veränderlichen Gebieten mit der Methode der Finiten Elemente”,
H. Braess, Dissertation, März 2000

F 00/3 “Theoretische und algorithmische Beiträge zur Berechnung von Faserverbundschalen”,
J. Tessmer, Dissertation, März 2000

F 00/4 “Theorie und Finite-Element-Methode für die Schädigungsbeschreibung in Beton und Stahlbeton”,
D. Tikhomirov, Dissertation, August 2000

F 01/1 “A C1 - continuous formulation for finite deformation contact”,
L. Krstulovic-Opara, Dissertation, Januar 2001

F 01/2 “Strain Localisation Analysis for Fully and Partially Saturated Geomaterials”,
H. Zhang, Dissertation, Januar 2001

F 01/3 “Meso-makromechanische Modellierung von Faserverbundwerkstoffen mit Schädigung”,
C. Döbert, Dissertation, April 2001

F 01/4 “Thermomechanische Modellierung gummiartiger Polymerstrukturen”,
S. Reese, Habilitation, April 2001

F 01/5 “Thermomechanisches Verhalten von Gummimaterialien während der Vulkanisation – Theorie und Numerik –”,
M. André, Dissertation, April 2001

F 01/6 "Adaptive FEM für elastoplastische Deformationen – Algorithmen und Visualisierung",
M. Schmidt, Dissertation, Juni 2001

F 01/7 "Verteilte Algorithmen für h-, p- und d-adaptive Berechnungen in der nichtlinearen Strukturmechanik ",
R. Niekamp, Dissertation, Juni 2001

F 01/8 "Theorie und Numerik zur Berechnung und Optimierung von Strukturen mit elastoplastischen Deformationen",
K. Wiechmann, Dissertation, Juli 2001

F 01/9 "Direct Computation of Instability Points with Inequality Contraints using the Finite Element Method",
H. Tschöpe, Dissertation, September 2001

F 01/10 "Theorie und Numerik residualer Fehlerschätzer für die Finite-Elemente-Methode unter Verwendung äquilibrierter Randspannungen",
S. Ohnimus, Habilitation, September 2001

F 02/1 "Adaptive Algorithmen für thermo-mechanisch gekoppelte Kontaktprobleme",
A. Rieger, Dissertation, August 2002

F 02/2 "Consistent coupling of shell- and beam-models for thermo-elastic problems",
K. Chavan, Dissertation, September 2002

F 03/1 "Error-controlled adaptive finite element methods in large strain hyperelasticity and fracture mechanics",
M. Rüter, Dissertation, Mai 2003

F 03/2 "Formulierung und Simulation der Kontaktvorgänge in der Baugrund-Tragwerks-Interaktion",
A. Haraldsson, Dissertation, Juni 2003

F 03/3 "Concepts for Nonlinear Orthotropic Material Modeling with Applications to Membrane Structures",
T. Raible, Dissertation, Juni 2003

F 04/1 "On Single- and Multi-Material arbitrary Lagrangian-Eulerian Approaches with Application to Micromechanical Problems at Finite Deformations",
D. Freßmann, Dissertation, Oktober 2004

F 04/2 "Computational Homogenization of Microheterogeneous Materials at Finite Strains Including Damage",
S. Löhnert, Dissertation, Oktober 2004

F 05/1 "Numerical Micro-Meso Modeling of Mechanosensation driven Osteonal Remodeling in Cortical Bone",
C. Lenz, Dissertation, Juli 2005

F 05/2 "Mortar Type Methods Applied to Nonlinear Contact Mechanics",
K.A. Fischer, Dissertation, Juli 2005

F 05/3 "Models, Algorithms and Software Concepts for Contact and Fragmentation in Computational Solid Mechanics",
C. Hahn, Dissertation, November 2005

F 06/1 "Computational Homogenization of Concrete",
S. Moftah, Dissertation, Januar 2006

F 06/2 "Reduction Methods in Finite Element Analysis of Nonlinear Structural Dynamics",
H. Spiess, Dissertation, Februar 2006

F 06/3 "Theoretische und algorithmische Konzepte zur Beschreibung des beanspruchungsadaptiven Knochenwachstums",
B. Ebbecke, Dissertation, März 2006

F 06/4 "Experimentelle Untersuchungen an elastomeren Werkstoffen",
M. Dämgen, Dissertation, Dezember 2006

F 07/1 "Numerische Konzepte zur Behandlung inelastischer Effekte beim reibungsbehafteten Rollkontakt",
M. Ziefle, Dissertation, Februar 2007

F 07/2 "Begleitbuch zur Leibniz-Ausstellung",
Hrsg: E. Stein, P. Wriggers, 2007

F 07/3 "Modellierung und Simulation der hochfrequenten Dynamik rollender Reifen",
M. Brinkmeier, Dissertation, Juni 2007

F 07/4 "Computational Homogenization of micro-structural Damage due to Frost in Hardened Cement Paste",
M. Hain, Dissertation, Juli 2007

F 07/5 "Elektromechanisch gekoppelte Kontaktmodellierung auf Mikroebene",
T. Helmich, Dissertation, August 2007

F 07/6 "Dreidimensionales Diskrete Elemente Modell für Superellipsoide",
C. Lillie, Dissertation, Oktober 2007

F 07/7 "Adaptive Methods for Continuous and Discontinuous Damage Modeling in Fracturing Solids",
S.H. Reese, Dissertation, Oktober 2007

F 08/1 "Student Projects of Micromechanics",
Hrsg: U. Nackenhorst, August 2008

F 09/1 "Theory and Computation of Mono- and Poly- crystalline Cyclic Martensitic Phase Transformations",
G. Sagar, Dissertation, August 2009

F 09/2 "Student projects of Micromechanics",
D. Balzani and U. Nackenhorst, Course Volume, October 2009

F 09/3 "Multiscale Coupling based on the Quasicontinuum Framework, with Application to Contact Problems",
W. Shan, Dissertation, November 2009

F 10/1 "A Multiscale Computational Approach for Microcrack Evolution in Cortical Bone and Related Mechanical Stimulation of Bone Cells",
D. Kardas, Dissertation, September 2010

F 11/1 "Ein integrales Modellierungskonzept zur numerischen Simulation der Osseointegration und Langzeitstabilität von Endoprothesen",
A. Lutz, Dissertation, Oktober 2011

F 12/1 "Ein physikalisch motiviertes Reifen-Fahrbahnmodell für die Gesamtfahrzeugsimulation",
R. Chiarello, Dissertation, Februar 2012

F 13/1 "Thermomechanical Analysis of Tire Rubber Compounds in Rolling Contact",
A. Suwannachit, Dissertation, September 2012

F 13/2 "Towards a Finite Element Model for Fluid Flow in the Human Hip Joint",
K. Fietz, Dissertation, September 2013

F 14/1 "Micro-Mechanically Based Damage Analysis of Ultra High Performance Fibre Reinforced Concrete Structures with Uncertainties",
A. Hürkamp, Dissertation, Dezember 2013

F 14/2 "Numerical Solution of High-Dimensional Fokker-Planck Equations with Discontinuous Galerkin Methods",
F. Loerke, Dissertation, Dezember 2013

F 14/3 "Numerische Simulation probabilistischer Schädigungsmodelle mit der Stochastischen Finite Elemente Methode",
P.-P. Jablonski, Dissertation, September 2014

F 15/1 "On a Finite Element Approach for the Solution of a mechanically Stimulated Biochemical Fracture Healing Model",
A. Sapotnick, Dissertation, Februar 2015

F 15/2 "Stimulation of Elastic-Plastic Material Behavior with Uncertain Material Parameters. A Spectral Stochastic Finite Element method Approach",
S. Fink, Dissertation, Februar 2015

F 15/3 "A Fully Micro-mechanically Motivated Material Law for Filled Elastomer",
O. Stegen, Dissertation, Februar 2016

F 16/1 "A modified adaptive harmony search algorithm approach on structural identification and damage detection",
M. M. Jahjouh, Dissertation, März 2016

F 17/1 "Computational simulation of piezo-electrically stimulated bone adaption surrounding activated teeth implants",
S. A. Shirazibeheshtiha, Dissertation, Januar 2017